Microstructure and mechanical properties of glass-ceramics from the MgO-Al O -SiO system for ballistic protection

Leonardo Sant'Ana- Gallo

ANNÉE 2016

THÈSE / UNIVERSITÉ DE RENNES 1
sous le sceau de l'Université Bretagne Loire

En Cotutelle Internationale avec
UNIVERSIDADE FEDERAL DE SÃO CARLOS

pour le grade de

DOCTEUR DE L'UNIVERSITÉ DE RENNES 1

Mention : Science des Matériaux

Ecole doctorale Sciences De La Matière

SANT'ANA-GALLO Leonardo

Préparée à l'unité de recherche IPR UMR UR1-CNRS 6251
Département Mécanique et Verres - Institut de Physique de Rennes
UFR Sciences et Propriété de la Matière

Microstructure and mechanical properties of glass-ceramics from the MgO-Al_2O_3-SiO_2 system for ballistic protection

Thèse soutenue à São Carlos, Brésil le 26 Septembre 2016

devant le jury composé de :

Tanguy ROUXEL
Professeur des universités - Université de Rennes 1 / *directeur de thèse*

Francisco-Carlos SERBENA
Professeur des universités - Universidade Estadual de Ponta Grossa / *rapporteur*

Fabrice ROSSIGNOL
Directeur de Recherche - Université de Limoges / *rapporteur*

Marcello RUBENS-BARSI-ANDREETA
Professeur des universités – Universidade Federal de São Carlos / *examinateur*

Joachim DEUBENER
Professeur des universités - Technische Universität Clausthal / *examinateur*

Edgar DUTRA-ZANOTTO
Professeur des universités - Universidade Federal de São Carlos / *co-directeur de thèse*

DEDICATION

To my beloved girlfriend, Yara Assis Hernandes, who always supported and stood by my side.

VITAE OF THE CANDIDATE

Master of Science in Materials Science and Engineering at UFSCar (2012). Materials Engineer at UFSCar (2010).

ACKNOWLEDGEMENTS

The first and most important acknowledgement is addressed to God, for Him being so generous to me, especially during the development of the thesis. He gave me strength to never give up and put wonderful people around me during these years to lighten my path.

Я бы хотел поблагодарить вас профессор Владимир Фокин за то что , вы всегда учили меня и были хорошим другом даже на растоянии. Вы всегда были для меня источником вдохновлением с моего первого шага в лабораторию. Я надеюсь всегда видеть вас в Сан-Карлусе.

Agradeço especialmente minha namorada, que esteve ao meu lado nestes quatro anos e vivenciou comigo as dificuldades inerentes do desenvolvimento de uma tese. Amparou-me e deu-me ânimo para que não deixasse a bola cair. Obrigado amor. Sem você ninguém estaria lendo este trabalho.

Aos meus pais Celso e Maria Teresa e ao meu irmão Igor. Disse o Papa Francisco: “Sem família, sem o calor do lar, a vida torna-se vazia; começam a faltar as redes que nos sustentam na adversidade, alimentam a vida quotidiana e motivam na luta pela prosperidade”. A vocês, meu muito obrigado.

Agradeço também a família que escolhi fazer parte aqui em São Carlos: o LaMaV. Dez anos depois de participar (e não passar) de uma seleção de alunos para iniciação científica, realizar meu estágio, mestrado e doutorado, entrego minha tese. Agradeço aos alunos de graduação Carlos Eduardo de Meo e Gabriel Toshiaki Tayama, por terem auxiliado no desenvolvimento do projeto. Um obrigado mais que especial à Laurie e ao Zé, sem os quais este laboratório ficaria de pernas pro ar!

Aux amis du Département Mécanique et Verres, à Rennes. Dès les techniciens aux chercheurs et professeurs, vous tous ont fait que mon séjour a été le plus agréable possible. Vous êtes aussi responsables pour maintenir un labo au plus haut niveau, qui a donné la possibilité de réaliser un excellent travail. Un remerciement spécial à Pierre Mezeix, Marion Dubernet, Zhao Yue Yao et Theany To, mes collègues de bureau, pour créer une ambiance très agréable tous les jours.

I would also like to address a special thanks to the professionals that helped me with discussions and experiments that enlightened my way. Dr. Jefferson Bettini, from the Brazilian Nanotechnology National Laboratory and Prof. Dr. Nathaly Audebrand from the Chemistry Science Institute of the University of Rennes 1.

ABSTRACT

In situ experiments were conducted on a glass dubbed 75-25, of the MgO-Al_2O_3-SiO_2 (MAS) system, using TiO_2 as the main nucleating agent, in order to examine the evolution of Young's modulus (E), shear modulus (G) and Poisson's ratio (ν), and the sequence of the crystalline phases formed during a double-stage heat treatment. The effects of crystallization on hardness and fracture toughness were also examined. High temperature X-ray diffraction experiments revealed the presence of spinel ($MgO.Al_2O_3$), rutile (TiO_2), karooite ($MgO.2TiO_2$), sillimanite ($Al_2O_3.SiO_2$) and sapphirine ($4MgO.5Al_2O_3.2SiO_2$) after crystallization. The elastic and shear moduli of the glass-ceramics (GC) were approximately 20% larger than those of the parent glass. Hardness values were close to 10 GPa and K_{IC} close to 1.2 MPa.$m^{1/2}$. Aiming to obtain transparent and colorless GC, new formulations, dubbed ZT1B4, 75-25/ZT and 75-25/25Ti, with lower titania content and higher zirconia content, were proposed and crystallized. Formulation ZT1B4 yielded a transparent GC with hardness of up to 8 GPa and an indentation fracture toughness (IFT) about 40% higher than that of the parent glass. Formulations 75-25/ZT and 75-25/25Ti yielded transparent GC with hardness values of up to 9 GPa and an IFT up to 35% higher than that of the parent glass. A series of glasses were also melted using metallic Ag as nucleating agent instead of ZrO_2 and TiO_2. The applied heat treatments generated non-homogeneous GC, which became warped due to the high crystallization temperatures. These new precursor glasses were therefore discarded. Transmittance in the ultraviolet to visible range (□□from□380 nm to 780 nm) was measured in the glass and GC samples of formulations 75-25, 75-25/ZT and 75-25/25Ti. Formulation 75-25/ZT presented the highest transmittance in both glass and GC states. It was concluded that among the new compositions, formulation 75-25/ZT is the most suitable one for use as ballistic protection when transparency to visible light is required.

RÉSUMÉ

L'étude a été menée en visant le développement de vitrocéramiques avec une microstructure appropriée pour l'application en tant que matériau transparent pour la protection balistique. Actuellement l'alumine polycristalline est le matériau céramique le plus utilisé pour cette application. Les vitrocéramiques représentent une alternative, car elles peuvent présenter des propriétés mécaniques qui les rendent aptes à une telle demande, mais avec des valeurs de densité inférieures, ce qui emmène à la fabrication de protections plus légères. Il est connu que les matériaux utilisés comme protection balistiques ont la dureté et des constantes élastiques élevées. Le système vitreux $MgO.Al_2O_3.SiO_2$ (MAS) peut former des phases cristallines de dureté élevée qui peut, en principe, conduire à de protections balistiques légères et efficaces.

À partir de l'étude d'un verre nommé 75-25, du système $MgO\text{-}Al_2O_3\text{-}SiO_2$ (MAS), ayant du TiO_2 comme principal agent de nucléation il a été étudiée l'évolution du module de Young (E), du module de cisaillement (G) et du coefficient de Poisson (ν), ainsi que l'ordre d'apparition des phases cristallines lors d'un double traitement thermique, à travers des mesures *in situ*. Le même cycle thermique a été utilisé pour observer l'évolution des constantes élastiques et pour effectuer la diffraction des rayons X à des températures élevées. Ce cycle thermique est constitué par un traitement de nucléation à 1006 K pendant 48 heures, et par un traitement de cristallisation à 1173 K, qui a été suivi pendant 10hs. La diffraction des rayons X a détecté, après 31 minutes, la présence de spinelle ($MgO.Al_2O_3$), rutile (TiO_2), karooite ($MgO.2TiO_2$) et sillimanite ($Al_2O_3.SiO_2$). Après 61 minutes, la présence de sapphirine ($4MgO.5Al_2O_3.2SiO_2$) a aussi été détectée.

En ce qui concerne l'évolution des constantes élastiques, il a été observé que l'augmentation de la température entraîne une réduction des valeurs de E, G et ν à des températures allant jusqu'à $T < T_{cristallisation}$ (1173 K). Pendant le plateau de 48 heures à la température de nucléation (1006 K), il y a eu une légère augmentation des constantes élastiques en raison de l'apparition de germes cristallins. À la température de cristallisation l'augmentation des

constantes élastiques est plus prononcée à cause de la croissance des cristaux. Après traitement thermique, les constantes élastiques de la vitrocéramique sont environ 20% plus élevées par rapport au verre de base.

L'effet de la cristallisation sur la dureté et la ténacité (K_{IC}) a également été étudié. Quatre vitrocéramiques avec différents traitements de cristallisation ont été préparées. Toutes les vitrocéramiques ont été obtenues par le même traitement thermique de nucléation, à la même température et pour la même durée (48 heures à 1006 K), mais avec différentes durées de traitement thermique de croissance, à la température de cristallisation (1173 K). Les temps de 31 min, 61 min, 92 min et 153 min de croissance ont été choisis parce qu'ils représentent les différentes étapes de la courbe d'évolution des constantes élastiques avec la cristallisation.

La dureté des vitrocéramiques et du verre de base a été mesurée avec l'application de différentes charges. La dureté des verres et des vitrocéramiques a montré une tendance à des valeurs plus grandes pour des charges appliquées plus petites, un phénomène connu sous le nom d'*Indentation Size Effect* (ISE). Pour des charges très élevées, l'augmentation de la dureté a également été observée par un craquage excessif des échantillons avec l'application de la charge. Les valeurs de dureté des échantillons vitrocéramiques sont proches de 10 GPa. Bien que proches, les valeurs de dureté ont tendance à augmenter avec l'augmentation de la durée du traitement thermique de cristallisation. La ténacité des vitrocéramiques et du verre de base a été mesurées par la technique *Single-Edge Precracked Beam* (SEPB). Toutes les vitrocéramiques en étude ont présenté une valeur de K_{IC} proche de 1,2 MPa.$m^{1/2}$. Contrairement à ce qui a été observée pour la dureté, l'échantillon qui a présenté une ténacité légèrement supérieure est celui qui a été obtenu avec le traitement de cristallisation le plus court (31 min).

La cristallisation du verre 75-25 conduit à des vitrocéramiques transparentes, mais colorées en raison de la présence de TiO_2. Le changement de valence Ti^{4+} à Ti^{3+} favorise l'absorption dans la longueur d'onde de 570 nm (dans la région du visible), ce qui donne à cette composition de vitrocéramique une coloration qui varie du violet au brun. En connaissant le processus de

cristallisation et avec l'intention d'obtenir des vitrocéramiques transparentes et incolores, de nouvelles formulations de verres ont été proposées, avec deux stratégies différentes. Dans le premier cas, les formulations L2R4 et 75-25, déjà étudiées, ont été reformulées en faisant varier la proportion d'agents de nucléation, en réduisant la quantité de TiO_2 et en augmentant la quantité de ZrO_2 (il est connu que ZrO_2 n'entraine pas de coloration aux échantillons), mais en gardant la quantité ZrO_2 + TiO_2 constante. La formulation L2R4 a donné lieu à la formulation ZT1B4. Une étude a été effectuée pour connaître la température du taux maximal de nucléation (T_{Max}), afin d'obtenir une plus grande densité de cristaux dans les vitrocéramiques. Les échantillons ont ensuite été nucléés en T_{MAX} = 1073 K, pour des périodes de temps différentes et cristallisées à 1233 K pendant 3 heures. Les vitrocéramiques ont présentées une dureté maximale de 8 GPa et une ténacité par indentation 36% plus élevée qui le verre de base. L'analyse par diffraction de rayons X de l'échantillon vitrocéramique traité pendant 480 min à 1073 K et cristallisé pendant 3 heures à 1233 K a présenté les phases cristallines suivantes : spinelle ($MgO.Al_2O_3$) ; forstierite ($2MgO.SiO_2$) ; ZrO_2 et oxyde de zircone et magnésium ($Zr_{0,875}Mg_{0,125}O_{1,875}$). Une nouvelle série de traitements a ensuite été réalisée avec un plateau de nucléation à 1073 K, pour différents temps et un nouveau temps de croissance de 6h. Après ce traitement, les vitrocéramiques ont présenté une dureté inférieure à 9 GPa. L'analyse de diffraction des rayons X de l'échantillon vitrocéramique traité pendant 120 min à 1073 K et cristallisé pendant 6 heures à 1233 K, présente du spinelle ($MgO.Al_2O_3$) et zircone (ZrO_2) comme phases cristallines. En raison des basses valeurs de dureté (H < 9 GPa), cette composition a été rejeté.

À partir de la formulation 75-25, de nouvelles compositions de verre de base ont été formulées, nommées 75-25/ZT et 75-25/25Ti. Des échantillons de la première formulation ont été nucléés à la température correspondante au taux de nucléation maximale (T_{MAX} = 1078 K), en différents temps (de 120 min à 360 min) ; le traitement thermique de nucléation a été suivi par un traitement pour la cristallisation à 1233 K pendant 3 heures. Après ces traitements, les vitrocéramiques ont présentéés une dureté maximale de presque 8,3 GPa, et

une augmentation de la ténacité par indentation d'environ 35%. L'analyse par diffraction de rayons X de la vitrocéramique traitée pendant 360 min à 1078 K et cristallisée à 1233 K pendant 3 heures, a montré la présence de spinelle ($MgO.Al_2O_3$) et zircone (ZrO_2). À la recherche de valeurs de dureté encore plus élevées, une nouvelle série de traitements a été faite, avec nucléation encore en 1078 K, mais la cristallisation à 1233 K pendant 6 heures Les vitrocéramiques ont présenté une dureté de 9 GPa. L'analyse de diffraction des rayons X d'une vitrocéramique traitée pendant 360 min à 1078 K et cristallisée à 1233 K pendant 6 heures, a indiqué la présence des mêmes phases cristallines développés par la série précédente. Les deux formulations présentent une coloration du verre et des vitrocéramiques moins intenses que les verres d'origine, c'est à dire la composition 75-25, voire figure 1.

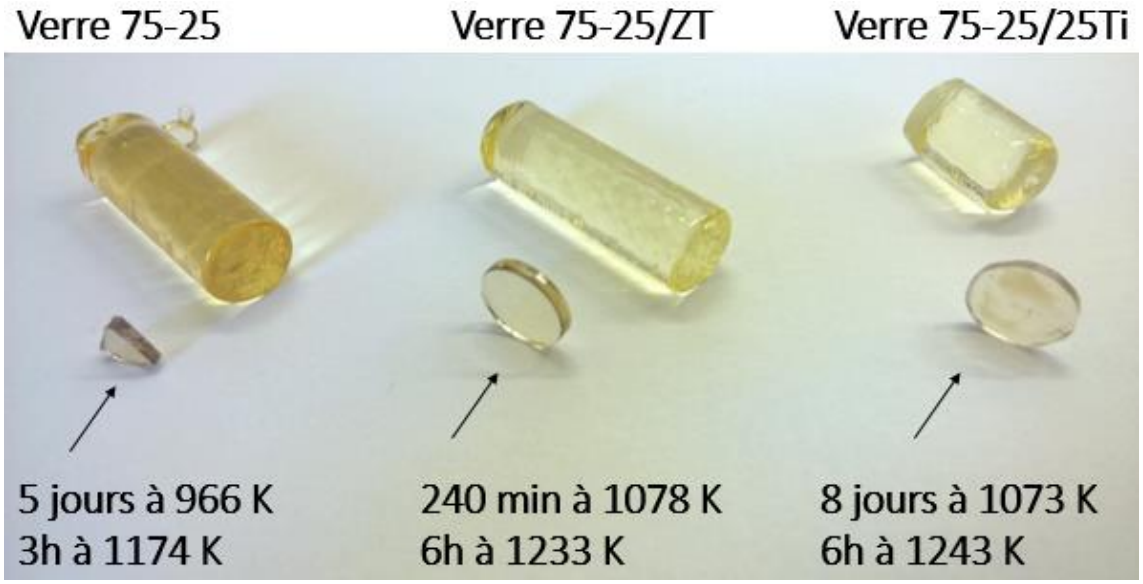

Figure 1 : Verres et vitrocéramiques des formulations 75-25, 75-25/ZT et 75-25/25Ti.

L'analyse par microscopie électronique à transmission des trois compositions (75-25, 75-25/ZT et 75-25/25Ti) après les différentes séries de traitements thermiques ont indiqué la présence de cristaux de taille nanométrique (20 nm ou moins). En fonction du traitement thermique appliqué, la présence plus ou moins importante de la phase vitreuse résiduelle a été mise

en évidence. Les analyses par *energy dispersive x-ray* (EDS) ont été réalisées sur diverses vitrocéramiques pour observer la concentration des différents éléments présents dans les échantillons.

Dans un deuxième chemin de synthèse, une série de verres contenant de l'Ag métallique comme agent de nucléation, à la place de ZrO_2 et de TiO_2, a également été fondu. Les traitements thermiques employés ont produit des vitrocéramiques non-homogènes, qui perdent la forme en raison des températures de cristallisation plus élevées. Les études avec ces nouvelles formulations de verres précurseurs n'ont pas été suivies.

La transmittance dans la région de l'ultraviolet au visible (λ de 380 nm à 780 nm) des verre et vitrocéramiques des formulations 75-25, 75-25/ZT et 75-25/25Ti ont été mesurées La formulation 75-25/ZT a donnée lieu aux valeurs de transmittance les plus élevés aussi bien pour le verre que pour la vitrocéramique. On en conclut que, parmi les nouvelles compositions, la formulation 75-25/ZT est la plus adéquate pour être utilisée comme protection balistique lorsque la transparence à la lumière visible est nécessaire. Cependant, des tests balistiques doivent être menées pour confirmer cette conclusion.

RESUMO

Em um vidro denominado 75-25, do sistema $MgO-Al_2O_3-SiO_2$ (MAS), que possui TiO_2 como agente nucleante majoritário, foi observada a evolução do Módulo de Young (E), módulo de cisalhamento (G) e coeficiente de Poisson, bem como a ordem de aparecimento de fases cristalinas durante um tratamento térmico duplo através de experimentos *in situ*. O efeito da cristalização na dureza e tenacidade à fratura também foi observado. Experimentos de difração de raios X a temperaturas elevadas detectaram a presença de espinélio ($MgO.Al_2O_3$), rutilo (TiO_2), karooita ($MgO.2TiO_2$), sillimanita ($Al_2O_3.SiO_2$) e sapphirina ($4MgO.5Al_2O_3.2SiO_2$) após a cristalização. Os módulos elásticos e de cisalhamento das vitrocerâmicas eram aproximadamente 20% maiores quando comparados com o vidro base. Valores de dureza foram próximos de 10 GPa e K_{IC} próximo de 1.2 $MPa.m^{1/2}$. Procurando obter vitrocerâmicas transparentes e incolores, novas formulações denominadas ZT1B4, 75-25/ZT e 75-25/25Ti, com menores teores de titânia e maiores teores de zircônia, foram propostas e cristalizadas. ZT1B4 originou vitrocerâmicas transparentes com dureza de até 8 GPa e incremento de tenacidade à fratura via indentação de cerca de 40% comparado com o vidro base. Formulações 75-25/ZT e 75-25/25Ti originaram vitrocerâmicas transparentes com valores de dureza de até 9 GPa e incremento de tenacidade à fratura via indentação de cerca de 35% comparado com o vidro base. Uma série de vidros contendo Ag metálico como agente nucleante no lugar de ZrO_2 e TiO_2 também foi fundida. Os tratamentos térmicos empregados geraram vitrocerâmicas não homogêneas, que perdem a forma devido às temperaturas de cristalização elevadas. Esses novos vidros precursores foram descartados. Vidros e vitrocerâmicas das formulações 75-25, 75-25/ZT e 75-25/25Ti tiveram a transmitância na região do ultravioleta ao visível, medida (λ de 380 nm a 780 nm). Formulação 75-25/ZT apresentou os maiores valores de transmitância tanto para o vidro quanto para a vitrocerâmica. Conclui-se que, dentre as novas composições, a formulação 75-25/ZT é a mais adequada para se utilizar como proteção balística quando a transparência ao visível se faz necessário.

PUBLICATIONS

GALLO, L. S.; RODRIGUES, A. C. M.; ZANOTTO, E. D.; ROUXEL, T. Correlation between crystallization, microstructure and mechanical properties of $MgO\text{-}Al_2O_3\text{-}SiO_2$ glass-ceramics. In 11^{th} International Symposium on Crystallization on Glasses and Liquids. Book of Abstracts. Nagaoka, Japan. 2015

GALLO, L. S.; MEO, C. E.; RODRIGUES, A. C. M.; ZANOTTO, E. D. Mechanical properties of transparent $MgO\text{-}Al_2O_3\text{-}SiO_2$ glass-ceramics. In 6^{th} International Workshop in Flow and Fracture of Advanced Glasses. Book of Abstracts. Weimar, Germany. 2014.

GALLO, L. S.; MEO, C. E.; RODRIGUES, A. C. M.; ZANOTTO, E. D. Hard $MgO\text{-}Al_2O_3\text{-}SiO_2$ glass-ceramics. In 23^{rd} International Congress on Glass. Hard $MgO\text{-}Al_2O_3\text{-}SiO_2$ glass-ceramic. Book of Abstracts. Prague, Czech Republic. 2013.

SUMMARY

Pg.

TABLE INDEX

FIGURE INDEX

1 INTRODUCTION

High level ballistic protection systems are made by an add-on armor and the main armor [1]. The main armor consists either of a high-performance polymer material, like Kevlar®; an aramid fiber manufactured by DuPont; or a metallic plate. The add-on armor consists of a high-hardness ceramic material, which has the purpose of breaking itself and crushing the projectile, thus diminishing the kinetic energy, and by consequence the perforation capacity of the incoming bullet. When the ceramic plate crashes, the debris crushes the projectile, since the former possesses higher hardness than the latter. The main armor must absorb what is left of the kinetic energy of the incoming projectile, as well as the ceramic's debris. The bonding of the plates is performed with the help of an adhesive polymer. The add-on armor can also be made from a glass-ceramic material.

Ceramic materials traditionally used as add-on armor are alumina (Al_2O_3) and silicon and boron carbides, and silicon and aluminum nitrates [2, 3]. When transparency is necessary, e.g. windows and helmet visors, the ceramics chosen are: sapphire (monocrystalline alumina), magnesium spinel ($MgO.Al_2O_3$), and AlON ($Al_{23}O_{27}N_5$) [4-6]. Certain glass-ceramic materials can be processed to become transparent; being, therefore, an alternative to traditional ceramics, since they generally have smaller density.

Previous studies have been conducted with MgO-Al_2O_3-SiO_2 (MAS) glass-ceramics. The compositions of two of them, dubbed L2R4 and 75-25, are presented in Table 1.1. Titania and zirconia, highlighted in the table, were used as nucleating agents.

Table 1.1 Glass compositions studied during the masters.

Component	L2R4 (mol%)	75-25 (mol%)
Al_2O_3	16.75	17.67
SiO_2	56.89	55.52
MgO	15.55	16.66
B_2O_3	1.80	1.50
TiO_2	6.90	6.90
ZrO_2	0.61	0.50
Sb_2O_3	1.50	1.25

Each composition went through 3 series of thermal treatments. The first was a single-stage heat treatment, the other two, double-stage heat treatments. The former consists in subjecting the sample to a heat-treatment on one temperature only, generating opaque, white glass-ceramics. The latter consists in heat-treating the sample on two temperatures. The first, close to the glass transition temperature, will promote crystal nucleation. The second, at a higher temperature, will promote crystal growth. With double-stage heat treatment, it is possible to obtain a transparent material. The condition is to have a crystal density in the order of 10^{21} crystals/m^3 [7]. With this density, when growth treatment is applied, crystals will not have enough space to grow and will remain smaller than the wavelength of visible light (380 – 780 nm)

Mechanical properties of the developed glass-ceramics, opaque or transparent, were in the order of 10 GPa and indentation fracture toughness (IFT) increments up to 50% compared to parent glass. Transparent glass-ceramic samples obtained from the aforementioned compositions had lilac-to-brown color, which can be seen in Fig. 1.1.

a) b)

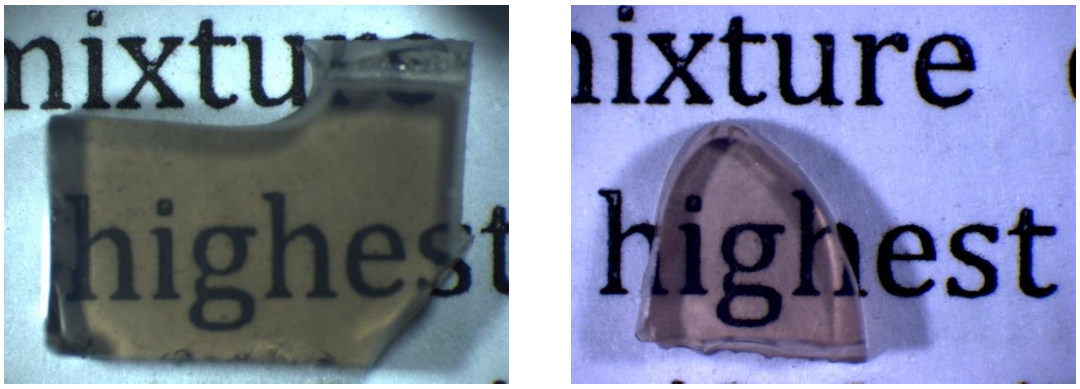

Figure 1.1 a) Glass-ceramic sample from composition L2R4. Nucleation heat-treatment at 983 K (Tg = 1003 K) for 7 days and growth heat-treatment at 1266 K for 3h. b) Glass-ceramic sample from composition 75-25. Nucleation heat-treatment at 966 K (Tg = 1008 K) for 120 h and growth heat-treatment at 1173 K for 3h.

This color is due to TiO_2. It is known that the valence change from Ti^{+4} to Ti^{+3} promotes the color change on the samples, since Ti^{3+} presents an absorption band at 570 nm, while Ti^{4+} does not present an absorption band at visible light on silicate glasses [8].

The glass-ceramics developed in this work can be used as ballistic protection, but also in any applications which require high impact resistance, such as the screens of smartphones and tablets.

2 OBJECTIVES

This work's objective was to obtain transparent and less colored glass-ceramics than the ones obtained during the master's degree studies, while attempting to maintain the achieved mechanical properties.

To achieve this goal, two paths were taken:

I. Reformulate the parent glasses in order to diminish the amount of TiO_2, since the color presented on the glass-ceramics were due to it.

II. Change the nucleating agents used to obtain bulk nucleation. Instead of using TiO_2 and ZrO_2, metallic Ag was used.

3 LITERATURE REVIEW

3.1 Ballistics

3.1.1 Definitions And Levels Of Protection

Ballistics can be defined as *"the scientific study of things that are shot or fired through the air, such as bullets and missiles"* [9]. It is divided into three categories: internal (bullet moving inside the barrel), external (bullet during flight) and terminal (bullet hitting the target). The design of a protection system is part of the terminal ballistic studies [4]. Some considerations should be taken into account when selecting materials to be used on a ballistic protection system, such as the desired protection level, total volume and weight of the system [3] and the final cost of the product. Armor systems are divided as presented in Fig. 3.1.

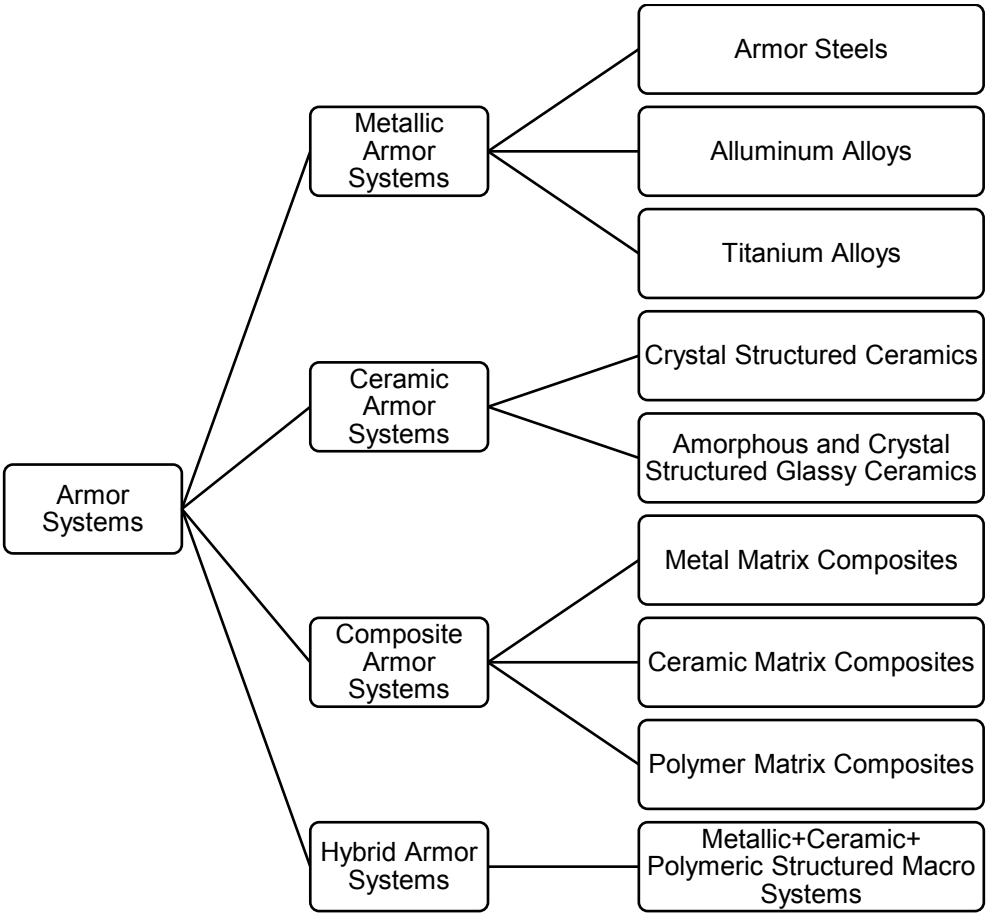

Figure 3.1 Classification of armor systems [4].

Transparent armor systems have military and civil applications, such as face and riot shields, windows on vehicles and buildings, among others. The transparent system may sustain multiple hits, explosion and scratches; have low diffraction index for a clear view, and low density for more comfortable portability [4]. They can be divided as presented in Fig. 3.2.

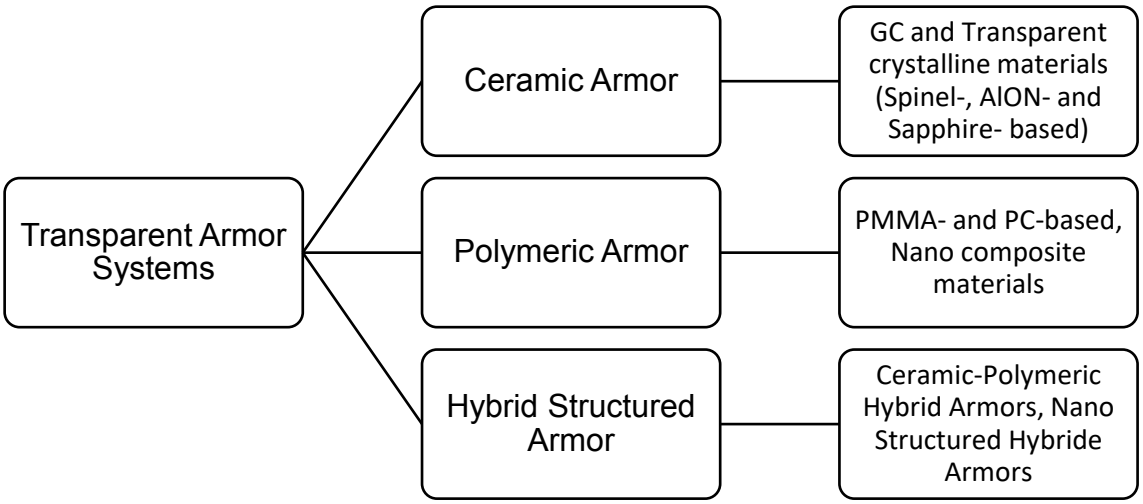

Figure 3.2 Schematic classification of transparent armor systems [4].

The ballistic resistance takes into account the gun, the projectile and its kinetic energy, the distance between consecutive shots, and the distance between the shooter and the target [10]. Brazilian Army divides ballistic protection in 6 levels, presented at ABNT NBR standard 15000:2005 [11]. Those levels are the same as proposed by the National Institute of Justice [12], from the USA, presented in table 3.1, adapted from [13].

Table 3.1 Levels of protection proposed by the Brazilian Standard ABNT NBR 15000:2005. Adapted from [12] and [13].

LEVEL	AMMUNITION	WEAPON	AMMUNITION NAME	CALIBER SIZE	REFERENCE VELOCITY	KINETIC ENERGY
I			.22 LRHV Lead	15 - 16,5 cm 6 - 6,5 in	320 +/- 12 m/s 1050 +/- 40 ft/s	133,12 J
			.38 Special RN Lead	15 - 16,5 cm 6 - 6,5 in	259 +/- 15 m/s 850 +/- 50 ft/s	342,12 J
II-A			9 mm FMJ	10 - 12 cm 4 - 4,75 in	332 +/- 12 m/s 4 - 4,75 in	440,9 J
			.357 Mag JSP	10 - 12 cm 4 - 4,75 in	381 +/- 15 m/s 1250 +/- 50 ft/s	740 J
II			9 mm FMJ	10 - 12 cm 4 - 4,75 in	358 +/- 12 m/s 1175 +/- 40 ft/s	512,66 J
			.357 Mag JSP	15 - 16,5 cm 6 - 6,5 in	425 +/- 15 m/s 1395 +/- 50 ft/s	921 J
III-A			9 mm FMJ	24 - 26 cm 9,5 - 10,25 in	426 +/- 15 m/s 1400 +/- 50 ft/s	725,9 J
			.44 Mag Lead SWC Gas Checked	14 - 16 cm 5,5 - 6,25 in	426 +/- 15 m/s 1400 +/- 50 ft/s	1406 J
III			7,62 x 51 FJ NB .308 Winchester FMJ	56 cm 22 in	838 +/- 15 m/s 2750 +/- 50 ft/s	3405 J
IV			30-06 AP	56 cm 22 in	868 +/- 15 m/s 2850 +/- 50 ft/s	4068,5 J

* AP = Armor Piercing; FJ = Full Jacketed; FMJ = Full Metal Jacket; JSP = Jacketed Soft Point; LRHV = Long Rifle High Velocity; NB = Nato Ball; RN = Round Nose; SWC = Semi Wadcutter

Levels I, II-A, II and III-A are, in order, the least effective, and can be purchased by civilians. Level III-A can take shots from 9 mm pistols and .44 Magnum, the biggest hand gun. Level III has restricted usage, only when approved by the Brazilian Army. It can take shots from an assault rifle having 7.62 x 51 mm ammunition. Level IV is the highest ranked one and is exclusively used by the armed forces. It takes shots from .30 caliber ammunition.

3.1.2 Add-On Armor And Ballistic Impact

The protection can consist of a single material or an assembly of materials, known as composite armor. In the case of the latter, materials from

different classes are used to form the protection system. A hard material is used as strike face; and a high-resistance, plastically deformable material is used as backing face. In case of human individual protection, the protection system is often formed by a ceramic plate (add-on armor) attached to a high-resistance metallic or polymeric plate (main armor) [14]. The use of different materials, with complementary properties, aims to obtain a protection system with enhanced performance [3]. Figure 3.3 presents a common configuration of a protection system, having a ceramic plate adhesively bonded with a metallic plate (rear plate).

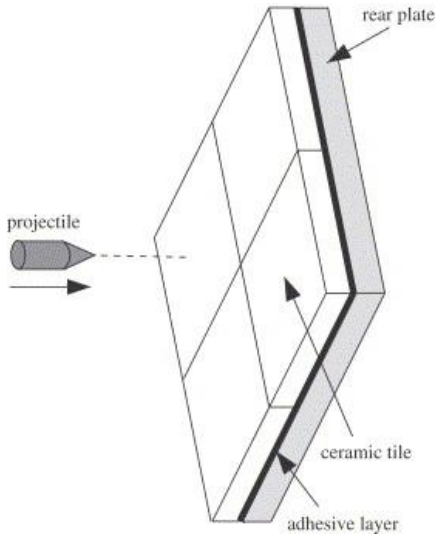

Figure 3.3 Ballistic system having a ceramic plate (add-on armor) and a metallic plate (main armor).

On ductile materials, tensions higher than rupture tension are released through localized plastic deformation. Ceramics, on the other hand, do not show significant plastic deformation. When ballistic impact occurs, the ceramic plate cracks and breaks, dissipating part of the kinetic energy of the projectile [3]. The residual energy is absorbed by the highly-resistant material that also absorbs the impact and fragments generated by the cracking of the ceramic plate [2].

Type and thickness of the high stress-resistant material used as main armor, combined with the add-on armor to form the protection system, play an

important role on crack propagation in the ceramic plate. Also, ceramic nature (oxide, non-oxide) and thickness, confining material, backing layer and geometry of the projectile influence the performance of the protection system [14]. Ceramic plates being 7-9 mm thick, bonded with aramid-fiber plates such as Kevlar®, from DuPont; or Twaron®, from Teijin, can stop a variety of projectiles. Those plates are generally covered with ballistic-grade polyamide bonded with the high stress-resistant materials [15]. During the ballistic impact, there is energy transfer to the ballistic protection system, leading to one of three cases [16]:

I. Projectile penetration, armor perforation and projectile ejection with remaining velocity, indicating its kinetic energy was higher than the energy the system could absorb.
II. Projectile partially penetrates the armor, indicating it had less kinetic energy than the system could absorb.
III. Projectile perforates the armor and has ejection velocity equal to zero. In this case, the initial projectile velocity is named ballistic limit.

The mechanics of projectile penetration itself can also be divided into three steps [14, 17]:

I. Destruction of projectile's tip and the formation of cone crack in the ceramic plate. At this point, the projectile's tip is eroded and the kinetic energy and perforation capability are drastically reduced.
II. Projectile penetration of the ceramic plate and cone crack propagation, spreading ceramic debris. The main armor deforms elastically.
III. Plastic deformation of the main armor and absorption of the residual kinetic energy of the projectile. The ceramic plate plays a major role in the first two steps.

The add-on armor in a protection system consists of a hard material which acts to diminish the penetration power of the projectile [3]. Ceramics are

suitable to be used as add-on armor since they increase the dwell time of the projectile inside the armor system, diminishing its penetration power. The usually high values of compression charges sustained by ceramics make them a suitable material, but their low resistance to multiple hits is a disadvantage [18].

It is possible to have either a monolithic ceramic or a ceramic-matrix composite material in a protection system [15]. Among oxide ceramics, the most common is polycrystalline alumina and among non-oxides, silicon and boron carbides [19] and also aluminum and titanium nitrates are applied [2, 15]. Ceramic-matrix composites, such as Al_2O_3/SiC or Al_2O_3/C reinforced with whiskers or fibers present an improved ballistic resistance when compared to monolithic ceramics due to its higher mechanical properties [15].

Glass-ceramics, whether they are transparent or not, present themselves as an interesting alternative to traditionally used ceramics for ballistic protection. They are generally less dense than polycrystalline alumina ($\rho_{Al_2O_3} = 3.95$ g/cm^3 [15]) and less expensive than non-oxide ceramics. Even transparent glass-ceramics are less expensive to produce than sapphire.

Compositions presenting lithium dissilicate ($Li_2O.2SiO_2$ – LS2) as the main crystalline phase have been studied to be used as ballistic protection [7, 20-25]. In 1984, Rudoi [20] observed that, through the use of TiO_2, ZrO_2, and SnO_2 as nucleating agents in the 3:2:1 proportion, there is an increase in chemical resistance against acids, alkalis or water.

GEC Alsthom has two patents of Transarm®, a transparent glass-ceramic of nanometric crystals to be used in visors, buildings, vehicles and so on. The first one dates back to 1995 [7] and describes the composition and heat-treatments to obtain the glass-ceramic. The second one [25], from 2003, reports a new sequence of heat-treatments at lower temperatures to obtain the same crystal density. The use of CeO_2 as refining agent is reported. A bubble-free microstructure would enhance the mechanical properties and, thus, the ballistic resistance.

Other glass-ceramics that have already been on the market are Robax® and Zerodur® from Schott [26], both from Li_2O-Al_2O_3-SiO_2 system. Glass-

ceramics from the MgO-Al_2O_3-SiO_2 system are also suitable to be used as ballistic protection. Gallo et al. [27] and Zachau and Corvers [28] have proposed different formulations of parent glasses from this system.

Although they are interesting replacing materials, a search at Web of Science for papers published until November 2015 on the subject of transparent glass-ceramics to be used as ballistic protection shows that only six documents were published until then. Only one investigates the ballistic performance of a new glass-ceramic developed for that specific application [29], from the soda-lime-silica system. The same search, but for transparent ceramics, reveals 85 papers about the subject. When searching for patents at the Derwent Innovations Index database in the same period, twenty documents related to transparent glass-ceramics for ballistic protection were found. Not all patents indicate the compositions under study.

3.1.3 Material Properties And Evaluation

It is known that a reliable correlation between the materials properties, such as Young's Modulus, fracture toughness, hardness and so on; and the ballistic performance of a body is yet to be obtained [30]. Better understanding of the mechanics behind the penetration of the projectile on the ceramic plate is necessary so that a consistent correlation of properties can be proposed.

Taking the properties of the ceramics into account, there is only one model known to the authors that is intended to foresee the performance under a ballistic impact, the D-criterion [31].

$$D = \frac{0.36 H_V C_L E}{K_{IC}^2} \tag{3.1}$$

where H_V is the Vickers hardness, E is the elastic modulus, C_L is the longitudinal sound waves propagation velocity and K_{IC} is the fracture toughness of the material.

This criterion stands as a first approach since is known to those in the field that ceramics with high hardness [18, 20, 32, 33] and that the sound propagates in it at high speed [34, 35] are good candidates to be used as add-on armor. Nonetheless, it must be said that eq. 3.1 is rather simplistic, and that the dynamics of a ballistic impact is complex and has not been fully understood so far. A complete relationship between properties, whether they are indicated in eq. 1 or not, is yet to be obtained. Although the D-criterion is intended to predict performance, not always does it manage to properly rank different materials.

To observe how complicated correlating materials properties with ballistic performance is, take the work of Budd and Darrant [7] as example. They have proposed 5 different glass-ceramic compositions. Their physical properties are presented in table 3.2, as well as its ballistic limits, relative to soda-lime-silica glass. The D-criterion, proposed by Neshpor is presented just to compare its prediction with the obtained results. To calculate the D-criterion, C_L was not taken into account.

Table 3.2 Glass-ceramic's physical properties and calculated D-criterion.

	1	**2**	**3**	**4**	**5**
Hardness (GPa)	6.3	8.5	6.7	11.1	11.4
3 pt bending (MPa)	120	167	172	149	119
E (GPa)	126	101	88	94	96
K_{IC} (MPa.m$^{1/2}$)	2.4	2.3	2.1	1.7	1.9
ρ (g/cm^3)	2.61	2.53	2.56	2.76	2.73
Relative ballistic limit*	1.13	1.18	1.17	1.16	1.16
D-criterion	954.0	1029.3	780.2	2103.6	1794.0

* the ballistic limit was taken relatively to the ballistic limit values of soda-lime-silica glass.

Table 3.3 presents the ranking of the glass-ceramics according to their properties, the ballistic limit and the D-criterion, highest-to-lowest values.

Table 3.3 Ranking of the glass-ceramics according to its physical properties.

Ballistic performance	**HV**	**3-pt bending**	**E**	**K_{IC}**	**Ballistic limit**	**D-criterion**
1	5	3	1	1	2	4
2	4	2	2	2	3	5
3	2	4	5	3	4 and 5	2
4	3	1	4	5		1
5	1	5	3	4	1	3

As it can be seen, neither a specific mechanical property nor the D-criterion comes close to properly classifying the materials according to their ballistic performance. That is the reason why the assembling of the properties should be taken into account when selecting the material. One must have noticed that glass-ceramic number 2 was not the best ranked in any of the four mechanical properties analyzed, but it was the second best in 3 of them and presented the highest relative ballistic limit.

Recently, the efforts have been concentrated on understanding the effects of the deformation rate in certain mechanical properties, as an attempt to predict the ballistic performance of a material more accurately [36]. According to Krell and Strassburguer [37], a small amount of the projectile's kinetic energy (~0,2%) is spent to fracture the ceramic body during the impact. Most of it (45-70%) is then transferred to the ceramic's debris. The ceramic-projectile interaction is mainly directed by the abrasive wear of the latter. Further works have shown that, for thin ceramic plates, the most severe damages to the projectile were caused during its penetration.

Good mechanical properties are a prerequisite to select a material to be used as ballistic protection. Ceramics presenting high hardness, toughness and Young's Modulus would, in principle, have better performance than those with lower values of the same properties. Haney and Subhash proposed how certain properties would relate to the ballistic performance of a material. Table 3.4 shows these relations.

Table 3.4 Ceramics properties and its relevance to ballistic performance [36].

PROPERTY	**RELEVANCE**
HARDNESS	Diminishes the penetration ability and provokes projectile erosion Increases dwell time Gives a first idea of the material's performance
K_{IC}	Increases resistance to penetration.
FRAGILITY*	Related to the damage zone or fragmentation size Related to the ability to dissipate damage
FRACTURE STRENGHT	Compression fracture strength may be related to the crack generation resistance and growth Diminishes shear resistance, which is related to the ballistic resistance.
ELASTIC CONSTANTS	Higher stiffness and smaller density relate to the increase of dwell time on the ceramic plate Reduces the propensity to cracking the opposite impact face Higher elastic stiffness and smaller density promotes impact energy dissipation through wave propagation.

*$fragility = \frac{H_C E}{K_{IC}^2}$; H_C is the critical hardness value, where the hardness changes from load-dependent to load-independent. E is the Young's Modulus and K_{IC} is the fracture toughness.

The idea that hardness enhances the ballistic performance comes from the fact that the higher the hardness, the higher the penetration resistance of the ceramic body. Higher hardness will lead to higher ballistic efficiency, since a smaller amount of ceramic will be needed to stop an incoming projectile. According to Haney and Subhash [36], Raymond L. Woodward was the first to propose hardness as a main property to predict the ballistic performance of a ceramic. Still according to them, LaSalvia proposed a model where hardness is presented as the potential of a ceramic to be used as ballistic protection, while toughness indicated if this potential can be achieved or not.

A direct relation between the ballistic performance and the elasticity moduli and the Poisson's ratio can be imagined, once they are deeply related to the wave velocities of a body. Higher acoustic impedance of the ceramic will result in less energy dissipated in it and more energy absorbed by the projectile. The higher the wave velocity in the ceramic body, the faster it will transfer the impact energy from the impact site to the bulk of the material.

However, knowing how each property contributes to the ballistic performance of the materials sometimes is not enough to make an accurate choice. The consideration of the mechanical properties alone can be misleading. To illustrate how complex the relation between the mechanical properties and the ballistic performance of a material is, let us take three of the most common ballistic materials as example: sapphire, spinel and polycrystalline alumina. The performances of spinel and polycrystalline alumina are reported as superior to that of sapphire, even though their static and dynamic mechanical properties are inferior. This is exactly the opposite of the thought that better ballistic performance comes with materials with superior mechanical properties.

Since the ballistic impact is an extremely fast and localized event, Haney and Subhash [36] conducted a series of dynamic measurements of mechanical

properties, such as dynamic indentation with a 10^3 s^{-1} deformation rate and 100 μs of load charge, to try to explain the better performance of sapphire.

Sapphire presented a higher hardness than spinel both under static and dynamic loads. When it comes to fragility, sapphire presents higher values than spinel. The higher fragility may indicate a higher tendency to crack and catastrophically fracture under impact loads. Spinel presents a transgranular cracking pattern that dissipates more energy than the cracking pattern presented by sapphire. It is also more resistant to projectile penetration due to the creation of fine particles that promotes the erosion and deceleration of the projectile. This characteristic is an indication of the good performance of spinel under multiple rounds.

Krell and Strassburguer [37] conducted a deeper study where not only the effect on ballistic performance of different mechanical properties of the ceramics was analyzed, but also the use of different backing materials was observed. The way the ceramic material will fracture is influenced by its intrinsic properties, but also by the properties of the backing material used on the protection system.

The materials tested were alumina, sapphire and Mg-spinel ($MgO.3Al_2O_3$). It was observed that the stability of these ceramics associated with different backing materials is guided by a hierarchy of factors. The main factor is the way the ceramic fractures, being dictated by its microstructure and dynamic stiffness, and also the material used as backing face. A minor factor is the ceramic's Young's Modulus, responsible for projectile damage during penetration. Ceramic's hardness will have stronger or weaker influence on projectile abrasion depending on the size of the fragments generated after the impact.

Depth-of-penetration (DoP) tests were conducted. This, which is a common ballistic test, consists of observing how deep a projectile penetrates on a plate. It was observed that alumina behaves differently depending on the backing material. It presents better results when steel, not aluminum, is the backing material. At first they thought the Young's Modulus was responsible for the difference in performance, since E_{steel} = 210 GPa and E_{Al} = 85 GPa. But the

performance of a glass-containing system (E_{glass} = 70 GPa) as backing was still better than one having aluminum. The answer lay on the fracture of the alumina plate when in contact with each material.

Subsequent studies were conducted to observe the influence of the ceramic's E, H and fragment size after impact. DoP tests on alumina hit by tungsten projectile (v = 1250 m/s), with steel as backing material, showed a positive influence on hardness increase by reduced grain size. The same was observed on spinel with glass as backing material. When grain size was a bi-modal distribution 3-75 μm (reported HV = 12.0 ± 0.1 GPa) the residual projectile velocity was 140 m/s. When grain size was around 0.35 μm (reported HV = 14.2 ± 0.2 GPa) the residual velocity dropped to 33 m/s.

When similar hardness is present, the ballistic performance is controlled by the Young's Modulus of the impact face. It was observed by the authors that spinel (that originates fine debris after impact) and alumina (that originates rough debris after impact) have the same hardness, but $E_{Al_2O_3}$= 380 GPa and E_{spinel} = 280 GPa. Spinel presented deeper penetration (DoP) than alumina: 8 – 8.3 mm and 4 – 6.5 mm, respectively. The tests were conducted having aluminum as backing material and steel-core armor piercing (v = 850 m/s).

The effect of mono- versus polycrystallinity was then studied. The subject had already been studied by the authors [38]. In the new studies, a 7.62 x 51 mm projectile (v = 850 m/s) impacted on a composed protection system and DoP tests were conducted on ceramic plates. The system consisted of 1-7 mm ceramic plate / 15-30 mm glass plate / 4mm polycarbonate plate. It was observed that polycrystalline alumina or fine-grained spinel stops a projectile which sapphire, the monocrystalline version of Al_2O_3, would only stop if the thickness of the plate was doubled (from 2 to 4 mm), even though sapphire presents higher mechanical properties. This behavior is regardless grain size and monocrystal orientation.

Sapphire presents intense cracking that leads to small-sized debris. However, it causes less damage than alumina with its larger-sized debris. One explanation for this fact lies in the materials microstructure. Sapphire has planes with high anisotropy on K_{IC} values. Polycrystalline alumina, on the other hand,

has more homogeneous values of K_{IC}. The difference in the mean ceramic fragment size from alumina (0.43 mm) and sapphire (0.33 mm) increases the wear of the projectile by two times. This fact had been observed by the authors in another study [38]. They affirmed that sapphire presents a high anisotropy on energy fracture at {1012} family plane and comparing with polycrystalline alumina, sapphire is submitted to a more intense cracking on close planes.

So, to answer if a monocrystalline version of a ceramic will have better performance than a polycrystalline one, each case must be analyzed. The same study that observed a difference in the ballistic performance of sapphire and alumina did not observe a difference between mono- and polycrystalline spinel [38]. The authors also inferred the importance of Young's Modulus of the ceramic material, which is associated with the deformation of the projectile and the dwell time. High Young's Modulus promotes higher dwell time and larger debris, which is similar to what occurs when stiffer backing materials are used.

Confinement also plays a role on the way ceramic tiles fracture. Woodward [14] studied several ceramics with different toughness and strength. The group included oxide ceramics such as alumina and toughened zirconia, non-oxide ceramic (two grades of TiB_2) and soda-lime glass. They were all studied in two configurations: confined and unconfined. The confined configuration had a metallic plate surrounding the sample. Plates were tested under the impact of a 7.72 mm tungsten alloy projectile, having pointed (23.2 g and 1209 m/s impact velocity) or blunt nose (19.9 g and 1243 m/s impact velocity). Among other conclusions, he observed that increasing toughness results in less fragmentation under the same impact conditions, and that a front confinement generates greater fragmentation, but with less fine-grain fragments.

3.2 $MgO – Al_2O_3 – SiO_2$ Glass System

Glass-ceramics from the $MgO\text{-}Al_2O_3\text{-}SiO_2$ glass system are suitable to be applied in high tech devices, such as microelectronics. They can be co-fired at temperatures lower than 1000 °C [39, 40]. They can also be applied as

cooktops, due to its transparency to infrared [41]. Glass-ceramics presenting cordierite as main crystal phase present good thermal stability and thermal shock resistance [42]. Bulk nucleation is not possible without the use of nucleating agents, such as TiO_2 and ZrO_2, largely applied together [43]. Zirconia has the disadvantage of having a low solubility in the glass melt (solubility at the 3 – 4 weight% range) and it increases the melting temperature. Titania, on the other hand, has a higher solubility, close to 20 weight%, and lowers the viscosity of the melt [43]. Figure 3.4 [44] presents the MgO-Al_2O_3-SiO_2 equilibrium phase diagram, in weight% of constituents. The main crystalline phases are indicated.

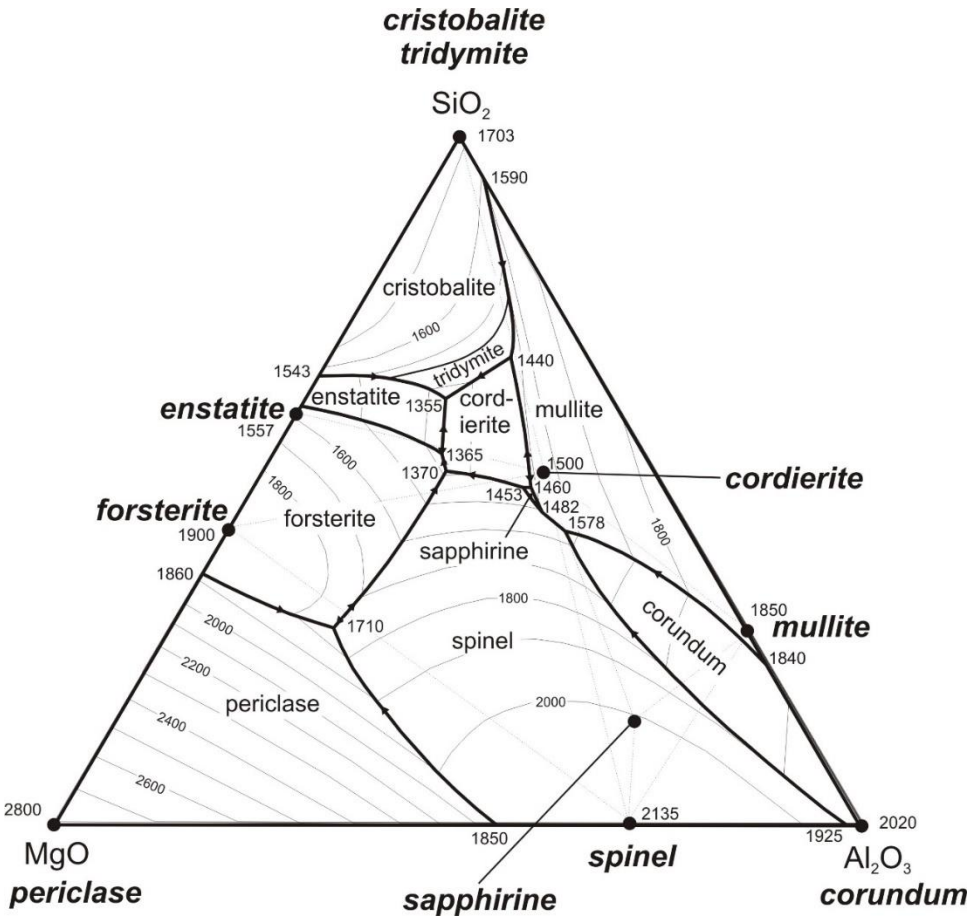

Figure 3.4 Equilibrium phase diagram for MgO-Al_2O_3-SiO_2 [44].

This system has been largely studied, and the addition of different oxides to observe the response on properties are common. Additions of Fe_2O_3 [45] and

AlN [39] have been reported. The addition of V_2O_5 as an alternate nucleating agent has also been analyzed [41]. With both titania and zirconia, there is liquid-liquid phase separation (LLPS) where one of the glasses is a nucleating-agent-rich liquid that further leads to bulk nucleation [41, 46, 47]. The same phenomenon is observed when TiO_2 and ZrO_2 are added on Li_2O – Al_2O_3 – SiO_2 (LAS) system [48]. Studies observed the nucleation of magnesium-aluminosilicate in a titania-rich liquid phase that is later used by cordierite as substrate to its nucleation [46, 47].

Zanotto and Fokin [49] studied bulk and surface nucleation of cordierite, using TiO_2 as the nucleating agent. Five glasses were prepared, with different amounts of titania and the one presenting bulk nucleation had 8.1 wt% of it. This result was the base for the two original formulations proposed during the master studies [27] and continued here. The glasses developed then were yellow color and the glass-ceramic had lilac-to-brow color, as it can be seen in Fig. 3.5.

a) b)

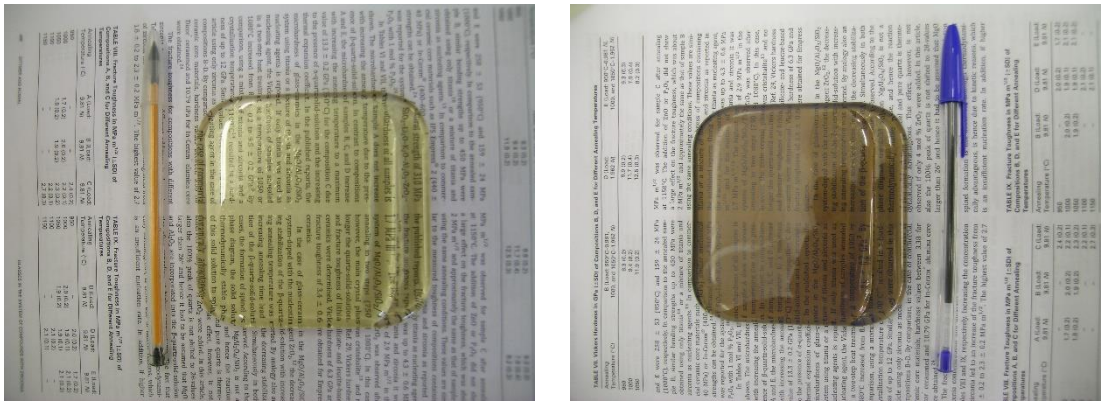

Figure 3.5 a) Glass and b) glass-ceramic of a glass composition formulated and studied during the masters studies. Color is due to the presence of TiO_2.

It is well known that transition metals may lead to color in glass [48]. In the case of the glasses studied here, the transition metals present are Ti and Zr. The ions Zr^{+4} and Ti^{+4} have an electronic configuration that does not allow electron transition on orbital d ($4d^0$ and $3d^0$ respectively), and thus would present no color. Ion Ti^{3+}, though, has an incomplete d orbital ($3d^1$) making

electron transition possible. Although Ti^{+4} does not present electron transition, there might be Ti – O charge transfer. The position of this charge transfer band changes according to the coordination of Ti^{+4}, if 4-, 5- or 6-fold coordinated.

Chavoutier et al. [48] studied the influence on color of systematic addition of TiO_2 on glasses of LAS system. The observed color changes were: from almost uncolored (in a glass with no TiO_2) to yellow-brown (in a glass with 4 mole % of it). They report no presence of Ti^{+3} on the glasses and the addition of TiO_2 lead to the shift of absorption band on optical transmission to higher wavelengths. Diffuse reflectance had shown that, with higher concentration of TiO_2, the environment of Ti^{+4} changes and their 3d orbitals are split into two groups. Charge transfer between 2p orbitals of oxygen and Ti^{+4} 3d orbitals are responsible for the color presented. Regarding glass-ceramics, Chavoutier et al. also analyzed the origin of the dark color of their samples. In their case, it was not due to the formation of Ti^{+3}, but to the scattering of the nanocrystals of the obtained glass phases.

Another possibility for the color of the glasses is the presence of Fe ions as impurity: both have incomplete d orbitals and absorb light at the visible range (Fe^{+3} has $3d^5$ electronic distribution and Fe^{+2} has $3d^6$), and by Fe – O charge transfer [48]. Fe^{+2} and Ti^{+4} may also exchange electrons if they are close enough in the glass structure.

The use of metallic particles as nucleating agents has been long known. Platinum is commonly applied to the crystallization of lithia-based glass ceramics [50-52]. Silver particles can also be used as nucleation sites in silicates. Although some color is associated with it [8], the amount added is in the ppm order, and thus the color would be less pronounced. The replacement of TiO_2 and ZrO_2 as nucleating agents for metallic silver was tested. Silver was added as $AgNO_3$.

3.3 Hardness

Hardness can be defined as the resistance of a material to the formation of a permanent imprint. It can be divided in 3 types: scratch resistance, impact

resistance and the resistance to indenter penetration. The last one is the most important to engineering projects and the tests (Knoop, Vickers, Brinell, Rockwell, Meyer, etc.) consist on penetrators of different shapes being pressed against the sample's surface, having an application rate, load and dwell time controlled. This work used a Vickers test to measure the hardness of glasses and glass-ceramics.

3.3.1 The Vickers Test

The Vickers hardness (Hv) test consists of a square-based diamond pyramid having a 136° angle between non-adjacent sides. This pyramid is forced against the mirror-polished surface of the sample and leaves an impression. The size of the impression and the load applied are used to calculate the hardness of the material. Fig. 3.6 presents the Vickers indenter and an example of an imprint [53].

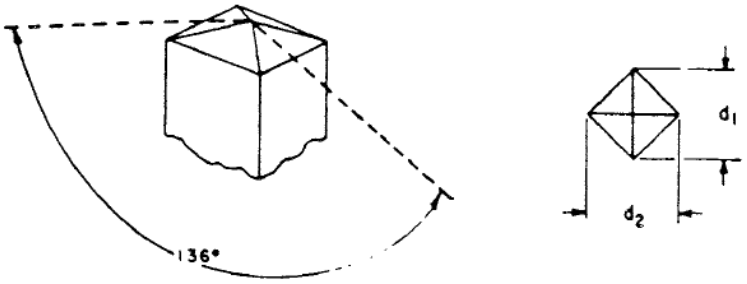

(a) (b)

Figure 3.6 (a) Vickers indenter tip and (b) indentation imprint [53]. d_1 and d_2 imprint's diagonals.

Having the mean value of the indentation diagonals and the applied load, the Vickers hardness is calculated as follows:

$$Hv = \left(\frac{P}{2a^2}\right) \tag{3.2}$$

where *P* is the applied load, in Newtons, *a* is the half-diagonal, in m. HV is given in GPa. The relation of the ratio of the applied load to the projected area is consistent with the definition of a normal stress and is independent of the indenter shape.

When pores are present, either on the surface or on the bulk of the sample, the measurement of the diagonals may be difficult. Fig. 3.7 present a series of acceptable and unacceptable imprints, according to American standard ASTM C 1327-08 [53].

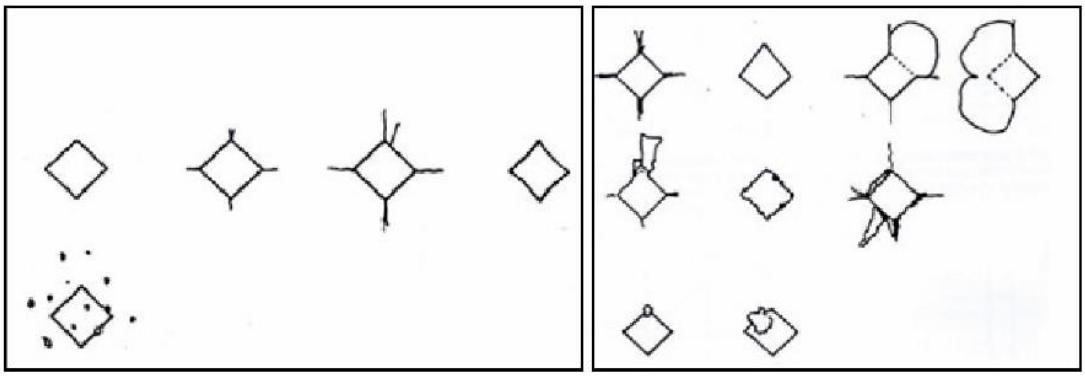

a) b)

Figure 3.7 a) acceptable and b) unacceptable imprints according to ASTM C1327-08.

This standard also states that there must be a safe distance between consecutive imprints. If no cracking is observed, a distance of 4 times the diagonal of the imprint (counting from the center) must be respected. When cracking occurs during the indentation test, the distance must be of 5c, also starting from the center of the imprints [53]. Fig. 3.8 summarizes these rules.

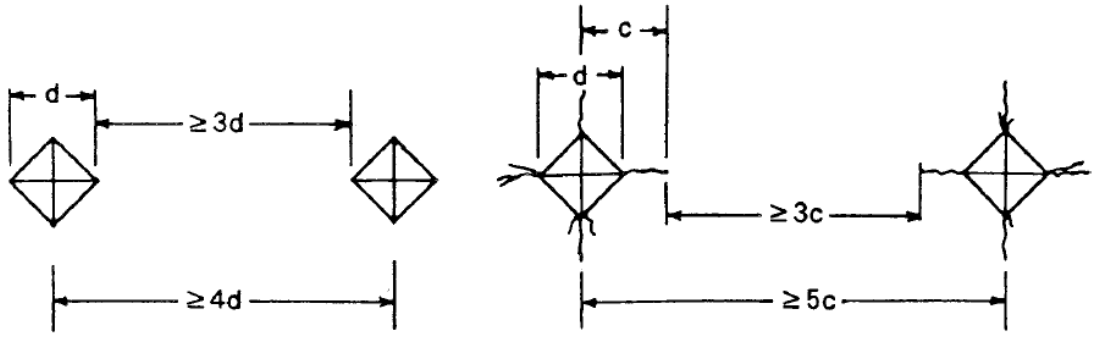

a) b)

Figure 3.8 Safe distance between consecutive imprints when a) no crack is present and b) cracks are present.

3.4 Fracture, Fracture Toughness

Fracture is the separation in two or more parts of a body, as a response to an imposed static stress, applied at low temperatures when compared to the melting of the material. It involves the formation and propagation of a crack due to applied stress. According to the presence or absence of plastic deformation, it is classified as ductile or fragile, respectively [54]. Ceramics have the tendency to break in a fragile, fast and catastrophic way, with little or no plastic deformation [55]. In fragile fracture, the crack propagates normal to the stress, producing a flat surface [54]. The maximum theoretical stress applied is based on the force of atomic bonds, given as follows:

$$\sigma_{theoretical} = \sqrt{\frac{E\gamma}{d_0}} \tag{3.3}$$

where γ is the energy associated to the creation of a surface and d_0 the interatomic equilibrium distance. To fracture a material, the energy involved must be enough to create two new surfaces [55].

When one measures the stress needed to break a material, one notices it is in the order of 100 times lower than the theoretical stress, sometimes even lower [54-56]. Griffith postulated that materials have pre-existing defects, and it is due to the stress concentration at these defects that the material will break at lower-than-theoretical tensions. Therefore, fracture is not seen as the separation of two perfectly set planes of atoms, but as the growth of a pre-existing crack [55]. When tension is applied, it is amplified at the tip of the defects, and the amplification will depend on the geometry and orientation of the defect. It is possible to correlate the critical tension for crack propagation to its length *l*:

$$K_c = Y\sigma_c\sqrt{\pi l} \tag{3.4}$$

where K_c is the toughness, the property that measures the resistance to fragile cracking when a crack is present, σ_c is the critical tension stress to crack propagation, *l* is the crack length and *Y* is a dimensionless parameter that depends both on crack size and geometry, as well as how the load is applied. For an infinite plate with a crack that crosses its thickness, *Y* = 1. When the plate is semi-infinite, Y ≈ 1.1.

When the thickness of the sample is orders of magnitude larger than the crack length, K_C becomes independent of the thickness and is named plane strain fracture toughness, K_{IC}. The subscript *I* indicates the mode of crack displacement, in this case, opening. There is also mode II, shearing, and mode III, tearing. Fig 3.9 presents the three cases.

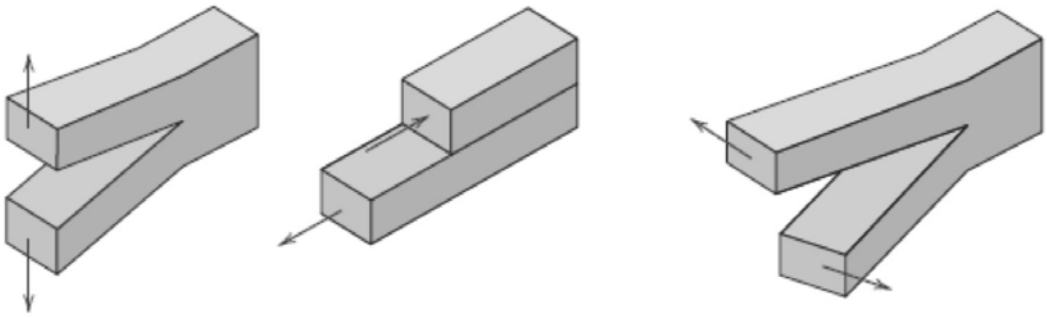

a) b) c)

Figure 3.9 Crack displacement modes. a) Mode I is crack opening, b) mode II is crack shearing and c) mode III is crack tearing [54].

3.4.1 The Single-Edge Precracked Beam Test

Single-edge pre-cracked beam is a suitable technique to measure toughness of glass and glass ceramic samples; a test that presents high reproducibility [57]. The test is relatively simple, fast, and easy; and the size of the samples are suitable for our studies. It requires accurately cut and shaped specimens as well as a fine surface finish allowing for a good positioning of the specimen in the testing set-up as well as for optical observation of the fractured region. To obtain K_{IC} by this technique, a series of aligned indentations are made on the surface of a sample. They will be the nucleating sites for the pre-crack, or pop-in crack (z). This surface is placed on top of an anvil with a groove and under a SiC bar, as shown in Fig. 3.10. Compressive load is applied on top of the SiC bar which uniformly distributes it through the sample. This technique is called bridge loading. The pre-crack appears and the load is released. This crack has the length of the sample and the difference between the lengths of the crack in two points must be less than 10% of the average [57].

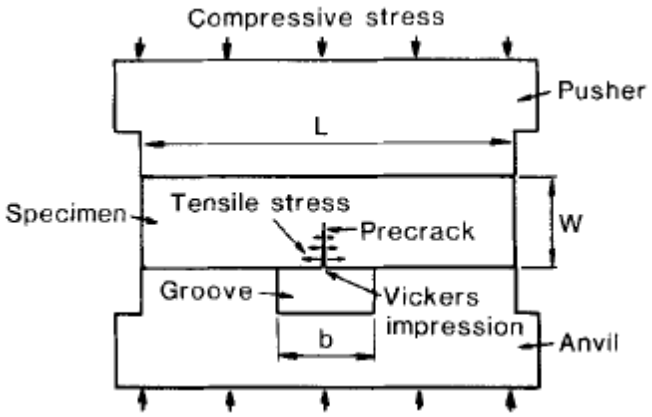

Figure 3.10 Schematic of the bridge indentation technique. The sample is placed between two SiC bars (pushing and anvil). The bar at the bottom has a groove of 3.4 mm to induce tensile stress at the lower surface of the sample [58].

A 3-point bending test is then performed to fracture the sample. The size of the pre-crack, the fracture load, the span size of the 3-point bending test, and the sample's thickness and width are taken into account to calculate toughness. The equation to calculate K_{IC} depends on the size of the pre-crack related to the sample's width. Equation 3.5 [57] was the one used in this study.

$$K_{IC} = \frac{P_f S}{B W^{1.5}} f\left(\frac{z}{W}\right) \tag{3.5a}$$

$$f\left(\frac{z}{W}\right) = \frac{3\left(\frac{z}{W}\right)^{\frac{1}{2}}\left[1.99 - \left(\frac{z}{W}\right)\left(1 - \left(\frac{z}{W}\right)\right)\left(2.15 - 3.93\left(\frac{z}{W}\right) + 2.7\left(\frac{z^2}{W^2}\right)\right)\right]}{2\left(1 + 2\left(\frac{z}{W}\right)\left(1 - \left(\frac{z}{W}\right)\right)^{\frac{3}{2}}\right)} \tag{3.5b}$$

were P_f is the maximum fracture load, *S* is the support span, *B* is the specimen thickness, *z* is the size of the pre-crack and *W* is the specimen width. Equation 10 is valid in the case when the support spam is 4 times the specimen thickness.

Attention must be paid to some key factors on the test. One of them is the inclination of the pre-crack, which must be formed vertical to the crack propagation direction [57]. Another one is the inclination of the fracture surface after the 3-point bending test, which must be parallel to a degree of ± 10° to the sample's width and thickness [58].

The size of the pre-crack can be modified by changing the load of the Vickers imprint on the surface of the sample, being larger for lower indentation loads [58]. Groove size also affects z size. The larger the groove, the larger z. For materials that do not present R-curve behavior, pre-crack size does not affect the values of K_{IC} for z > 1 mm [58]. In this study, pre-crack size was always larger than 1 mm.

3.4.2 Toughness Measurements Via Vickers Hardness

The cracks generated on a Vickers hardness test are frequently used to calculate the fracture toughness of a material. It is particularly used by the glass and ceramic community because it is a fast-performing, low-cost test [59-64]. The first equations trying to correlate those cracks with K_{IC} were proposed by S. Palmqvist back in 1957, studying metallic carbides. He was also the first to propose important parameters on the cracking process, like the materials' hardness [59-61]. Evans and Charles, studying from monocrystalline oxides to carbides during the 1970's, proposed the first equations relating mechanic tests with the cracks [61]. Ever since, this estimation became popular among the scientific community [61, 62, 65].

Fig. 3.11 presents the five types of crack that can be originated after a hardness test. Cone cracks are generated on the surface at a specific angle, loading a spherical indenter (Brinell indenter). Radial cracks, or Palmqvist cracks, are generated after loading a sharp indenter tip, like Knoop or Vickers, on the sample. Median cracks are generated parallel to the load axis, under the plastic deformation zone, having the shape of a circle. The origin of half-penny crack is uncertain. It is not known if it is the final morphology of median crack that grows to the surface, if it is due to the propagation of radial cracks on the

volume of the material, or even if it is the coalescence of these two types of cracks. The last type of crack is the lateral crack, which is also formed under the plastic deformation zone and grows parallel to the surface, having a circular shape [66].

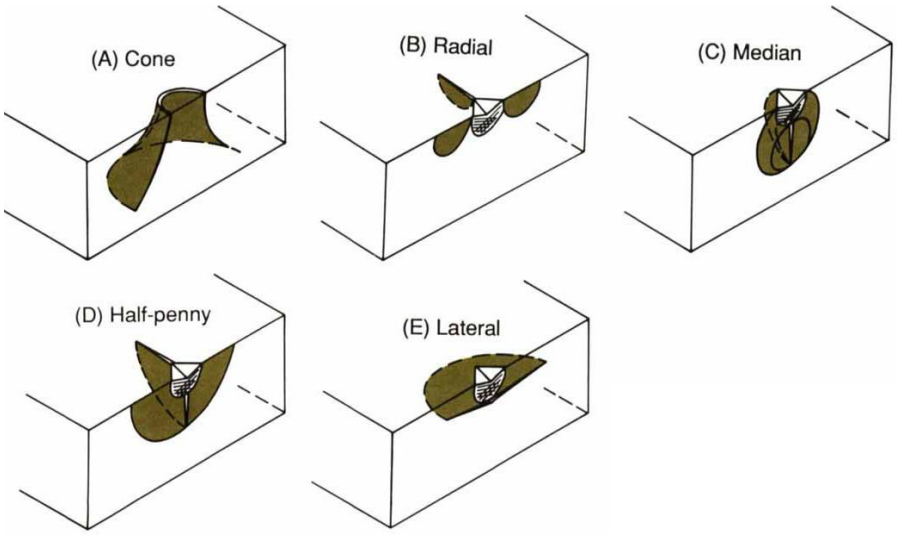

Figure 3.11 Possible types of crack that appear after an indentation test [66]. a) cone crack appears when a round tip indenter is used. All others appear when a sharp indenter is used.

The stress field generated during an indentation gives rise to a series of different equations [63], each one with its own suppositions [64]. Fig. 3.12 presents median and Palmqvist cracks and the parameters involved. In this work, the Niihara equation [65] was adopted when median cracks occurred.

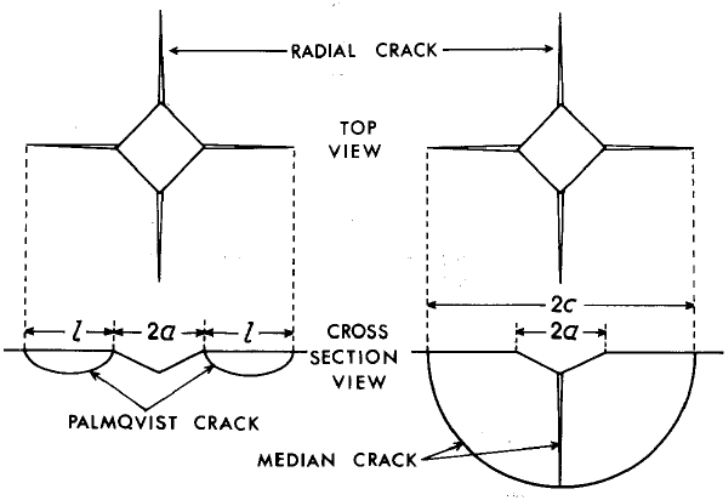

Figure 3.12 Palmqvist and median cracks. a is half the diagonal of impression, l is the crack length and c = l + a [65].

This equation is applied when 0,25 < *l/a* < 2,5 [63]:

$$K_C = 0.035\left(\frac{l}{a}\right)^{-\frac{1}{2}}\left(\frac{H_0}{\Phi E}\right)^{-0,4}\left(\frac{H_0 a^{\frac{1}{2}}}{\Phi}\right) \tag{3.6}$$

where *l* is the crack length, *a* is half of the diagonal imprint, H_0 is the material's hardness, *E* is the material's Young's Modulus, and Φ is a restriction factor that can be approximated to 3.

When the ratio $\frac{P}{c^{3/2}}$ is constant, the cracks in the material are median and the equation proposed to this type of crack is the following, by Anstis et. al [60]:

$$K_C = 0.016\left(\frac{E}{H_0}\right)^{1/2}\frac{P}{c^{3/2}} \tag{3.7}$$

It is important to mention that the values obtained applying equations 3.6, 3.7 or any other relating cracks that appear after a hardness test to fracture toughness do not reflect the real value of K_{IC}. Quinn and Bradt [61] say that the stress field generated during a hardness test is not the same as the one that

appears after a standard toughness test, such as single-edge pre-cracked beam (SEPB) or single-edge V-notched beam (SEVNB). Serbena et. al [67] observed such differences studying the mechanical properties of lithium dissilicate glasses and glass-ceramics. In this study, the authors kept the crystal size constant and varied their volume fraction. Indentation fracture toughness (IFT) was measured applying eq. 3.6 and another one proposed by Niihara. The IFT values present themselves different according to the load applied at the hardness test. Moreover, they are not in accordance with the standardized double torsion test they performed. Another point of conflict was that the K_{IC} value, obtained by standardized test, constantly increased with the growth in crystal volume fraction, but the K_C value, at some point, depending on the load applied and the equation used, reached a saturation value. Other complications are inherent to the technique [59-61, 68].

The measurement of IFT was used in this work just to have an idea of the resistance to crack propagation of the developed glass-ceramic, but only hardness values were taken into account to further design the experiments.

3.5 Young's Modulus, *E*, Shear Modulus, *G*, And Poisson's Ratio ν

Two independent elastic moduli are sufficient to fully describe the elastic behavior of a homogeneous isotropic materials. For example, Young's modulus (E) and shear modulus (G). Other parameters, such as the bulk modulus and Poisson's ratio are directly obtained from E and G. A material under the application of tensile stress may deform elastically or plastically, depending on the intensity of the stress. When deformation lies in the elastic regime, there is proportionality between the stress and strain, proposed by Hooke [54, 56]:

$$\sigma = E.\epsilon \tag{3.8}$$

where σ is the tensile stress, ϵ is the strain and E Young's Modulus.

Young's modulus is an indicative of the atomic bonding force and can be calculated as the slope of the stress *versus* strain curve under the elastic

regime, as shown in Fig. 3.13 a) [54]. Fig. 3.13 a) also represents a typical curve for ceramics, since they do not present significant plastic deformation. For dense polycrystalline ceramics, *E* is in the range of 100–800 GPa and for silicate glasses from 60–80 GPa [56].

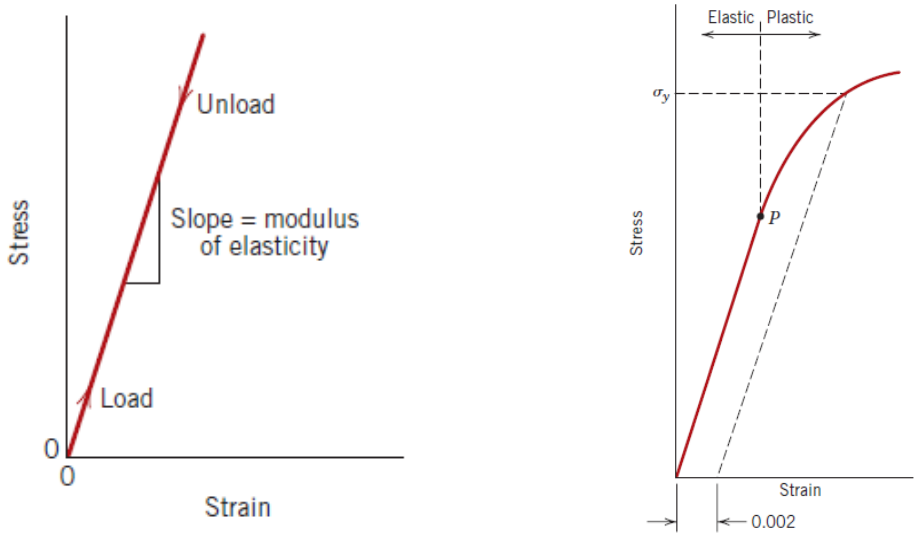

Figure 3.13 Typical Stress x strain curve on elastic regime for a) ceramics and b) metals [54].

Some materials, such as some metals and polymers, do not present a straight line at the stress *versus* strain curve on the elastic regime. For those, one can calculate the tangent or secant modulus. On the first case, the modulus is calculated tracing a straight line from the origin of the system to the point where the line intersects the curve at the desired stress value. On the second, it is calculated the derivative of the curve on the desired stress value.

When it comes to glasses, Young's Modulus may change significantly with their composition. For example, amorphous Selenium have E = 10 GPa, while a composition from the YSiAlON glass system may present E = 165 GPa [69]. High-E glasses find applications, for instance, on computer hard disks [69]; lowering the weight of windows; increasing structure stiffness; designing glasses and glass-ceramics with better thermomechanical properties [70]. Since Young's Modulus is an indicative of the atomic bonding energy, one would expect that a High-E glass would also present high glass transition temperature. Not always does that relation stand, though. For example, a-SiO_2

has glass transition of over 1100 °C, but because of its low atomic packing density, it presents a relatively low E when compared to oxycarbides [69, 70]. Fig. 3.14 presents the relation of Young's modulus with Tg [70]. The dashed line represents *E* of window glass, of approximately 75 GPa.

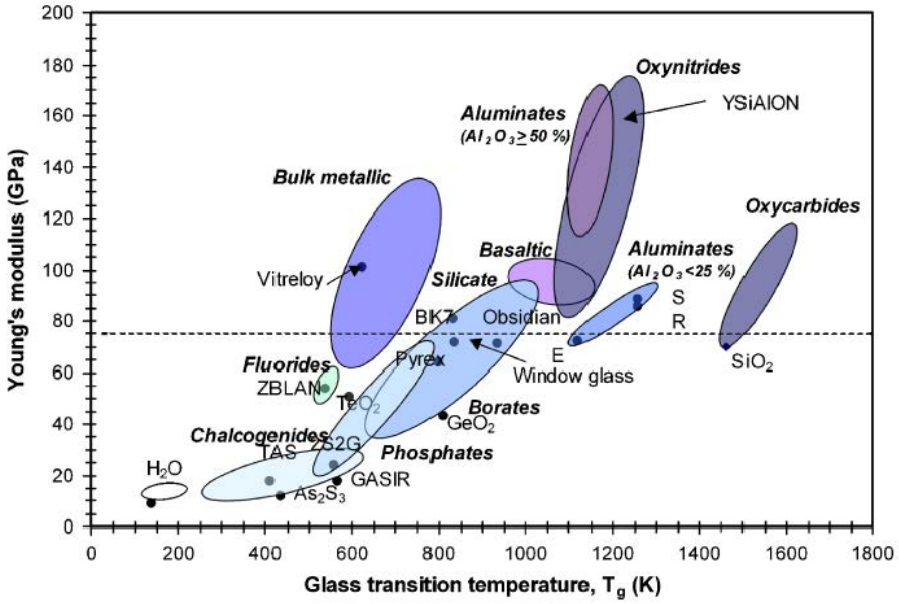

Figure 3.14 Relation between Young's modulus and the glass transition temperature of several glass systems. Values at room temperature, except for glassy H_2O (taken at -196 °C). Some comercial glasses are also indicated [70].

Not only with composition does Young's modulus change, but also with temperature. As temperature increases and the structure starts to soften, Young's modulus's value tends to decrease. Depending on the composition, the decrease speed may vary. And this change is more pronounced at higher-than-Tg temperatures. Also, depending on composition, E values may increase with temperature, like what is observed in vitreous silica; or remain almost unchanged for a certain temperature interval, as is the case of SiOC [70]. Figure 3.15 presents several glass compositions and how their E change with temperature.

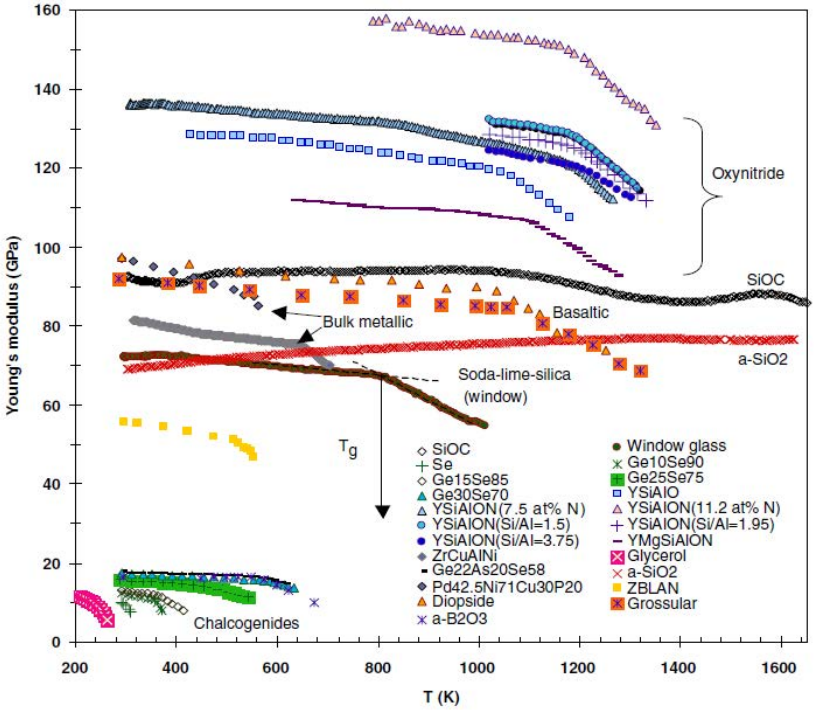

Figure 3.15 Temperature dependence of Young's modulus. Compiled by Rouxel [70].

One could expect that when other types of forces are applied, other proportional constants are obtained. When shear stress (τ) is imposed on the elastic regime, the following proportionality is valid:

$$\tau = G.\gamma \tag{3.9}$$

where G is called shear modulus (also represented as μ) and γ is the shear deformation. For ceramics, the ratio $\frac{E}{G} \approx 0.4$ [69].

The last possible type of deformation, isostatic compression, gives rise to the forth elastic constant, the bulk modulus (B), defined as the ratio of applied pressure P and the volume deformation ΔV/V.

Taking the application of a uniaxial tensile stress on the elastic regime, there is a strain on the body parallel to the stress application axes, say ϵ_Z. As a response, to maintain the volume constant, lateral deformation on X and Y axes also appear, ϵ_X and ϵ_Y. These deformations are perpendicular to the applied

stress axis. If the material is isotropic, that is, it presents the same physical properties regardless of the orientation, then ϵ_X = ϵ_Y. Poisson's ratio (ν) is defined as "*the negative of the ratio of transverse contraction strain to longitudinal extension strain in the direction of elastic loading*" [70]. This is mathematically expressed as:

$$\nu = -\frac{\epsilon_X}{\epsilon_Z} = -\frac{\epsilon_Y}{\epsilon_Z} \tag{3.10}$$

The negative sign is applied in order to always have positive values of ν. Poisson's ratio for isotropic materials lies between -1 ≤ ν ≤ 0.5 [56, 70], for ceramic materials generally lies from 0.2 to 0.3 [69] and for glasses from 0.1 to 0.4 [70]. Negative values of Poisson's ratio indicate that, with the application of a tensile stress on Z axes, there is an expansion (instead of a contraction) on X and Y axis. This happens in some polymeric foams, for instance [70].

This constant is an indicative of the material's atomic packing density (C_P) and network connectivity. Highly packed structures (C_P > 0.6) tend to have ν close to 0.4. A highly cross-linked structure, on the other hand, tend to present a low ν [70]. If the material is isotropic, Young's Modulus and shear modulus can be related to Poisson's ratio as:

$$\nu = \frac{E}{2G} - 1 \tag{3.11}$$

Poisson's ratio also changes considerably with composition and temperature. Fig 3.16 presents the variation of ν with normalized temperature (T/Tg) for several organic, inorganic and metallic glasses [70]. The behavior above T/Tg = 1 is divided in strong and fragile glasses. Strong are those that present a low degree of depolymerization above Tg and fragile are those which present the opposite behavior.

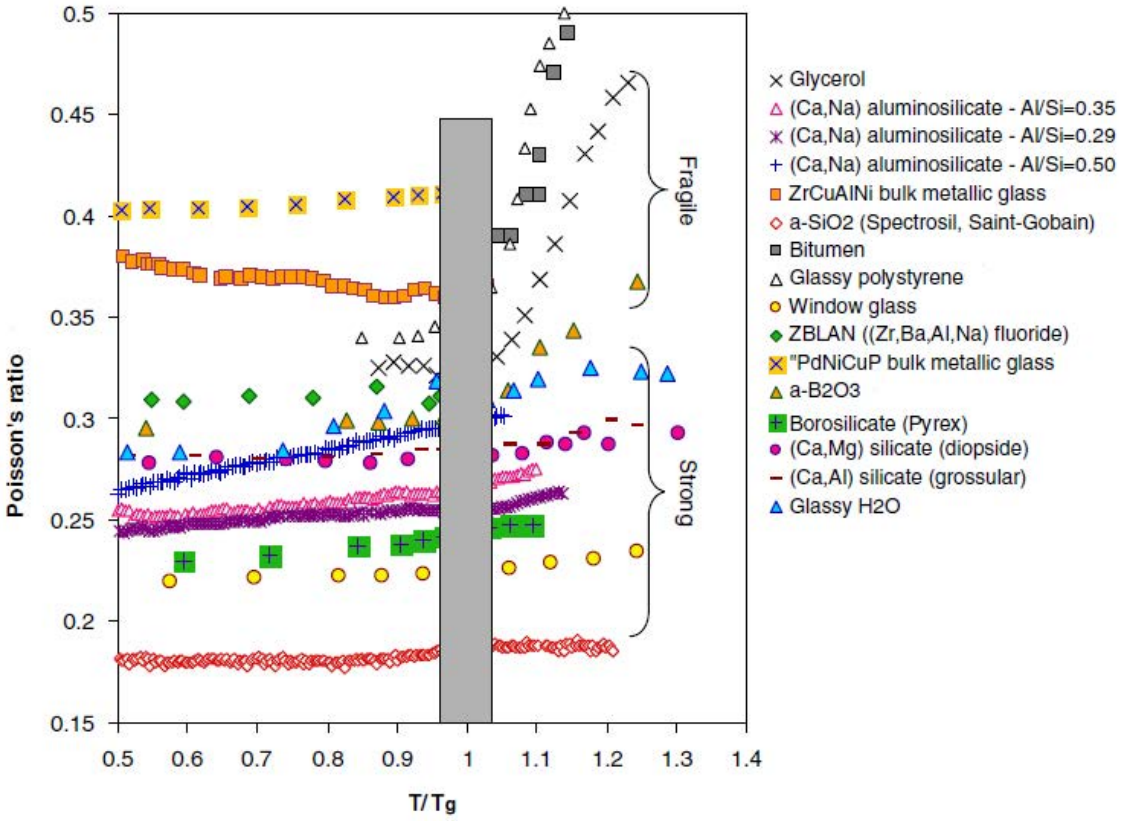

Figure 3.16 Poisson's ratio temperature dependence for several glass systems. Data compiled by Rouxel [70].

3.5.1 The Resonance Spectroscopy

There are three types of experiments that one can conduct to obtain the elasticity moduli of a material: quasi-static, dynamic and ultrasound. In this work, dynamic tests were conducted. They consist of the calculus of E and G via the resonance frequencies of the analyzed body (resonance spectroscopy). In this test, a suspended sample (a bar, cylinder or a disc) is tapped to induce vibration, which has a specific frequency spectrum, according to its resonance frequency. Figure 3.17 shows the two types of mechanical vibration modes on a rectangular specimen: flexural and torsional. The first is used to calculate Young's modulus; and the second, shear modulus.

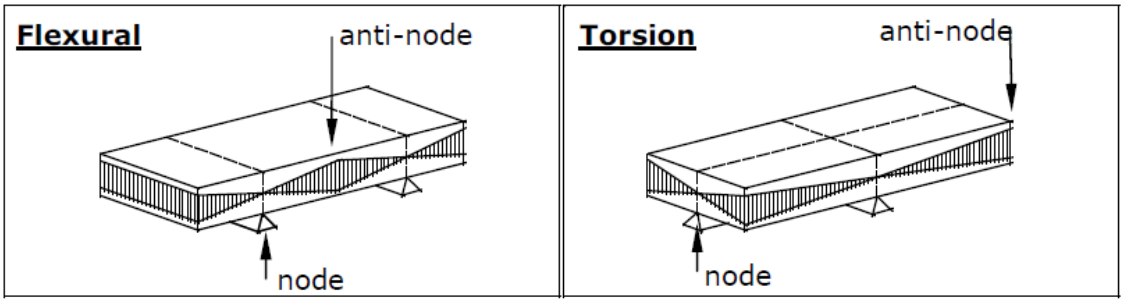

Figure 3.17 Flexural and torsion vibration modes of a rectangular bar [71].

The resonance frequency depends on the elastic properties and on the density of the material and the geometry of the sample, and will dump according to the absorption of the material. If the material has large or small grains, crystals or defects of any kind, it will affect the dumping. A transducer detects the vibration and produces an electrical signal that is sent to the electronic part of the experiment. E, G and ν can then be calculated.

The sample is tapped by hand or, for high temperature measurements, with a rod at its node. The generated vibration is independent of the intensity of the impulse. Care must be taken not to tap it too gently, or the vibration is not detected; or too hard, for the sample will not move, or might even break.

Detection of the vibration happens with the aid of a transducer, which can be a piezoelectric sensor, a microphone or a laser vibrometer. In this work, a microphone was used. Once flexural and torsional resonant frequencies are known, E, G and *v* can then be calculated. According to ASTM E 1876 [72], for a rectangular bar, one has:

$$E = 0.9465\left(\frac{m.f_f^2}{b}\right).\left(\frac{L^3}{t^3}\right).T_1 \tag{3.12a}$$

$$T_1 = 1 + 6.585.(1 + 0.0752\nu + 0.8109\nu^2).\left(\frac{t}{L}\right)^2 - 0.868\left(\frac{t}{L}\right)^4 - \left[\frac{8.34.(1 + 0.2023\nu + 2.173\nu^2)\left(\frac{t}{L}\right)^4}{1 + 6.338.(1 + 0.1408\nu + 1.536\nu^2)\left(\frac{t}{L}\right)^2}\right] \tag{3.12b}$$

where ν is Poisson's ratio; *m* is the mass of the bar (g); *b* is the width of the bar (mm); *L* is the length of the bar (mm); *t* is the thickness of the bar (mm); f_f is the fundamental flexural resonant frequency of the bar (Hz) and T_1 is a correction factor.

$$G = \frac{4.L.m.f_t^2}{b.t}\left[\frac{B}{1+A}\right] \tag{3.13a}$$

$$A = \frac{\left[0.5062 - 0.8776.\left(\frac{b}{t}\right) + 0.3504\left(\frac{b}{t}\right)^2 - 0.0078\left(\frac{b}{t}\right)^3\right]}{12.03.\left(\frac{b}{t}\right) + 9.892\left(\frac{b}{t}\right)^2} \tag{3.13b}$$

$$B = \left[\frac{\frac{b}{t} + \frac{t}{b}}{4\frac{t}{b} - 2.52\left(\frac{t}{b}\right)^2 + 0.21\left(\frac{t}{b}\right)^6}\right] \tag{3.13c}$$

where f_t is the fundamental torsional resonant frequency of the bar (Hz), *B* is a correction factor and *A* a correction factor dependent on the width-to-thickness ratio.

4 MATERIALS AND METHODS

4.1 Composition Reformulation And Melting

The compositions studied during the masters were reformulated in an attempt to obtain transparent and less colored glass ceramics. The oxides present at the original formulations are MgO, Al_2O_3, SiO_2, Sb_2O_3, TiO_2, ZrO_2 and B_2O_3. Two lines of work were analyzed. In the first one, shown in section 5.2, the glasses had the same constituents as the ones studied in the masters, but the amount of TiO_2 was diminished. However, the sum TiO_2 + ZrO_2 was kept constant and equal to the parent compositions. The two first reformulations originated the glasses dubbed ZT1B4, formulated after L2R4 original composition; and 75-25/ZT, formulated after 75-25 original composition.

The ZT1B4 raw material, after 5 minutes of milling in an agate jar at 350 rpm to have better homogenization, was calcinated at a sequence of temperatures: 1373 K for 4.5h; followed by 1423 K, then 1473K, and finally 1523 K for 2h. This was to promote the initial kinetics to form the crystalline phases that would be perceived after heat-treatments. After the described periods at each temperature, an exploratory XRD analyses was conducted to see if the raw material had crystalline fraction. Only after 2h at 1523 K some crystal phase was observed. This powder was once again milled and melted in a Deltec furnace, Deltec INC. USA, model DT-33-RS-812C, having Super Kanthal resistance, in a Pt crucible, at 1853 K for 4h. Annealing was conducted in a EDG 1800 furnace, EDG Equipamentos, Brazil, at 943 K for 2h, the furnace was cooled to room temperature at the rate of 3 K/min.

The 75-25/ZT raw material underwent a similar protocol. It was milled in an agate jar for 3 cycles of 5min each at a 350-rpm speed. Calcination was carried at 1373 K for 2h and subsequent 2h at 1523 K. The powder was milled once again and melted at 1873 K for 4h. After annealing at 943 K for 2h, the furnace was cooled to room temperature at 3 K/min. This glass composition also originated another one, named 75-25/25Ti, with higher content of ZrO_2 than TiO_2. The raw materials were dry-mixed for 5h. Melting occurred at 1893 K for 4h. The glass was annealed at 923 K for 3h and the furnace was then cooled to room temperature at 3 K/min. Because the glass was still fragile due

to residual tension, another annealing was conducted at 1003 K for 3h, with the cooling of the furnace happening at 3 K/min.

At the second line, presented in section 5.3, the nucleating agents (TiO_2 and ZrO_2) were substituted by $AgNO_3$. The idea was to have metallic silver as nucleating agent. Four glass compositions having MgO, Al_2O_3, SiO_2, Sb_2O_3 and B_2O_3 as constituents were prepared, with excess of $AgNO_3$ being added. The raw materials were dry-mixed for 8h at 120 rpm. The glasses were melted at 1823 K for 3h and annealed at 923 K for 2h, then cooled down at 3 K/min.

4.2 Characterization Of Parent Glasses And Glass-Ceramics

After the melting of a new composition, a differential scanning calorimetry (DSC) analysis was conducted to observe the thermal profile of the glass. The equipment used was a NETZSCH DSC 404, Netzsch, Germany. When the glass was crystallized, the crystalline phases present at the originated glass-ceramics were identified by X-ray diffraction at a Rigaku Ultima IV equipment, Rigaku, Japan, using Cu-Kα radiation. The analyses were conducted using step scan with a 0.02° step and 2s count time. These series of analyses were conducted at Vitreous Materials Laboratory (LaMaV) of the Federal University of São Carlos.

High temperature X-ray diffraction (HTXRD) was conducted for the bulk samples using a D8 X-ray diffractometer (Bruker AXS), using monochromatic Cu-$K\alpha_1$ radiation by means of an incident beam Ge monochromator, a Lynx Eye detector and a HTK1200 heating chamber (Anton Parr). The XRD was recorded over the 10-80° 2θ angular range, with a step of 0.02° 2θ, and an acquisition time of 0.5s per step. An initial run without any isothermal plateau was performed on a bulk sample heated from room temperature to 773 K at a fast rate of 9 K/min (no XRD was recorded at this stage) and from 773 K to 1320 K at a much slower heating rate of 0.42 K/min. These conditions were employed because no crystallization is expected below 773 K. For these experimental conditions, each diagram required approximately 30 min to be recorded and 48 patterns were recorded during this heating step.

The second analysis was conducted using two temperature steps (double-stage heat treatment). The sample was heated from room temperature to 873 K at 7.2 K/min and then to 1006 K at 0.9 K/min. The temperature of 1006 K is the glass transition temperature, T_g, as measured by DSC for a heating rate of 10 K/min. The sample was maintained at 1006 K for 48h to promote nucleation before being heated using a 2.7 K/min rate until the sample reached 1173 K. The sample was then held at this temperature for 10h to promote crystal growth. Each pattern was recorded over the 10-80° 2θ range, with a step of 0.02° 2θ, and a step time of 0.5s. The specimen was then rapidly cooled to room temperature. This heat treatment protocol was also applied to the high-temperature *in situ* measurements of the elastic moduli.

These two analyses were performed to observe the differences in crystallization, differences in the obtained crystalline phases during single- and double-stage heat treatments. The HTXRD was performed at the Institute of Chemical Sciences of the University of Rennes 1, under the supervision of Prof. Dr. Nathaly Audebrand, who assisted me on several analyses and interpretations, and with whom I had fruitful discussions.

Room temperature analyses of raw powder and glass-ceramic samples were conducted at the Vitreous Materials Laboratory of the Federal University of São Carlos, in an Ultima IV X-Ray equipment from Rigaku, Japan, that uses Cu-Kα radiation.

4.3 Thermal Heat Treatments

In Brazil, the thermal heat treatments to crystallize the glass at different temperatures and for different times were carried out in a furnace manufactured at the Vitreous Materials Laboratory, which has Kanthal A1 resistance that can go up to 1273 K. In France, crystallization heat treatment was conducted in a Nabertherm furnace model L3/12/P320. Four glass samples were submitted to a thermal cycle of heating from room temperature to 873 K with a 7.2 K/min rate, and further from 873 K to 1006 K (nucleation temperature) with a 0.9 K/min rate. Temperature was kept at 1006 K for 48h and then increased up to 1173 K

(crystal growth temperature) with a 12.7 K/min rate. The duration of each treatment at 1173 K was 31 min, 61 min, 92 min and 153 min. This heating cycle is the same as the one employed for elastic moduli measurements at high temperatures and also HTXRD.

4.4 Sample Preparation And Optical And Electronical Microscopy

Optical grade polishing was achieved using sandpaper graded from 120 to 1200 and subsequent polishing on a Montasupal polishing machine, model 110. For the polishing, diamond suspension having particle size 9, 3 and 1 μm were used. Transmission electron microscopy (TEM) was conducted in a TECNAI G^2 F20 microscope, FEI Company, USA, located at the Structural Characterization Laboratory (LCE) of the Materials Engineering Department of the Federal University of São Carlos. TEM analyses were also conducted in a TEM-FEG JEM 2100F microscope, Jeol, Japan, at the Brazilian Nanotechnology National Laboratory (LLNano) from the Brazilian Materials and Energy National Research Center (CNPEM) in Campinas, São Paulo State. Sample preparation for the TEM analyses consists of hand milling the sample, mixing it with alcohol and letting it rest for about 10 min. The supernatant of this solution was dropped on a 300 mesh Cu grid and put in a plasma cleaner to prepare for the analysis. The analyses at the LLNano were made possible due to the assistance of Dr. Jefferson Bettini.

4.5 Vickers Hardness Measurements

The Vickers hardness measurements of glasses and glass-ceramics were conducted at LaMaV, in a Future-Tech F-7e microindenter, Japan. The applied load to perform the measurements was 4.9 N and the dwell time at peak load was 20s. The diagonals were measured with LAS software version 3.7.0, from Leica Microsystems. At the Department of Mechanics and Glasses of the University of Rennes 1, hardness measurements were conducted in two equipments. For an applied load of 600 and 1000 mN, the tests were conducted in a Fischerscope HC100 instrumented indenter. The dwell time at peak loads

was set at 5s, while the loading and unloading stages lasted for 20s. These loads were used to measure Vickers hardness of glass samples only. For larger loads, ranging from 4.9 to 196.1 N, a Matsuzawa microindenter, Japan, was used. The dwell time at peak loads was set at 15s. These increased loads were used to indent the glass and the glass-ceramics. Micrographs and measurements of crack size and diagonal impression were conducted using cell^{A} software, from Olympus BioSystems GmbH. Experimental errors associated with the measurements are image resolution and operator's skills to perform the aforementioned measurements.

4.6 Indentation Fracture Toughness Measurements Via Vickers Hardness Test

Indentation fracture toughness will be calculated using the cracks that appears after a hardness test, according to what was proposed at 3.4.2.

4.7 Elastic Properties Measurements

E, G and ν were also calculated at high temperatures (up to 1173 K) using flexural and torsional frequencies [72] by resonance spectroscopy, in a Nabertherm furnace, Germany, controlled by a RFDA HT1050 software. Sample dimensions were 25.2 x 43.55 x 3.57 mm^3. E and G values were used to calculate Poisson's ratio, according to equations 3.12; 3.13 and 3.11, respectively.

The glass sample was heated from room temperature to 873 K at 7.2 K/min and then to 1006 K at 0.9 K/min. The sample was maintained at 1006 K for 48h to promote nucleation before being heated using a 2.7 K/min rate until the sample reached 1173 K. Temperature was maintained at 1173 K for 10 h to promote crystal grow. Then the sample was cooled to room temperature at a 5 K/min rate. The heating cycle was chosen to match the one for the HTXRD and a measurement was made every 30 s.

4.8 Fracture Toughness Measurements

Fracture toughness measurements were conducted in glasses and glass-ceramic samples having approximately 2.5x3.5x20 mm^3, using SEPB method with a 20 mm-span 3-point bending support. A series of aligned Vickers indentations, ranging from 8 to 11 indents depending on the size of the sample, spacing 250 μm each, were performed using a Matsuzawa microindenter model MXT 70. The applied load was 9.81 N.

Using a Lloyd universal testing machine, a pre-crack emerged from the imprints after applying a compressive load using the bridge indentation technique, as shown in figure 3.10. To generate the pre-crack, the following loading cycle was used: i) compressive stress under the rate of 0.5 mm/min until 500 N; ii) compressive stress under the rate of 0.1 mm/min until visual observation of the pre-crack. Then the samples were submitted to the 3-point bending test in an Instron universal testing machine model 1380, a loading rate of 0.5 mm/min. Fracture toughness was calculated according to equation 5, presented at 3.4.1.

4.9 Visible Light Transmission Measurements

Light transmission at the 380 – 780 nm range was conducted at LaMaV, using a UV/VIS Spectometer Lambda 20 (1nm), from Perkin Elmer, USA.

5 RESULTS AND DISCUSSION

For better understanding and easier follow up of the results, this chapter is divided into 3 parts. Part A shows the results concerning the mechanical properties investigation of composition 75-25. This composition was studied during the masters and its crystallization and hardness is well known. That is the reason why it was chosen for further analysis at the Department of Mechanics and Glasses of the University of Rennes 1. High-temperature E, G and ν, HTXRD and K_{IC} measurements were conducted in France. Part B concerns the reformulation of the glasses studied during the masters, L2R4 and 75-25, with the attempt to obtain a less colored but still transparent and hard glass-ceramic. The reformulations concerned the change in the amount of TiO_2 and ZrO_2. Part C concerns the reformulation of a glass composition similar to L2R4 and 75-25 and primarily studied by the undergraduate student Carlos Eduardo de Meo during his internship at LaMaV. This formulation, dubbed 80-20 and originated after a reformulation of composition 75-25, had TiO_2 and ZrO_2 replaced by $AgNO_3$ in order to have metallic Ag as nucleating agent. Fig. 5.1 presents a flowchart to better understanding.

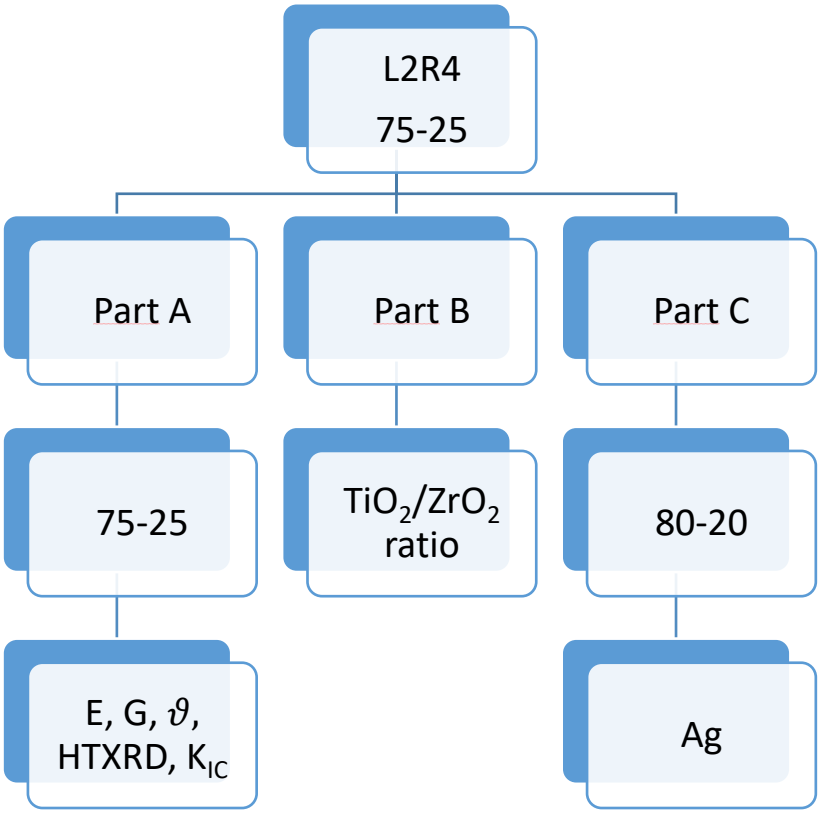

Figure 5.1 Flowchart of experiments.

5.1 Part A

The glass composition 75-25 was studied during the masters and can originate either transparent and opaque glass-ceramics. After single-stage heat treatments, opaque glass-ceramics were originated and hardness increased from to 6.78 ± 0.04 GPa (glass) to 8.5 ± 0.1 GPa after 180 min at 1283 K, temperature close to the second crystallization peak. After double-stage heat treatments with nucleation treatments at two different temperatures (T_{n1} = 966 K and T_{n2} = 1006 K) and growth treatment at T_c = 1173 K, transparent glass-ceramics were originated and hardness increased to 9.88 ± 0.08 after 300 min at 1006 K and 3h at 1173 K. Table 5.1 presents the composition of the analyzed glass. Titania and zirconia were used as nucleating agents and are highlighted in the table.

Table 5.1 75-25 glass composition.

Oxide	mol%	wt%
Al_2O_3	17.67	26.15
SiO_2	55.52	48.41
MgO	16.66	9.74
TiO_2	06.90	08.00
ZrO_2	00.50	00.89
Sb_2O_3	1.25	5.29
B_2O_3	1.50	1.52

5.1.1 Thermal Characterization And HTXRD

Figure 5.2 shows the DSC traces for the bulk and powder samples. The coincidence of the curves is indicative of the copious internal nucleation that is desirable when crystallizing a glass to produce GCs for technological applications due to the ease of microstructure control and reproducibility. The glass exhibits three crystallization peaks up to 1473 K, as shown in fig. 5.2. The glass transition temperature, T_{gDSC}, obtained using the tangent rule is ≈1006 K.

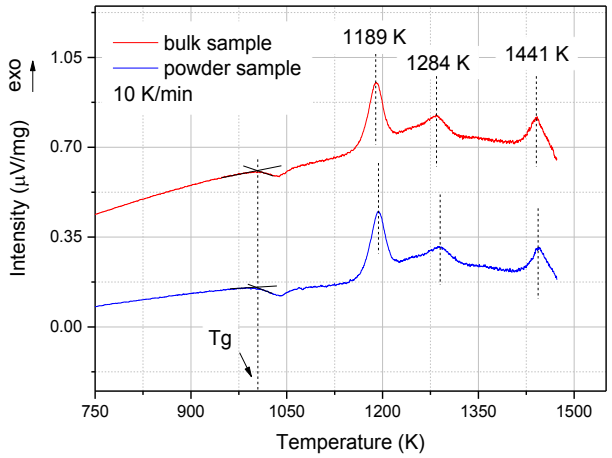

Figure 5.2 DSC analysis of composition 75-25.

Crystallization peaks appear at 1189 K, 1284 K and 1441 K. Following the results of the initial HTXRD run (data not shown), the first peak corresponds to the precipitation of β-quartz (International Centre for Diffraction Data, ICDD PDF2 file 89-8951). The second peak is broader and may correspond to the precipitation of three different crystalline phases that were detected in a 50 K-interval centered at the peak temperature: TiO_2 (ICDD PDF2 file 89-6975) at 1230 K, ringwoodite (γ-2MgO.SiO_2, ICDD PDF2 file 74-1681) at 1243 K and sapphirine ($4MgO.5Al_2O_3.2SiO_2$ – ICDD PDF2 file 11-0607) at 1282 K. The crystalline phase responsible for the third crystallization peak could not be detected due to the temperature limitation of the XRD diffractometer.

An HTXRD experiment with two temperature steps was also performed. After the nucleation stage at 1006 K for 2 days, the XRD pattern showed no diffraction peaks, indicating that the nucleated crystals had a low volume fraction that was below the limit detectable by the technique. The temperature was then raised to 1173 K, which is just below the first crystallization DSC peak. The crystal growth kinetics were monitored at this temperature for 10h. The XRD patterns collected during the first 92 min and after 9h and 42 min are shown in Figs. 5.3 a) and 5.3 b), respectively.

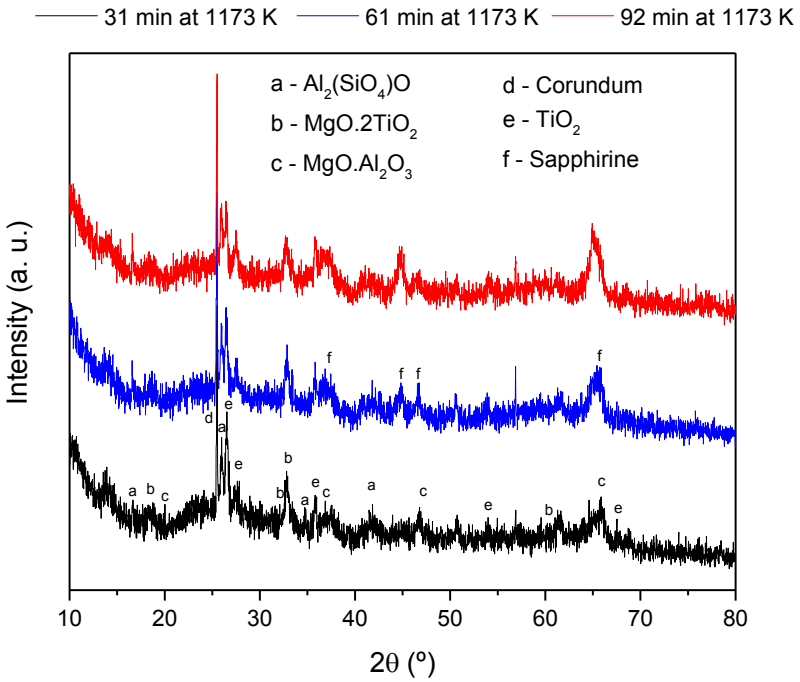

a)

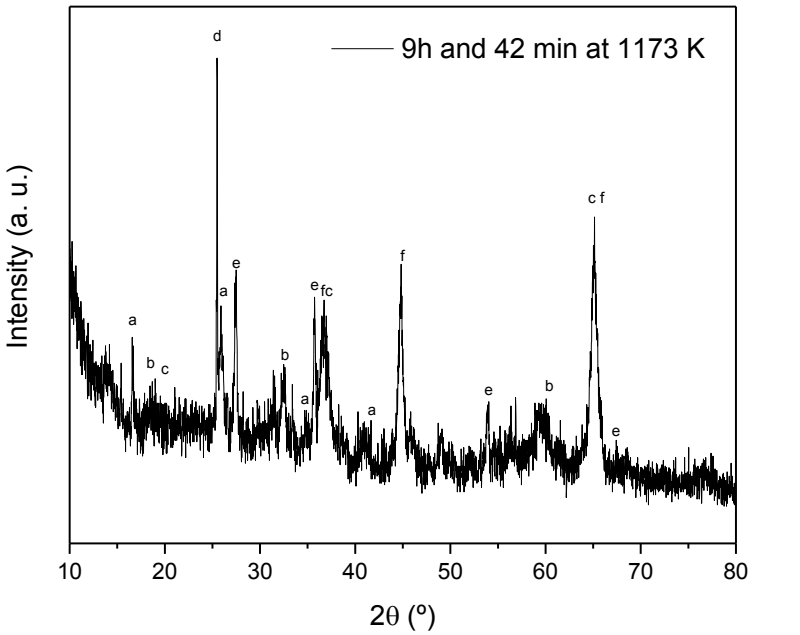

b)

Figure 5.3 XRD patterns of a MAS glass of composition described in[a] table 5.1, nucleated for 48h at 1006 K followed by a) from bottom to the top: 31 min; 61 min and 92 min at 1173 K. b) 9h and 42 min at 1173 K. The presence of corundum peaks is attributed to the sample holder.

Five crystalline phases were identified after the first scan at 1173 K. One of the phases is magnesium spinel, ($MgO.Al_2O_3$ - ICDD PDF2 file 82-2424). This crystalline phase is known to be hard (Hv = 15.4 GPa [73]) and its presence certainly enhances the hardness of the glass-ceramic. Sillimanite ($Al_2O_3.SiO_2$) (ICDD PDF2 file 88-0892), with Hv ~ 11 GPa [74], is also present. A third phase is karooite ($MgO.2TiO_2$ – ICDD PDF2 file 89-6944) whose hardness is unknown. Finally, due to its high concentration in the glass, TiO_2 (Hv = 7-11 GPa [75]) also precipitates.

Because this first scan took 30 minutes to be completed, it was not possible to distinguish which of those four phases came first. To distinguish the order of phase appearance, a faster scan could be used; however, this speed would compromise the already poor intensity of the peaks. It must also be said that, due to the low intensity and high broadness of the peaks, the identification might have been overestimated. Ultimately, Sapphirine ($4MgO.5Al_2O_3.2SiO_2$ – ICDD PDF2 file 11-0607) (Hv = 13.3 GPa [76]) was also identified in the second scan, which started after 31 min at 1173 K. The third scan, which started after 62 min, shows an increase in the intensity of all diffraction peaks, including peaks attributed to sapphirine. Fig. 5.3 b) presents the pattern of the sample after 9 hours and 42 minutes at 1173 K, the intensity of the peaks visibly increased, thus confirming that crystallization was not yet completed. The occurrence of the characteristic diffraction peaks of corundum (Al_2O_3 – IDCC PDF2 file 89-3072) is due to the sample holder.

The role of TiO_2 in the crystallization of cordierite ($2MgO.2Al_2O_3.5SiO_2$) has been extensively discussed. It is classically assumed that TiO_2 induces liquid-liquid phase separation in the volume of MAS glasses [43, 46, 47] that then triggers crystal. The Ti-rich liquid will then crystallize a Ti-containing phase that is used as a substrate to the crystallization of cordierite. However, the hypothesis of liquid-liquid phase separation for the crystallization of cordierite is not the only one proposed. For instance, Guignard, M. et al. has shown, that titania promotes nucleation through the formation of high coordinated Al species and structural fluctuations on the glass that emulates the precipitating crystal phase [77]. The presence of the TiO_2-containig phase ($MgO.2TiO_2$ crystals) in

the first scan may suggest that, in accordance with [43, 46, 47], sapphirine uses these crystals as nucleating sites.

5.1.2 Temperature Dependence Of The Elastic Properties
5.1.2.1 Heating Up To Crystallization Plateau

To observe the evolution of the elastic properties, E, G and ν during heat treatment, a glass sample was submitted to same temperature protocol as used for HTXRD analysis. E and G were then calculated following the method described in section 4.7. An overview of the temperature variation over time is presented in Fig. 5.4, along with the evolution of shear modulus.

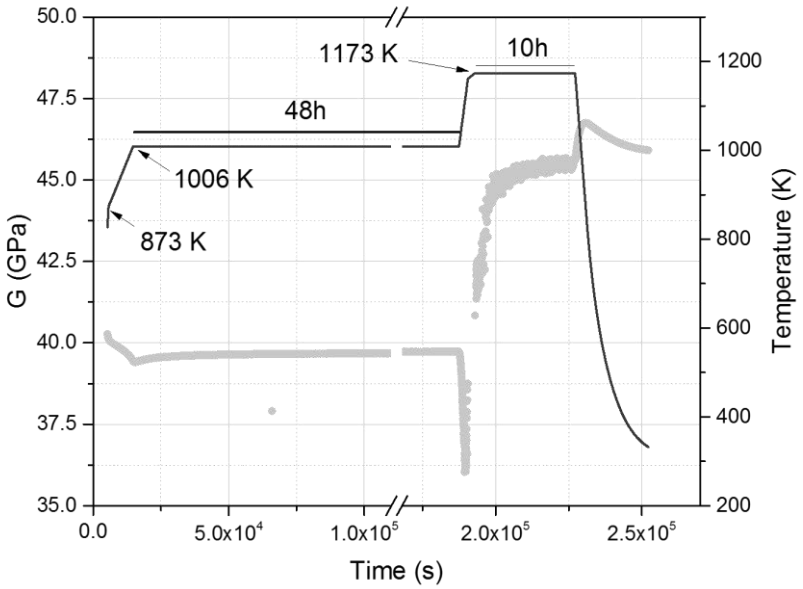

Figure 5.4 Overview of the temperature variation with time used in the *in situ* measurements of mechanical properties and the time-dependence of shear modulus during the whole experiment.

Fig. 5.5 presents the variation of the mechanical properties, E, G and ν, with temperatures up to 1173 K. The experimental points were fitted using different equations. At T < T_{gM}, where T_{gM} is the glass transition temperature deduced from the variation of E(T) or G(T), the temperature dependence of the

elastic moduli is well described by the expression proposed by Wachtman [78] (Eq. 5.1).

$$M = M_{0K} - BTexp\left(\frac{-T_0}{T}\right) \quad (5.1)$$

where M is an elastic modulus (E or G) and M_{0K} is the value when approaching 0 K. The variables B and T_0 are fitting parameters. This expression was used to fit the experimental points between 1007 K and 1035 K, as shown in Fig 5.5.

For temperatures between T = 1045 K and the DSC crystallization temperature, Tx (1173 K), a power law expression (Eq. 5.2) is more suitable [79].

$$\left(\frac{M}{M\ (T_g)}\right) = \left(\frac{T_g}{T}\right)^{\alpha_M} \quad (5.2)$$

where α_M may range from 0.07 for amorphous SiO_2 and 10 for amorphous Se [79] and is related to how fast the liquid softens with temperature. This value is therefore correlated to the fragility index, as described by the concept introduced by Angell [80]. In this expression $M\ (T_g)$ and α_M are obtained by the fitting. For fitting purposes, it was applied T_g = T_{gDSC} (1006 K).

Expressions 5.1 and 5.2 satisfy two fundamental requirements, namely: i) $\frac{dM}{dT}\Big|_{solid}$ approaches zero as T approaches 0 K; and ii) $\frac{dM}{dT}\Big|_{liquid}$ approaches zero as T tends to the maximum temperature sustainable by the melt ($T_{vaporization}$).

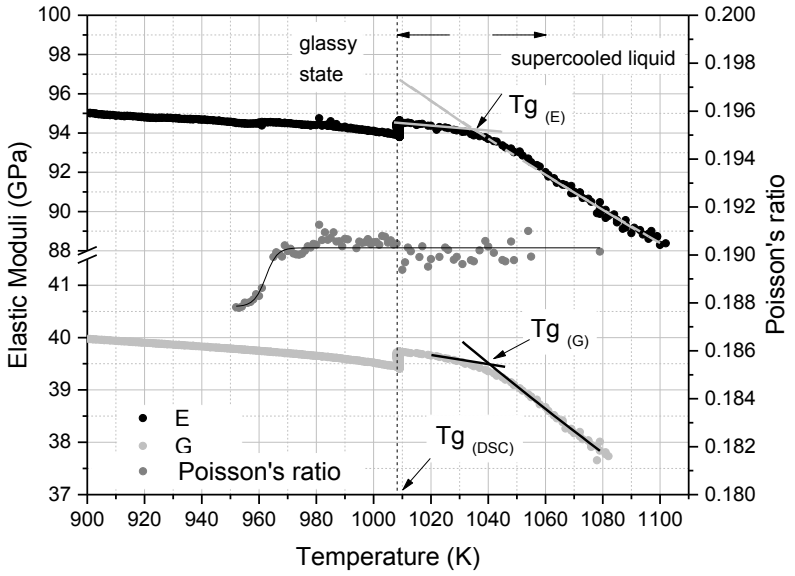

Figure 5.5 The temperature dependence of E, G and ν for two monotonic heating experiments with a plateau at T_{gDSC} between them. Full lines over the experimental points for E and G represent fitting using Eq. 5.1 for T < T_{gM} and Eq. 5.2 for T > T_{gM}. The full line over the calculated Poisson's coefficient is used as a guide.

In Figure 5.5, the glass transition range, T_{gG} and T_{gE}, associated to mechanical resonance is located where the curves corresponding to the glassy and to the liquid states (Eqs. 5.1 and 5.2 respectively) intersect. Note that T_{gG} and T_{gE} were calculated from E(T) and G(T) after a 48 h nucleation plateau. Therefore, without the nucleation plateau, T_{gE} and T_{gG} would be different and may be closer to T_{gDSC}.

Table 5.2 shows the following: glass transition temperature after the nucleation treatment, T_{gE} and T_{gG}, the E, G and ν values at room temperature, the softening rates for E and G immediately below and above Tg (dE/dT^- (T_{gE}), dE/dT^+ (T_{gE}), dG/dT^- (T_{gG}) and dG/dT^+ (T_{gG}), respectively) obtained through the derivation of Eqs. 5.1 and 5.2, and the α_E and α_G values. As a comparison, some typical data for different glasses were added [79, 81-83].

Table 5.2 Elastic properties of the investigated glass and glass-ceramics and glasses of similar compositions.

	E (297 K) (GPa)	G (297 K) (GPa)	ν (297 K)	Tg (E) (K)	Tg (G) (K)	dE/dT$^-$ (T_{gE}) (MPa.K^{-1})	dE/dT$^+$ (T_{gE}) (MPa.K^{-1})	dG/dT$^-$ (T_{gG}) (MPa.K^{-1})	dG/dT$^+$ (T_{gG}) (MPa.K^{-1})	α_E	α_G
This study	98.1	41.3	0.187	1035	1041	-12.5	-94.8	-8	-45	1.04±0.03	1.18±0.02
Alumi. Sil. 1[a)]	-	-	-	933	940	-9.3	-62.6	-4.8	-25.9	0.77±0.01	0.81±0.01
Alumi. Sil. 2[b)]	-	-	-	939	935	-15.7	-52.4	-6.1	-23.5	0.66±0.02	0.73±0.02
Alumi. Sil. 3[c)]	84.0	33.5	0.25	968	960	-11.3	-67.3	-5.3	-29.1	0.83±0.01	0.90±0.01
Alumi. Sil. 4[d)]	87.6	34.8	0.26	1012	1019	-6.7	-53.4	-4.7	-24.7	0.64±0.03	0.78±0.03
Grossular[e)]	92.1	36.0	0.28	1077	1074	-11.3	-73.8	-4.5	-30.5	0.95±0.06	1.00±0.07
Anorthite[f)]	-	-	-	1141	1124	-13.9	-43.2	-3.8	-18.1	0.55±0.01	0.57±0.01
Window Glass	72.0	29.5	0.22	852	855	-28.8	-70.6	-12.6	-29.7	0.93±0.03	0.97±0.03
Diopside[g)]	97.5	38.3	0.27	1218	1276	-32.1	-62.6	-22.7	-14.4	1.00±0.04	1.04±0.02

a) Al/Si = 0.29; b) Al/Si = 0.36; c) Al/Si = 0.35; d) Al/Si =0.5; e) $Ca_3Al_2Si_3O_{12}$; f) $CaAl_2Si_2O_8$and g) $CaMgSi_2O_6$

Although Poisson's ratio (ν) is a coefficient associated with the elastic properties at the macroscopic scale, it has been previously shown [70] to be linked to the atomic network connectivity. The values of ν typically range from 0.1 (for a highly polymerized structure, such as silica glass) to 0.4 (for a weakly polymerized structure containing a high percentage of non-bridging oxygens) [70]. Amorphous silica (a-SiO_2) has a highly cross-linked network (Q^4 structure), and a small value of ν. The presently studied glass has a nominal composition that corresponds to 75 mol% of cordierite ($2MgO.2Al_2O_3.5SiO_2$) and its structure would consist mostly of Q^3 units, which also leads to a cross-linked structure. The studied glass possesses the largest shear modulus value and the third highest Tg value among the glasses in table 3; these findings are consistent with a highly cross-linked structure having a strong atomic binding energy.

However, the studied glass also exhibits the highest softening rate below and above Tg (dG/dT^- (T_{gG}) and dG/dT^+ (T_{gG})) and the largest α_G [84]. This liquid is therefore classified as being relatively fragile. One possible explanation is the composition of the crystalline phases acting as nuclei. As shown in Fig. 5.3 a), Mg-spinel, rutile, karooite and sillimanite are present in the early stages at 1173 K and are presumably the first to nucleate. Because these phases are stable at high temperatures and have a high bonding energy, the residual glassy phase remaining after the crystallization treatment is expected to be less refractory than the parent pristine glass. The residual glassy phase is likely to govern the softening stage and is responsible for the fragile-like character of the liquid. The nuclei act as stiff "islands" (crystalline phases having high values of E and G) that are weakly interconnected by the residual glassy phase [79].

5.1.2.2 Elastic Properties At Nucleation Range

Figure 5.6 presents the evolution of E, G and ν upon the 48 h nucleation treatment at 1006 K.

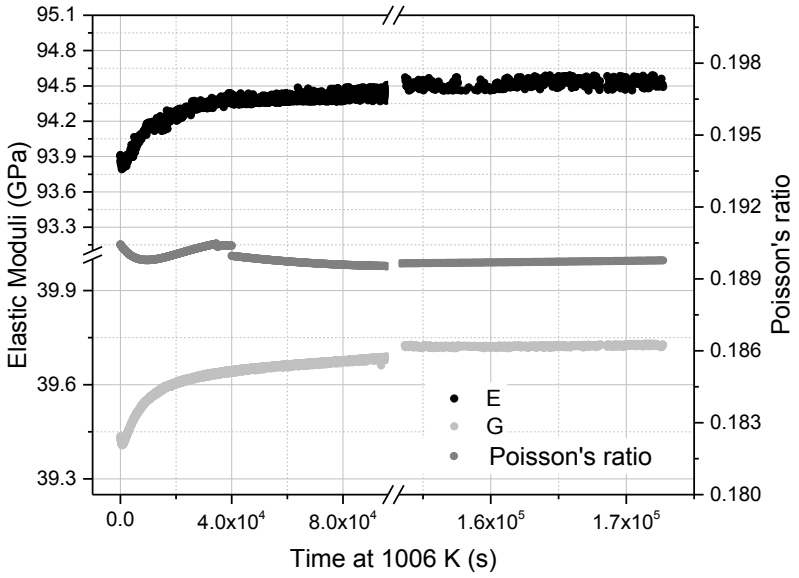

Figure 5.6 Young's Modulus (E), shear modulus (G), and Poisson's ratio as a function of the annealing time at 1006 K for the investigated glass composition.

In the first ten hours of annealing at 1006K, E and G exhibit monotonic and significant increases, which are attributed to some degree of crystallization. For longer times, only a slight evolution is observed (less than a 0.5% increase in E). Nucleation must have a minor effect on the overall atomic connectivity and packing density, thus the effect of the nucleation treatment on ν is very limited (if any). As observed in fig. 5.4, for the initial stage of nucleation, there is a decrease in G. At 1006 K, the glass starts to relax, which promotes a decrease in the mechanical properties. When the crystallized volume fraction increases, it promotes increases in E and G, as indeed observed.

5.1.2.3 Evolution Of The Elastic Moduli Upon Crystallization

Fig. 5.7 a) shows the evolution of E, G and ν upon the crystallization treatment at 1173 K. The evolution of the crystallized volume fraction is described by the Johnson-Mehl-Avrami-Kolmogorov (JMAK) equation [85]. The

experimental data could be smoothly fitted using the rule of mixtures for the effective moduli of the developing glass-ceramic material given by eq. 5.3:

$$M_{GC} = (1 - f(t))M_{RG} + (1 - (exp - Kt^n))M_C \quad (5.3)$$

where M_{GC} is the elastic modulus (E or G) of the glass-ceramic,M_{RG} is the elastic modulus (E or G) of the residual glass, taken at t = 0s at 1173 K, and M_C is the elastic modulus of the crystalline phase. This value promotes the best adjustment to the fitting of the experimental points. The variable K is a constant at any temperature, and n is an integer or half-integer. Table 5.3 summarizes the parameters used to fit the experimental data obtained for E and G and the initial values used for each fit. The errors were estimated using the least squares method. Figure 5.7 b) presents the evolution of Poisson's ratio during the crystallization stage at 1173 K.

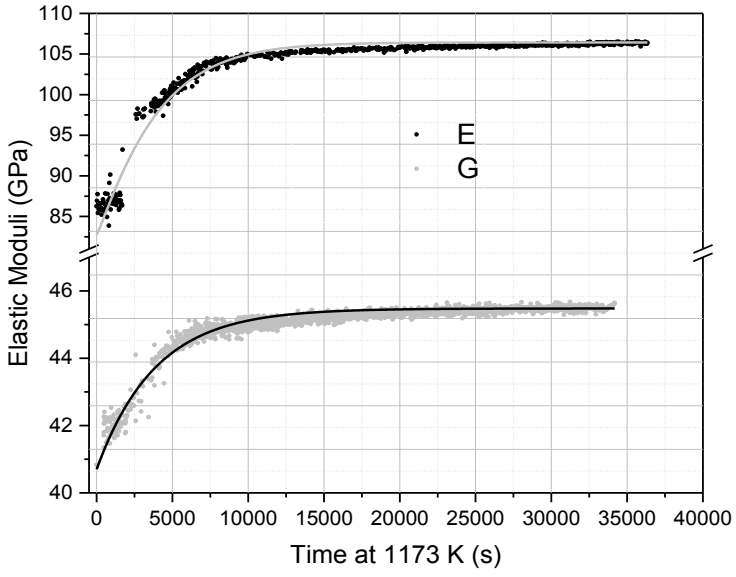

a)

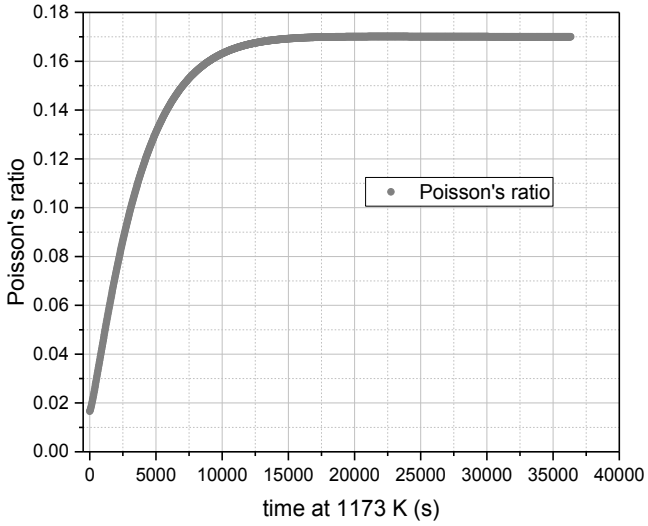

b)

Figure 5.7 a) Experimental points of Young's modulus, shear modulus and the evolution of the crystalline volume fraction, given by the JMAK equation, at the 10-hour crystallization step at 1173 K. b) Poisson's ratio at the 10-hour crystallization step at 1173 K.

Table 5.3 Parameters for the fitting of the experimental points of E and G.

E_{RG} (GPa)	E_C (GPa)	K	n
82.7 ± 0.1	106.4 ± 0.1	$1x10^{-4} \pm 1x10^{-5}$	1.11 ± 0.02
G_{RG} (GPa)	G_C (GPa)	K	n
40.7 ± 0.1	45.5 ± 0.1	$3x10^{-4} \pm 2x10^{-5}$	1.00 ± 0.01

At the beginning of the crystallization process, the volume fraction of the nuclei is extremely low, and hence the volume fraction of the glass matrix is very high. Because the glass has a more open structure compared to the crystal, the Poisson's ratio is low in the early stages at 1173 K and increases as the crystallized fraction increases. As crystallization evolves, the atomic packing density (C_P) increases, leading to an increase in ν [70].

Table 5.3 shows important data for the value of n. The value for crystallization from a fixed number of nuclei can be 1 or 0.5 for needle-like crystal growth, 2 or 1.5 for flat crystals, and 3 or 2.5 for spherical crystals [86]. The values obtained by fitting suggest that the majority of the crystals would exhibit a needle-like shape geometry.

The time-dependent elastic curves (Fig. 5.7) show that mechanical properties increase only slightly between 10,000s (2h and 47min) and 15,000s (4h and 10min) of crystallization treatment. This increase suggests that there is only a small change in the crystallized volume fraction over this time interval. However, the change is detected by a continuous increase in Poisson's ratio, which becomes constant only after 15,000s. The slow evolution of the composition and the network structure of the residual glassy phase over the next 3h were reflected by the increase in ν up to 15,000s.

5.1.3 Hardness And Indentation Fracture Toughness

5.1.3.1 Glass

Figure 5.8 Vickers indent performed at load of a) 600 mN; b) 1 N; c) 4.9 N; d) 9.8 N; e) 49.03 N; f) 98.07 N and g) 196.1 N.

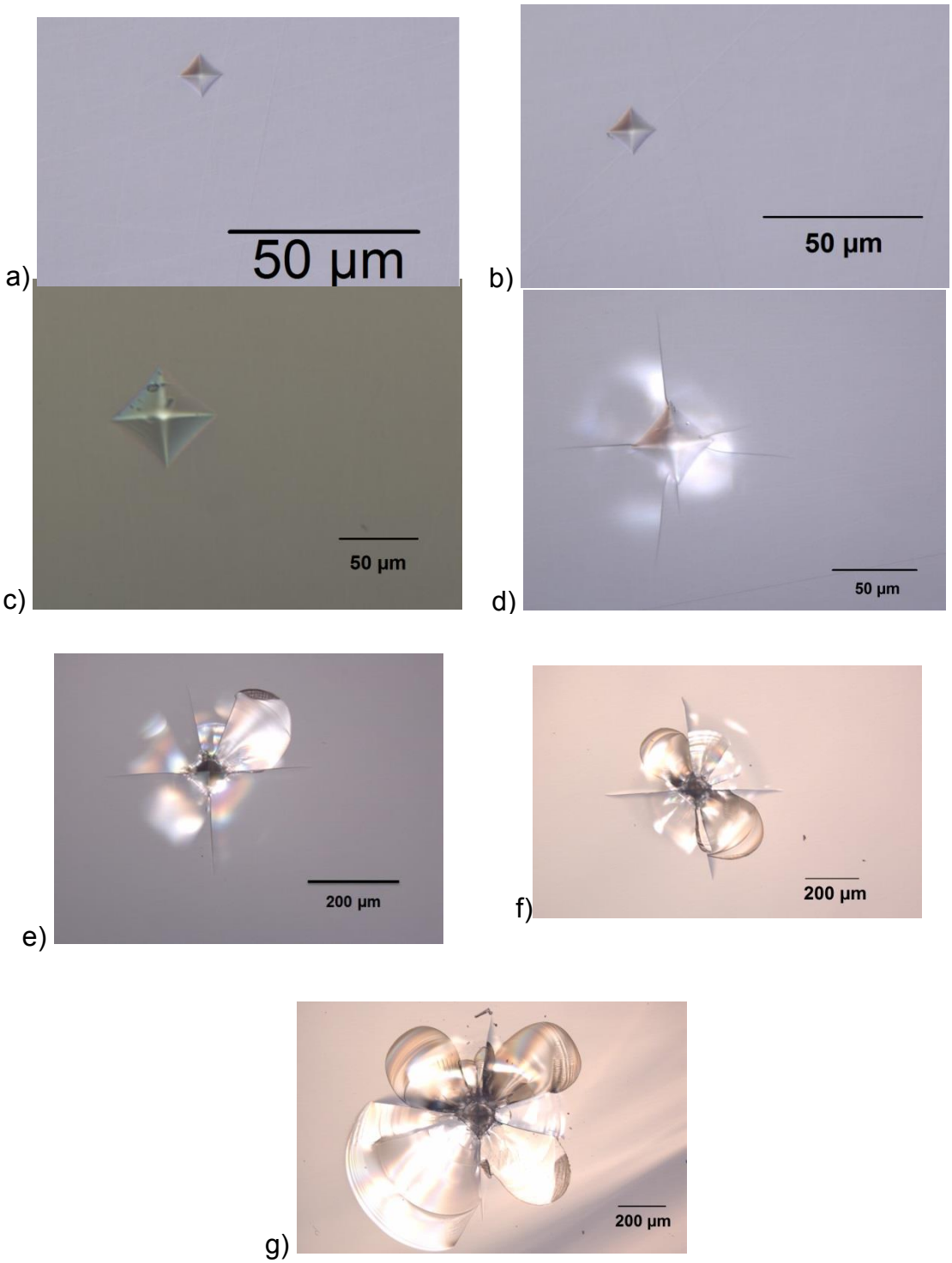

Figure 5.8 Vickers indent performed at load of a) 600 mN; b) 1 N; c) 4.9 N; d) 9.8 N; e) 49.03 N; f) 98.07 N and g) 196.1 N

With the increasing loads, the size of the imprints and the damage on the samples also increase. Up to the load of 4.9 N, no cracks were visually

observed. With the application of 9.8 N, median cracks were seen, and lateral cracks also appear for higher loads. Table 5.4 presents the mean hardness value of the samples.

Table 5.4 Applied loads, mean half diagonal of Vickers imprint, mean crack length and mean hardness.

Load (N)	**a (μm)**	**c (μm)**	**c/a**	**Hv (GPa)**
0.60	5.88 ± 0.05	non observed	-	8.7 ± 0.4
1.00	7.62 ± 0.05	n. o.	-	8.5 ± 0.3
4.90	17.26 ± 0.01	n. o.	-	8.22 ± 0.04
9.80	24.16 ± 0.01	95.88 ± 0.01	3.84 ± 0.02	7.9 ± 0.2
49.03	52.88 ± 0.01	284.12 ± 0.02	5.28 ± 0.02	8.5 ± 0.8
98.07	66.42 ± 0.01	339.04 ± 0.02	5.88 ± 0.02	11 ± 2
196.1	93.02 ± 0.01	529.14 ± 0.02	5.69 ± 0.02	11 ± 1

It is possible to see that this glass presents, for loads lower than 10 N, the load-dependency of hardness known as the indentation size effect (ISE). This behavior at low-applied loads was observed for other glasses like borosilicate, aluminosilicate, soda lime silicate and fused silica [87]. Hardness presents a tendency to decrease with increasing applied load, from 600 mN to 9.80 N. Then, for the applied load of 49.03 N, a slight increase is observed, but the value is within the error for the smaller loads. A change in behavior is observed when a load of 98.07 N is applied. Hardness increases significantly, presenting its highest mean value. This must be explained by the fact that most of the energy of the indentation process was not used to perform the imprint, but to create cracks around the imprint. The smaller size of the imprints leads to a

higher mean hardness value. Figure 5.9 presents a graph showing how hardness changes with the applied load.

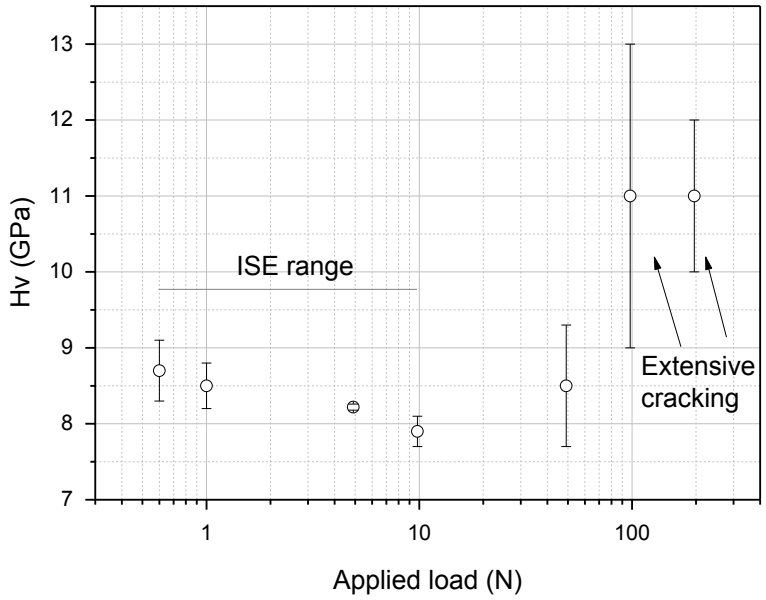

Figure 5.9 Change in hardness values with the applied load for a glass sample.

5.1.3.2 Glass-Ceramics

Observing the evolution of the mechanical properties with temperature presented at 5.1.2.2, it was decided to crystallize 4 different samples and observe the changes on Hv at different crystallization stages. The four crystallized samples had the same nucleation treatment (48h at 1006 K) and different growth times at 1173 K. The chosen growth times were: 31 minutes, 61 minutes, 92 minutes and 153 minutes. This heat treatment was performed to have samples with the same nuclei density, but with different crystal size. These times of treatments at 1173 K were chosen because they show different moments of the evolution of elastic moduli and Poisson's ratio, as it can be observed in Figs. 5.7 and 5.8. Hardness and IFT increase of the glass ceramic samples were measured using the following loads: 4.9 N; 9.8 N; 49.03 N; 98.07 N; 196.1 N. Table 5.5 presents hardness values of the glass-ceramics. Figure 5.10 presents the profile of the indents in each sample, for each load.

Table 5.5 Applied loads, mean values of half diagonal of Vickers imprint (a), crack length (c), hardness (H) and Indentation Fracture Toughness increase (IFT).

Sample	Load (N)	a (μm)	c (μm)	c/a	Hv (GPa)	IFT increase (%)
48h at 1006 K + 31 min at 1173 K	4.9	17.59	53.56	3.38	7.95 ± 0.05	---**
	9.8	25.23	86.61	3.46	7.7 ± 0.1	8 ± 10
	49.03	53.11	238.01	4.47	8.7 ± 0.1	15 ± 4
	98.07	71.69	366.80	5.00	9.6 ± 0.6	10 ± 7
	196.1	44.24	469.03	5.33	12 ± 2	10 ± 10
48h at 1006 K + 61 min at 1173 K	4.9	16.10	50.76	3.16	9.5 ± 0.3	---**
	9.8	22.9	78.19	3.42	9.35 ± 0.08	24 ± 10
	49.03	51.99	223.32	4.28	9.06 ± 0.05	38 ± 4
	98.07	71.96	356.15	4.94	9.4 ± 0.1	20 ± 7
	196.1	94.77	504.07	5.32	11.0 ± 0.6	10 ± 10
48h at 1006 K + 92 min at 1173 K	4.9	15.95	50.54	3.17	10 ± 1	---**
	9.8	22.97	78.67	3.42	9.3 ± 0.3	24 ± 10
	49.03	51.61	223.23	4.33	9.2 ± 0.2	38 ± 4
	98.07	66.02	323.71	4.91	12 ± 1	30 ± 10
	196.1	---*	---*	---*	---*	---*
48h at	4.9	15.57	48.85	3.14	9.9 ± 0.5	---**

1006 K + 153 min at 1173 K	9.8	22.63	77.24	3.41	9.7 ± 0.3	27 ± 10
	49.03	51.56	227.78	4.38	9.1 ± 0.4	38 ± 6
	98.07	70.05	343.03	4.92	10.0 ± 0.2	27 ± 6
	196.1	---*	---*	---*	---*	---*

*severe damage made it not possible to measure the imprinted diagonals.

** Due to the absence of cracks on the glass for this load, IFT increase was not calculated.

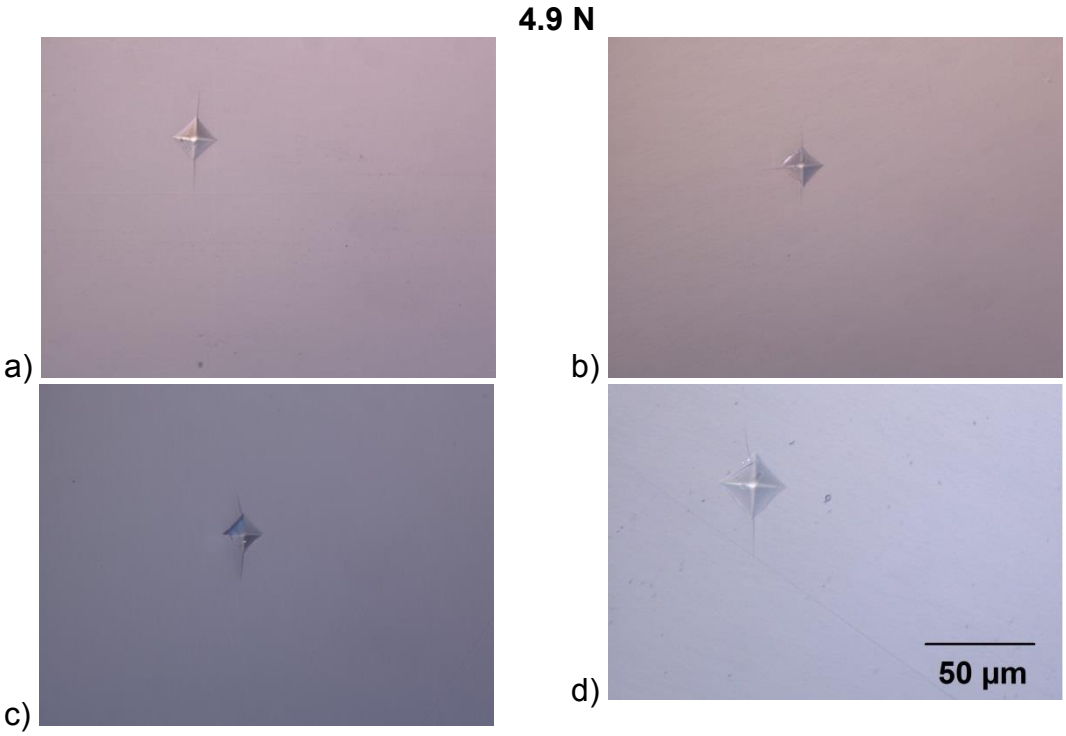

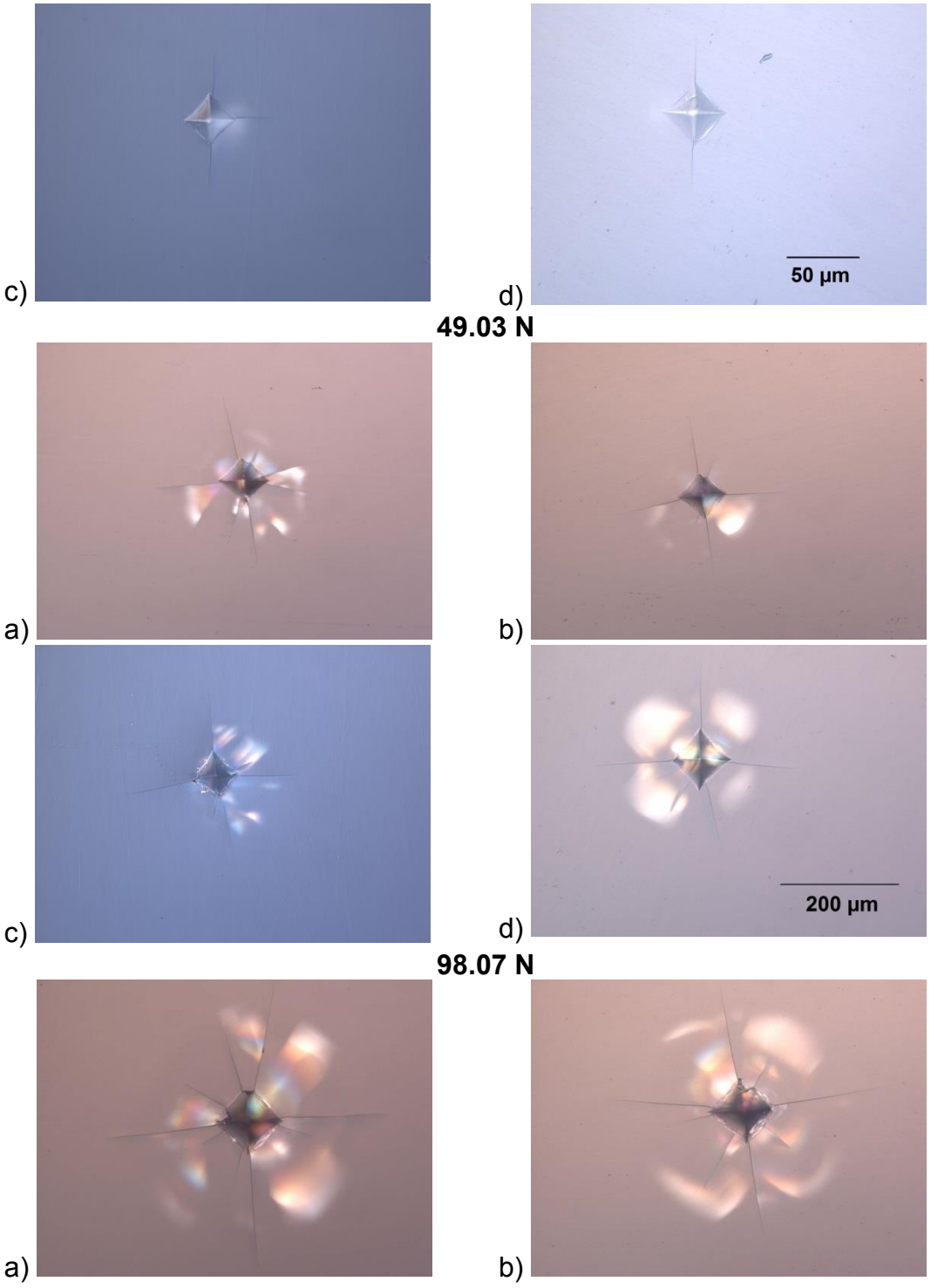
c)
d)
50 µm
49.03 N
a)
b)
c)
d)
200 µm
98.07 N
a)
b)

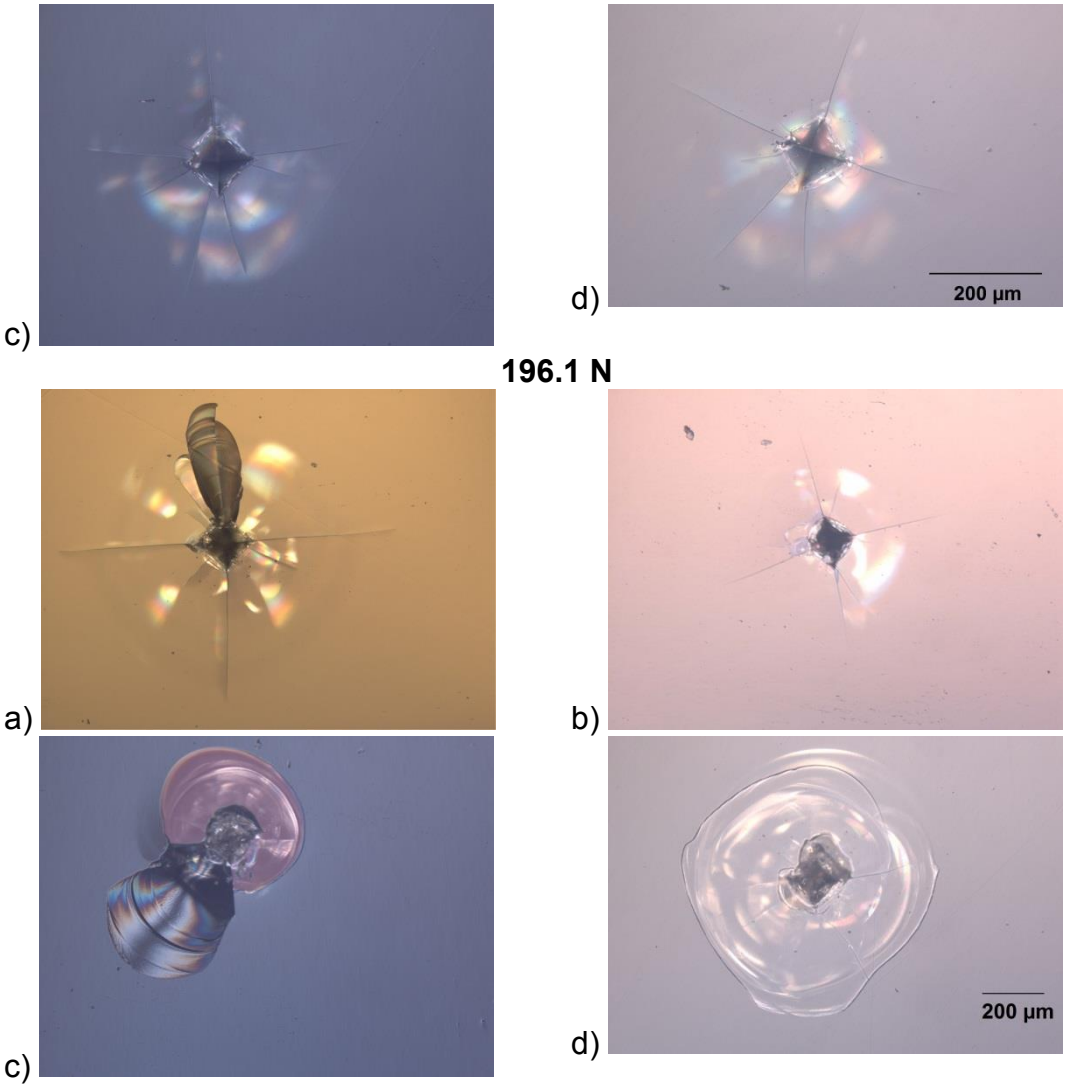

Figure 5.10 Profile of the indents for each load. a) 48h at 1006 K + 31 min at 1173 K; b) 48h at 1006 K + 61 min at 1173 K; c) 48h at 1006 K + 92 min at 1173 K and d) 48h at 1006 K + 153 min at 1173 K. Scale is the same for the pictures of each load.

Comparing the imprint profile of the glass and the glass-ceramic (fig. 5.8 and fig. 5.10, respectively) it can be seen that crack and damage resistance increases. For the same applied load, one sees a larger imprint on the glass surface than on the glass-ceramic surface. With crystallization, all glass-ceramics behave similarly when it comes to the generation of radial and lateral cracks. The exception is for the highest load.

ISE behavior of the glass-ceramics is not the same for all samples. Glass-ceramic sample heat-treated for 48h at 1006 K and 31 min at 1173 K has an

ISE behavior close to the one of the glass, with decreasing hardness while load is increased until 9.8 N, then higher hardness for higher loads. The lower crystalline fraction of this particular sample would explain this behavior closer to the glass than to the other glass-ceramics. The same way it was observed for the glass, extensive cracking also occurs for hardness tests of applying load of 98.07 N and higher. This explains the scattered values obtained and the apparent higher measured hardness, as shown in Table 5.5 and seen on Fig. 5.11 b).

Glass-ceramic crystallized for 48h at 1006 K and 61 min at 1173 K presented a discrete drop in Hv with increasing applying load from 4.9 N to 49.03 N. This sample was the one with the smallest increment in Hv when the applying load increased from 49.03 N to 98.07 N.

Glass-ceramic crystallized for 48h at 1006 K and 92 min at 1173 K showed a slight decrease in Hv with increasing load from 4.9 N to 9.8 N, and then it remained constant to the applying load of 49.03 N. This sample is the one that presented the largest increase for the applying load of 98.07 N. For the sample with the highest crystalline fraction, the one after 48h at 1006 K and 153 min at 1173 K, hardness values shrink for increasing loads until 49.03 N, then increase again for 98.07 N.

The difference in the crystalline fraction and the phases present in each sample might explain the different behavior of Hv with the applying load. For all samples, the increase of Hv for the applying load of 98.07 N when compared to 49.03 N might occur for the same reason as for the glass: great part of the energy of the indentation process was used to create cracks around the imprint, leading to smaller imprints, thus, to higher Hv values. Fig. 5.11 presents the ISE for the glass-ceramics.

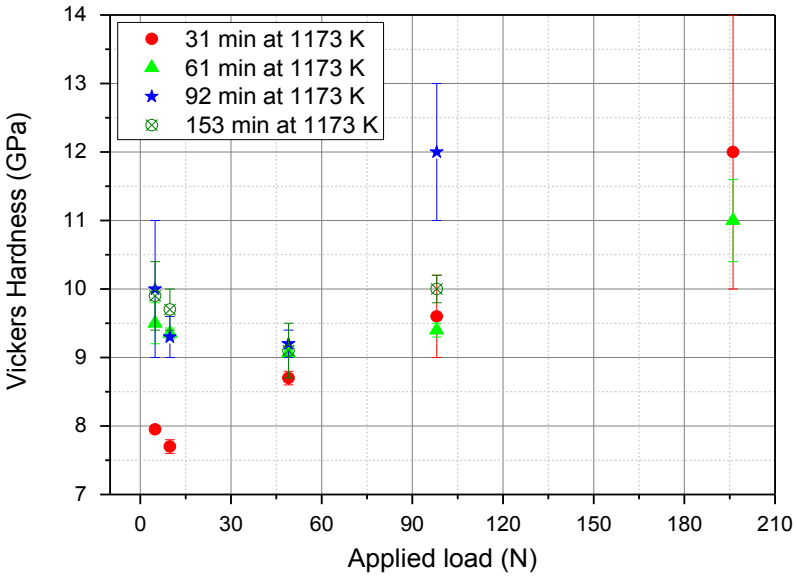

a)

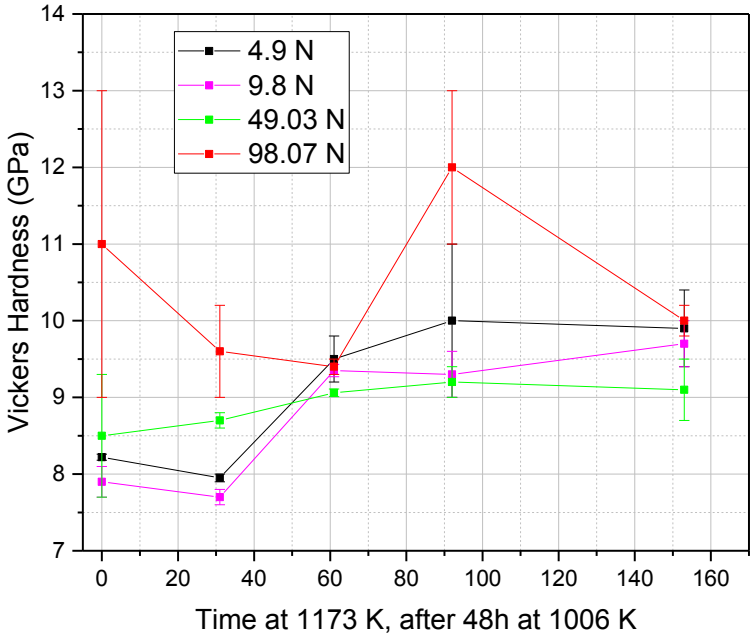

b)

Figure 5.11 a) Change in hardness values with the applied load for the glass-ceramic samples and b) Change in hardness values with time at 1173 K, after 48h at 1006 K, for different applied loads.

Each of these glass-ceramic samples represent different crystallization stages, with increasing values Young's modulus and shear modulus as the

crystallization time at 1173 K increases. It would be expected that the sample's hardness followed the same trend, i. e. increasing values for increasing time at 1173 K, which leads to an increase in the crystal volume fraction. However, this was not observed. It can be concluded that hardness is macroscopically less sensitive to crystallized volume fraction changes than E and G

5.1.4 K_{IC} Measurements

The glass and glass-ceramics had their fracture toughness measured as described in 3.4.1. Figure 5.12 presents a sample after the generation of the pre-crack, following the scheme presented in fig. 3.10. The brighter part under the sample is the 3.4 mm groove at the anvil. Sample was tilted to get a better picture of the pre-crack. Figure 5.13 presents the fracture region of a sample after the 3-point bending test. Precrack (bottom) was clearly distinguished from the fast-propagating crack region. The imprints and the cracks generated by them are seen in the bottom of the sample. The precrack size, the maximum fracture load, the support span for the 3-point bending test, the specimen thickness and the specimen width are used in eq. 3.5 to calculate the samples' toughness. The values of K_{IC} are presented in fig. 5.14. For the sake of comparison, IFT calculated using Niihara and Anstis equations are added. It can be seen that all the glass-ceramics have the same fracture toughness within the error, and the glass has the lowest K_{IC}, as expected.

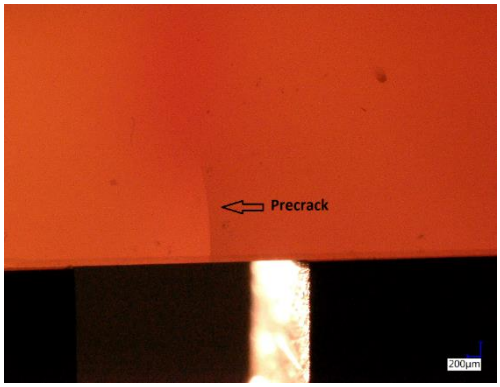

Figure 5.12 Sample with generated precrack.

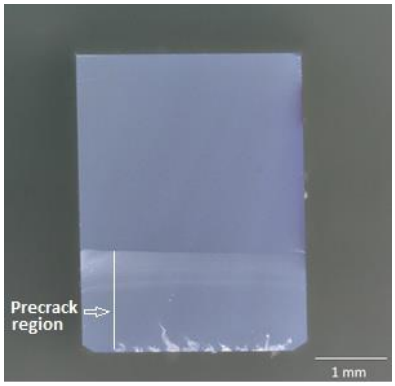

Figure 5.13 Fracture surface of sample after 3-point bending test. The pre-crack region is clearly distinguished from the fast propagating region. Heat treatment of 48 h at 1006 K and 153 min at 1173 K.

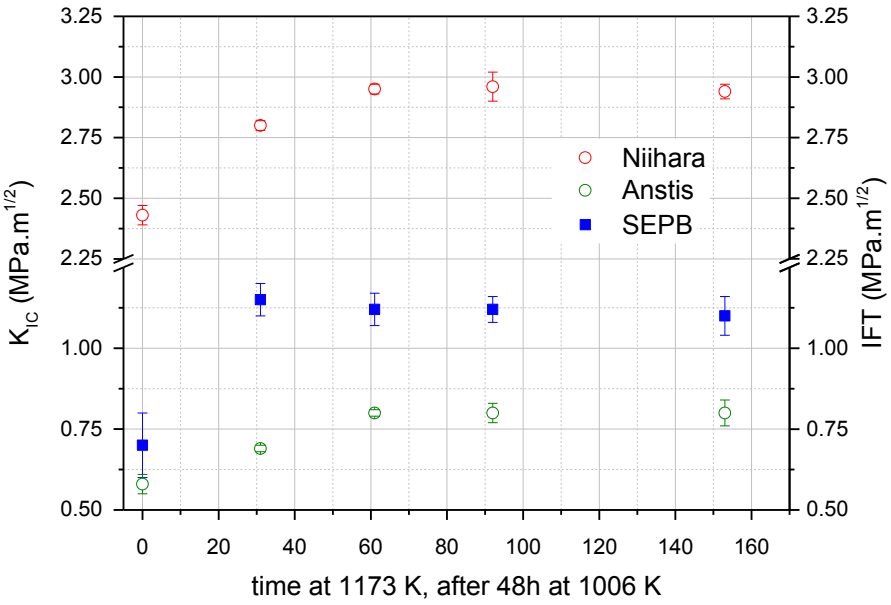

Figure 5.14 Toughness measurements for the glass and glass-ceramics obtained with different growth periods at 1173 K.

It can be seen that all the glass-ceramics have the same fracture toughness within the error, and the glass has the lowest K_{IC}. The results also show that there is no correlation between values of indentation toughness and

those obtained from SEPB method. After the standardized technique, the glass-ceramic with a heat treatment of 48 h at 1006 K and 31 min at 1173 K presented the highest value of K_{IC}, although after indentation toughness, that heat treatment leads to the smallest value of K_{IC}. The validity of K_{IC} measurements performed via indentation is widely and long questioned [61].

5.1.5 Microstructure Analysis

After the heat treatment of 48h at 1006 K and different times at 1173 K, the microstructure of the glass-ceramic powder samples was analyzed with transmission electron microscopy, due to the nanometric scale of the crystals. The microstructure of each sample is presented below.

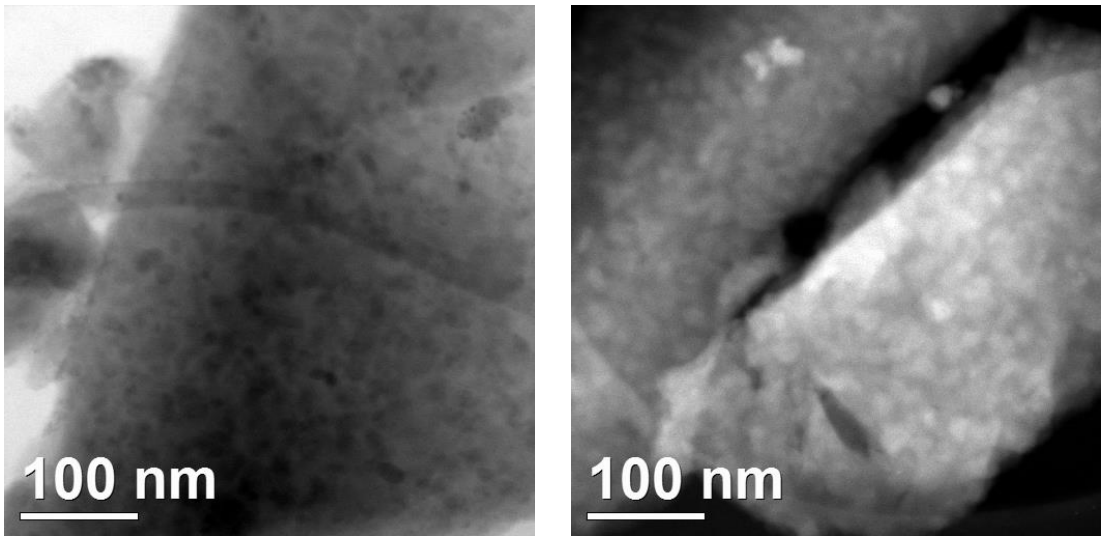

a) b)

Figure 5.15 Transmission electron microscopy analysis of a sample from formulation 75-25 after nucleation treatment at 48h at 1006 K and 31 min at 1173 K a) bright field and b) dark-field images.

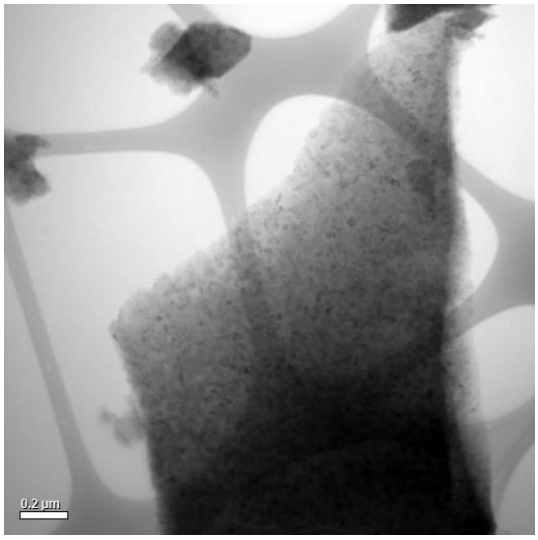

a)

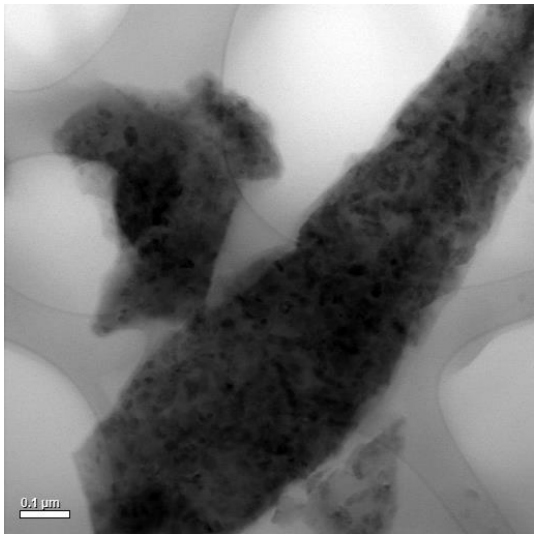

b)

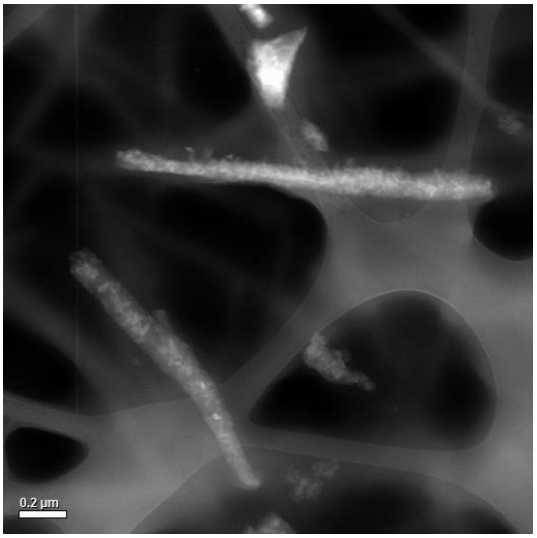

c)

Figure 5.16 Transmission electron microscopy analysis of a sample from formulation 75-25 after nucleation treatment at 48h at 1006 K and 61 min at 1173 K. Bright field (a) and b)) and dark-field (c)) images.

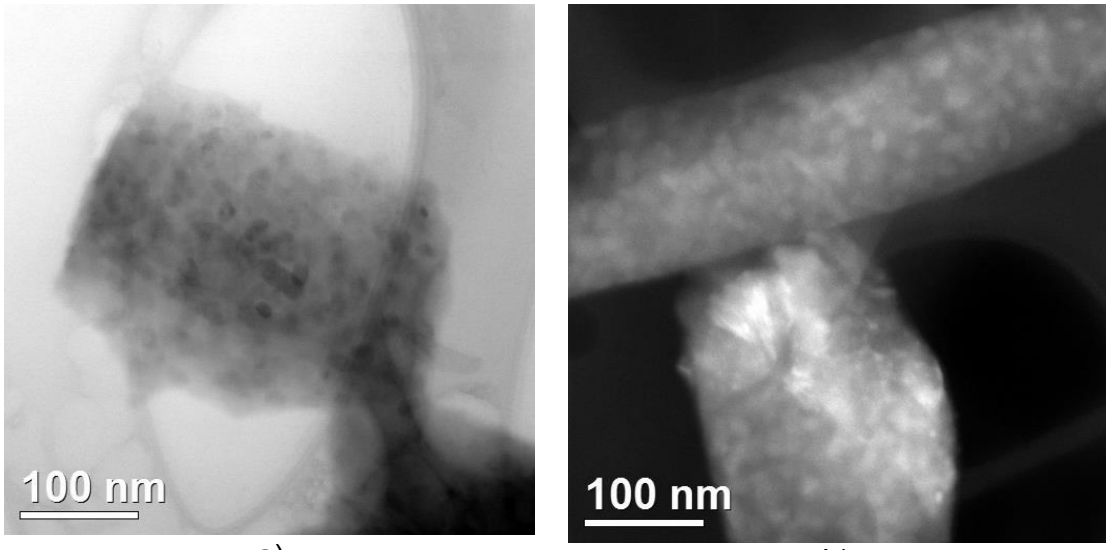

a) b)

Figure 5.17 Transmission electron microscopy analysis of a sample from formulation 75-25 after nucleation treatment at 48h at 1006 K and 92 min at 1173 K a) bright field and b) dark-field images.

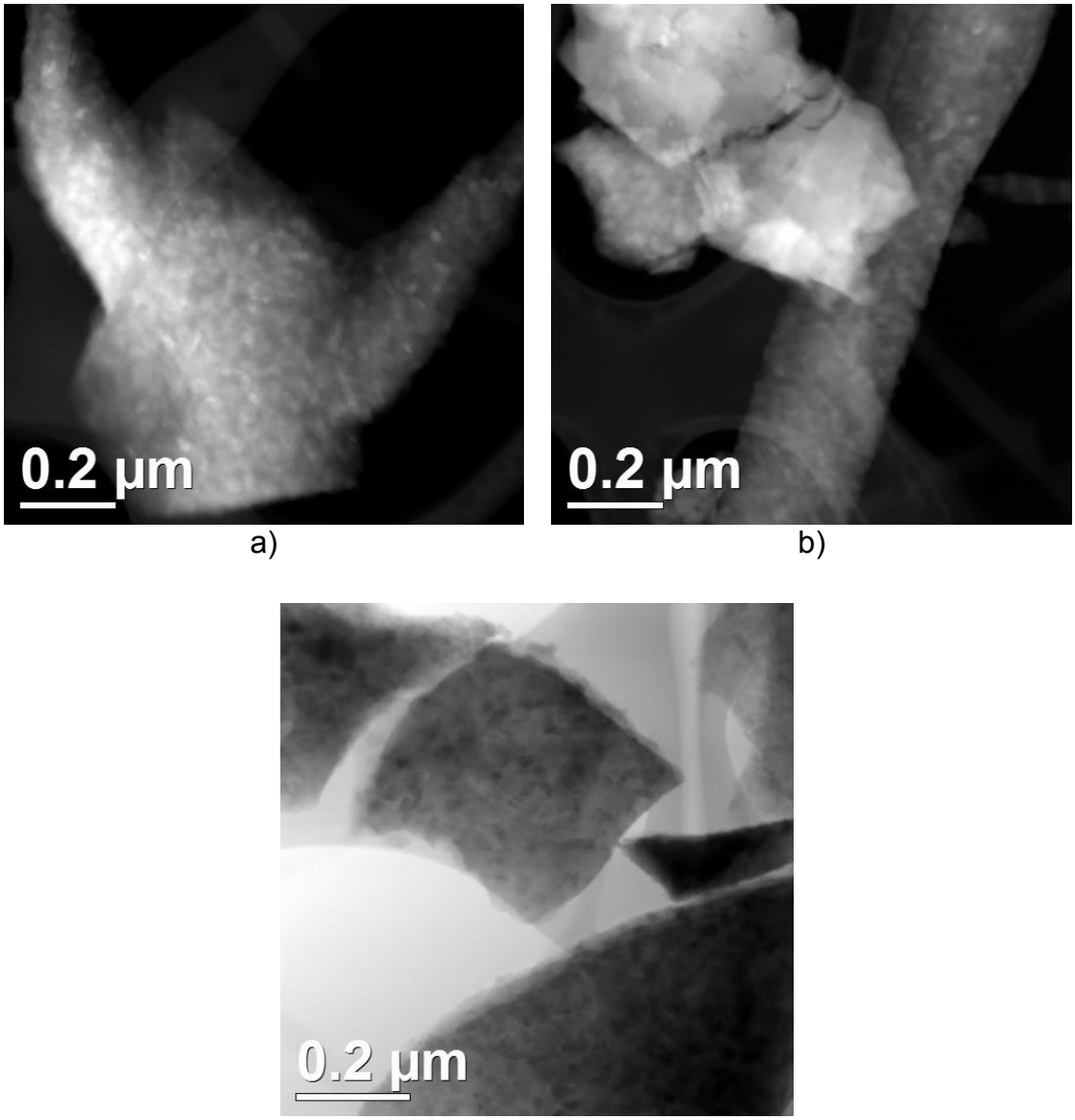

a) b)

c)

Figure 5.18 Transmission electron microscopy analysis of a sample from formulation 75-25 after nucleation treatment at 48h at 1006 K and 153 min at 1173 K. Bright field (a)) and dark-field (b) and c)) images.

Each sample presents bright and dark field images of the microstructure. It can be seen on the images that samples have been highly crystallized since the early stages of the treatments. The amount of the residual glassy phase decreases with time at 1173 K, as expected. However, residual glass still remains after 48h at 1006 K and 153 min at 1173 K, as it can be seen in Fig.

5.18 b). This presence of the residual glassy phase corroborates with the measurements of E and G with temperature, presented in Fig. 5.7. The slow increase on these properties shows that the residual glassy phase is still there and changing with time at 1173 K.

Although the glassy phase shrinks with time, shape and size of the crystals do not change much. The similarity of the structures would explain the close values of hardness (at higher loads) and K_{IC}. It is not possible to distinguish each crystalline phase among the observed crystals, which are 20-50 nm large in average. An element mapping was also performed using energy dispersive x-ray detector (EDS) at the TEM analysis. The results are shown below.

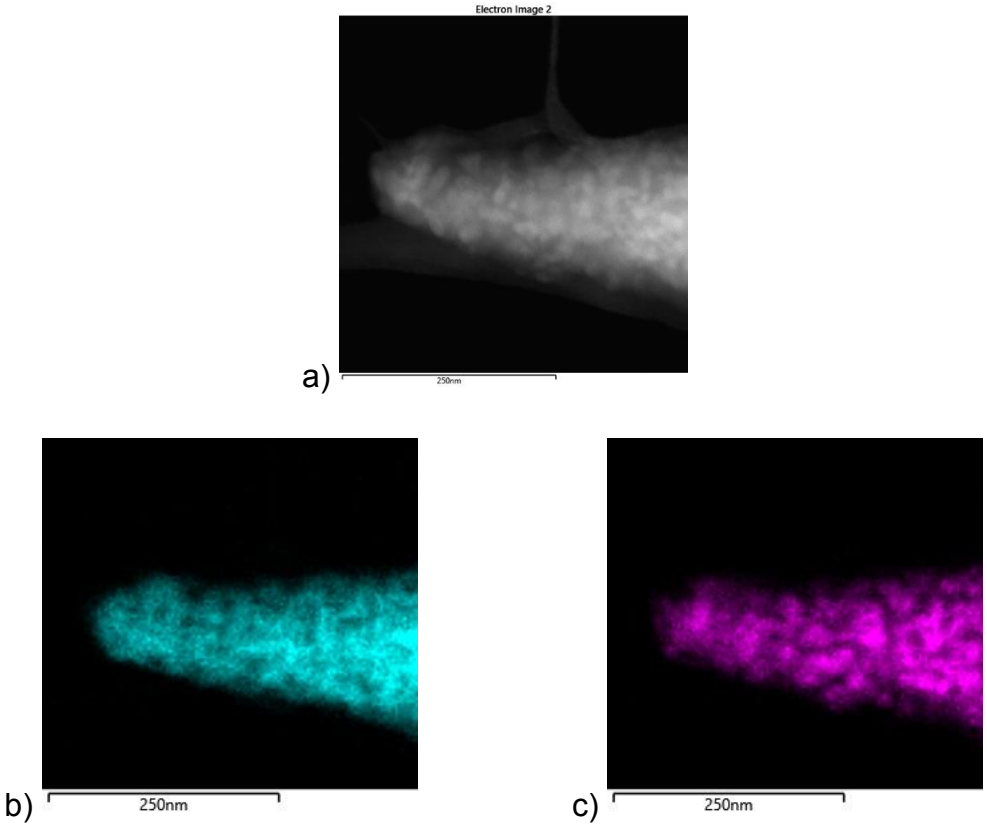

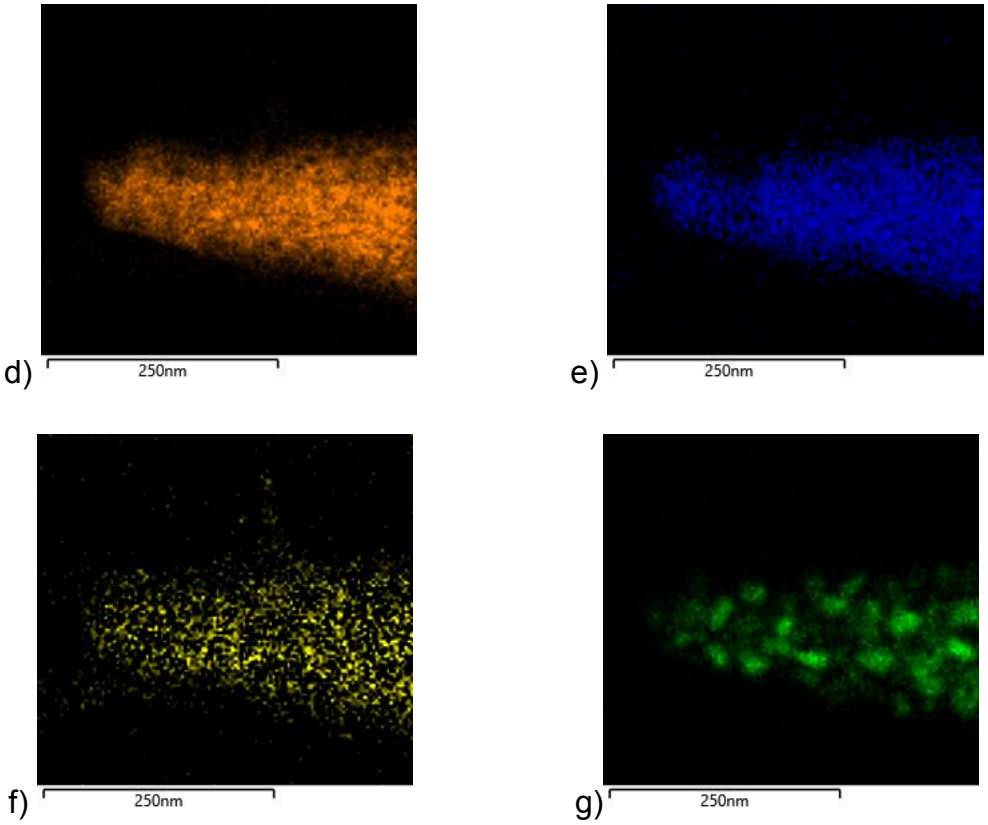

Figure 5.19 Element dispersion on the glass-ceramic particle from formulation 75-25 after nucleation treatment at 48h at 1006 K and 31 min at 1173 K. EDS images. a) original image; b) Si; c) Al; d) Mg; e) Sb; f) Zr and g) Ti.

The EDS measurement shows that Mg and Sb are the least densely concentrated elements on the analyzed area, being uniformly present either in the crystal phase and the residual glass. No crystal phase containing Sb was detected via X-Ray, as it can be seen on fig. 5.3, so this result is not a surprise. Magnesium, nonetheless, was expected to be more densely concentrated that it is, since it is present on 2 out of 4 crystal phases present at this time and temperature. The low concentration may be a reflex of the initial stages of crystallization, where the crystal phases are identified via XRD but they are in a low volume fraction. Si and Al are much more densely concentrated. The first is present only in one out of the four crystal phases present. This would suggest that this phase is in a higher concentration comparing to the others. The fact that Al is densely concentrated and present in two phases, one with Si and another with Mg, is an indicative that the phase containing Sillimanite

($Al_2O_3.SiO_2$) is in higher concentration and the Mg-spinel, in a lower concentration. Zr is less densely concentrated and is not present on any crystal phase. Ti is highly densely concentrated and present on two out of the four crystal phases present at this time and temperature. One of the phases is pure TiO_2 and the other is a magnesium titanate. Again, since Mg is less densely concentrated, Ti might be highly densely concentrated on the form of pure TiO_2.

Fig. 5.20 presents the EDS spectra for the sample after 48h at 1006 K and 61 min at 1173 K.

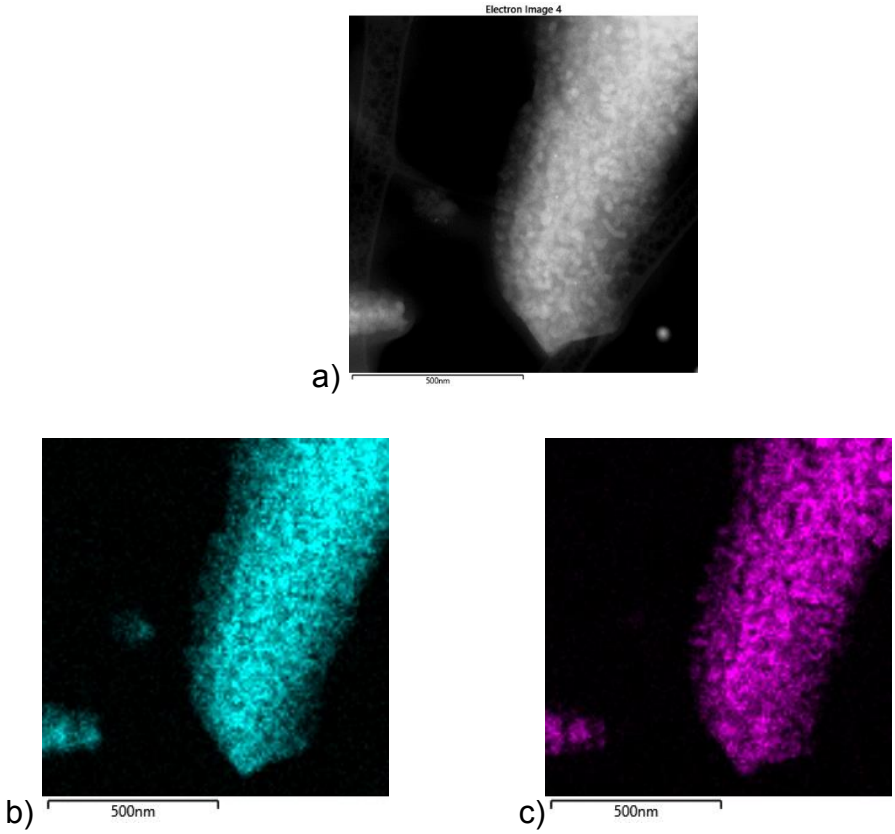

a)

b)

c)

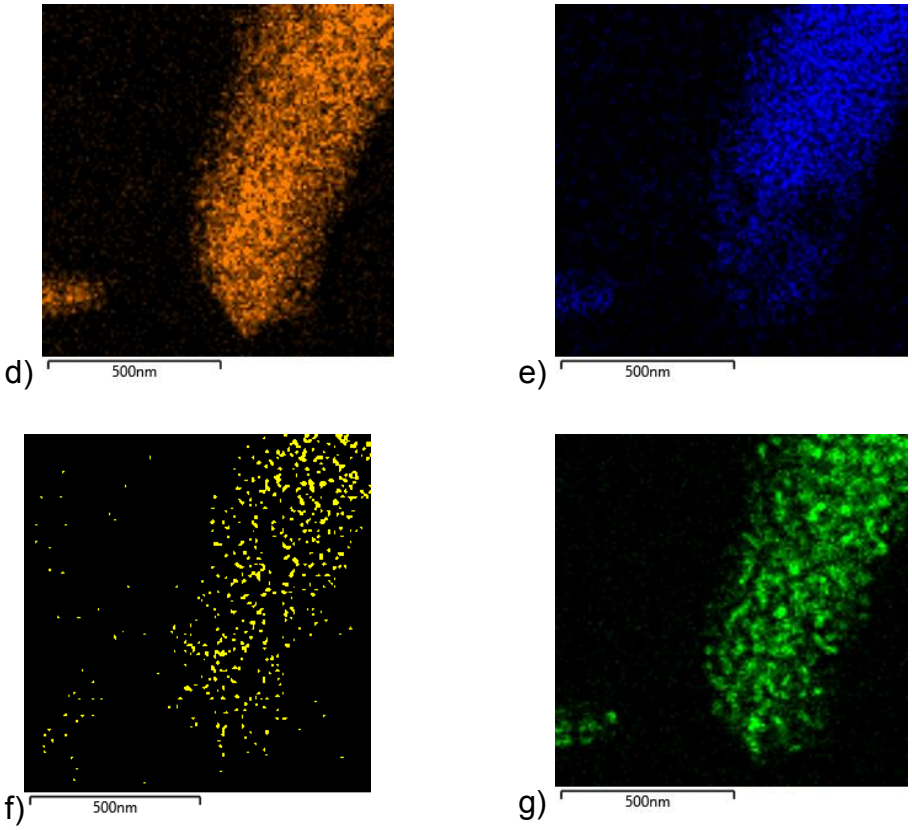

Figure 5.20 Element dispersion on the glass-ceramic particle from formulation 75-25 after nucleation treatment at 48h at 1006 K and 61 min at 1173 K. EDS images. a) original image; b) Si; c) Al; d) Mg; e) Sb; f) Zr and g) Ti.

All the elements are more concentrated now than they were in the previous analyzed sample, as expected. Mg now is present in 3 out of the 5 crystal phases detected at this time and temperature. The presence of Sapphirine ($4MgO.5Al_2O_3.2SiO_2$), combined with the increase in volume fraction of the other crystal phases, helps understand the higher concentration of Mg when compared to the previous sample.

Fig. 5.21 presents the EDS spectra for the sample after 48h at 1006 K and 92 min at 1173 K.

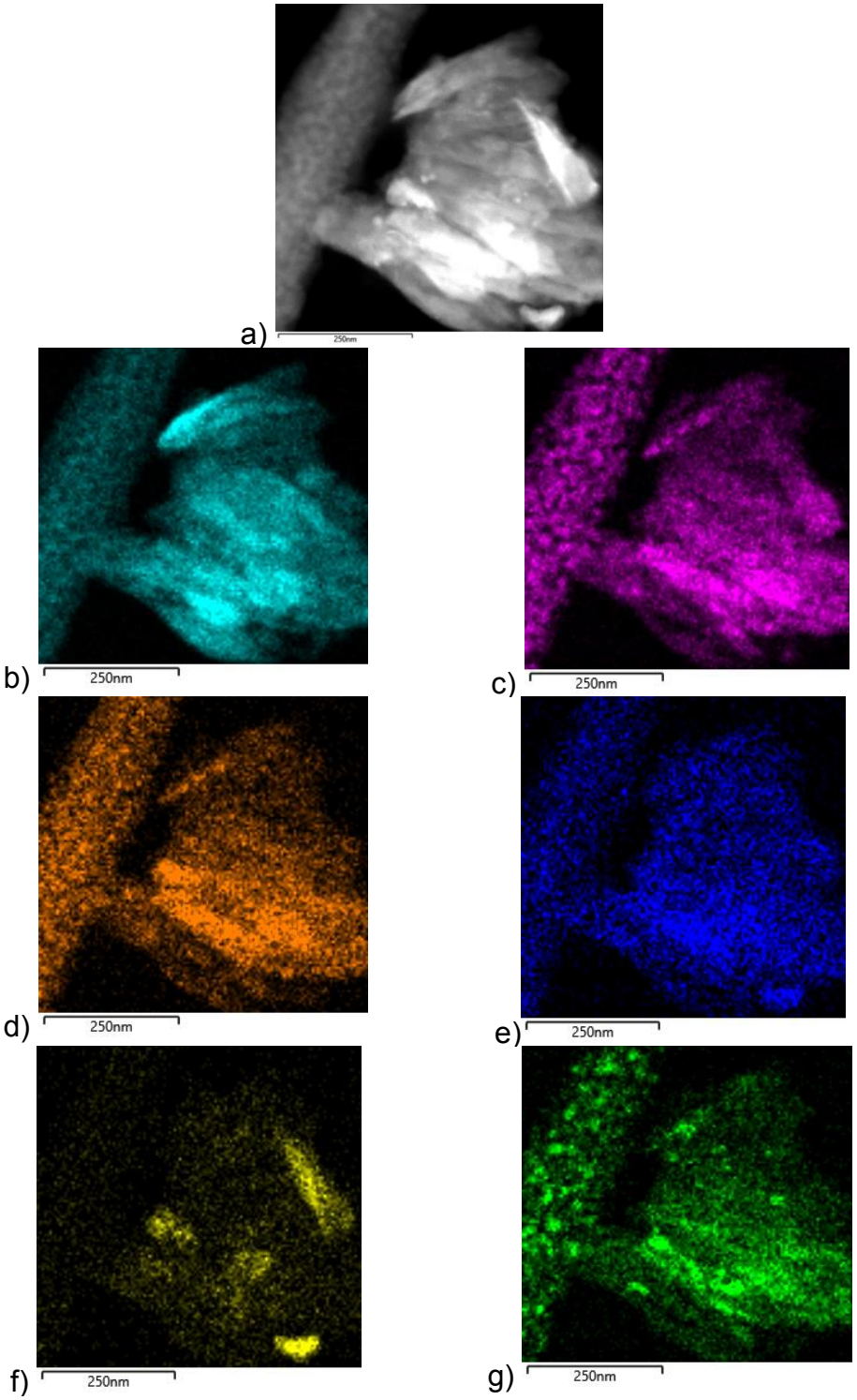

Figure 5.21 Element dispersion on the glass-ceramic particle from formulation 75-25 after nucleation treatment at 48h at 1006 K and 92 min at 1173 K. EDS images. a) original image; b) Si; c) Al; d) Mg; e) Sb; f) Zr and g) Ti.

The EDS analysis of this sample showed that all the elements but Sb are observed in regions with gradient concentration. Nevertheless, Sb is uniformly distributed through all the analyzed region. Two important facts must be commented on. Firstly, Zr, that was not detected in any crystal phase even after the crystallization cycle of 48h at 1006 K and 12h at 1173 K applied at the HTXRD, is present in four highly concentrated zones. Secondly, the high concentration zones of Ti and Mg are equivalent, leading to the conclusion that the amount of $MgO.2TiO_2$ increases. This crystal phase may be used by sapphirine as a substrate to its nucleation.

Fig. 5.22 presents the EDS spectra for the sample after 48h at 1006 K and 92 min at 1173 K.

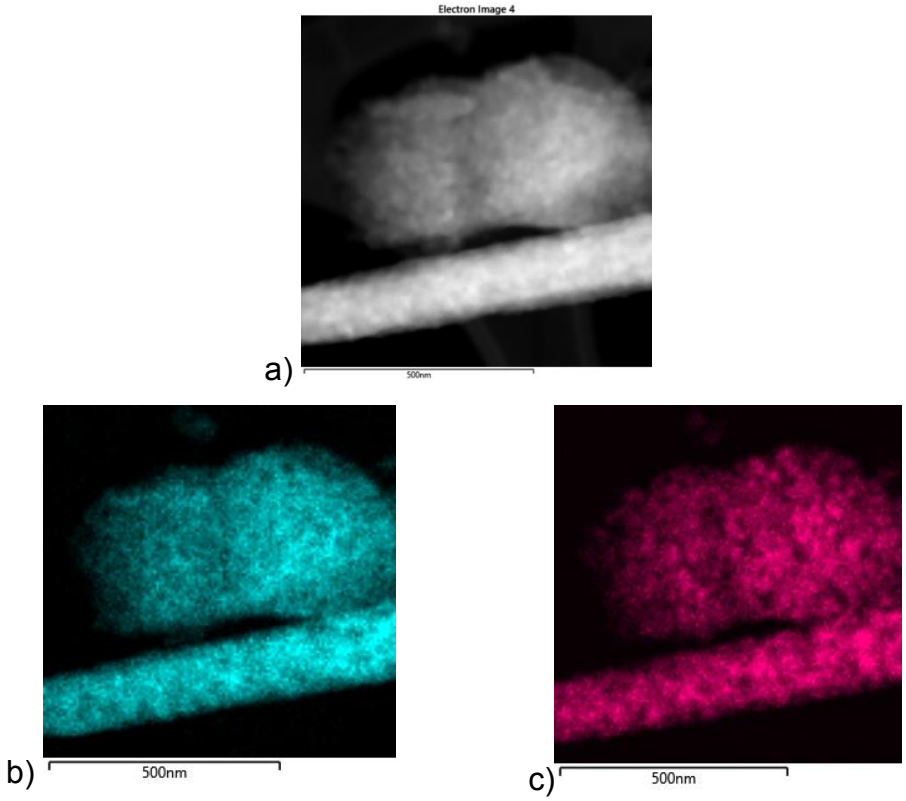

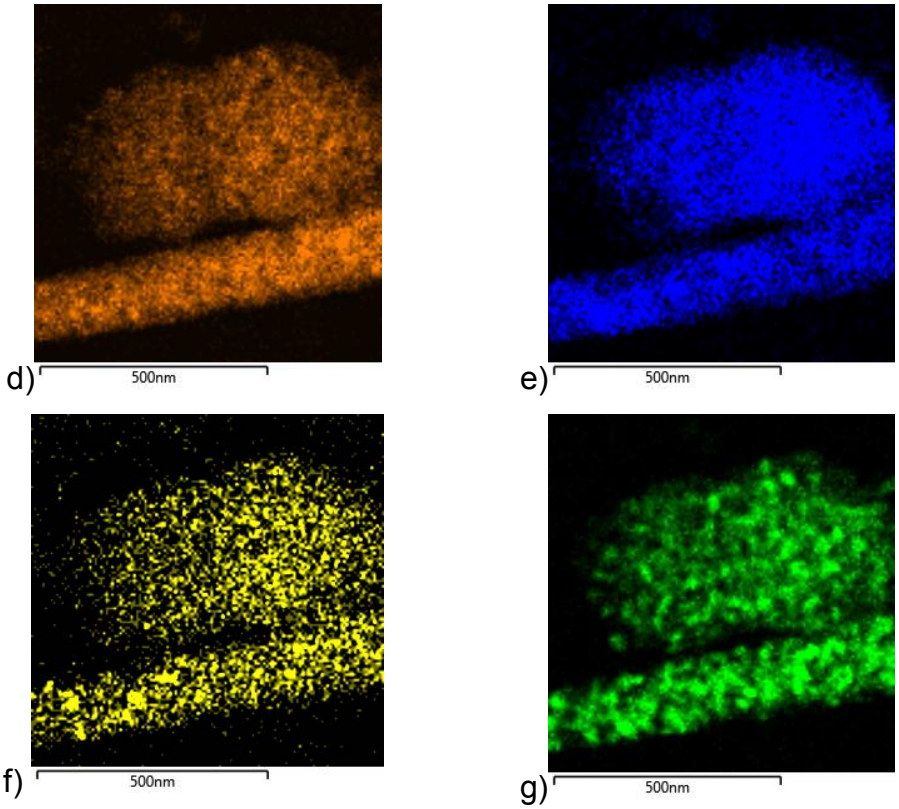

Figure 5.22 Element dispersion on the glass-ceramic particle from formulation 75-25 after nucleation treatment at 48h at 1006 K and 153 min at 1173 K. EDS images. a) original image; b) Si; c) Al; d) Mg; e) Sb; f) Zr and g) Ti.

At this moment of the crystallization cycle, the amount of crystalline phase is high, to the point that all elements are uniformly distributed through the analyzed region.

5.2 Part B

In this part of the work, the compositions studied during the masters and presented in table 1.1 were reformulated to have less titania and more zirconia, since the latter add no color to the glass and glass-ceramic. The new composition obtained from L2R4 was dubbed ZT1B4 and the one obtained from 75-25 was dubbed 75-25/ZT. Table 5.6 presents the new compositions.

Table 5.6 Glass compositions after reformulation.

Component	ZT1B4 (mol%)	75-25/ZT (mol%)
Al_2O_3	16.75	17.66
SiO_2	56.89	55.48
MgO	15.59	16.65
TiO_2	03.75	03.84
ZrO_2	03.76	03.62
Sb_2O_3	1.50	1.25
B_2O_3	1.80	1.50

5.2.1 Formulation ZT1B4

The raw powders, first the ZT1B4 and then the 75-25/ZT, were calcinated before melting to form the crystal phases. Fig 5.23 shows the XRD analyses of the ZT1B4 raw powder after the calcination cycle described at 4.1. By reason of the similarity of this composition with 75-25/ZT, the XRD of the calcinated powder of the latter will not be presented.

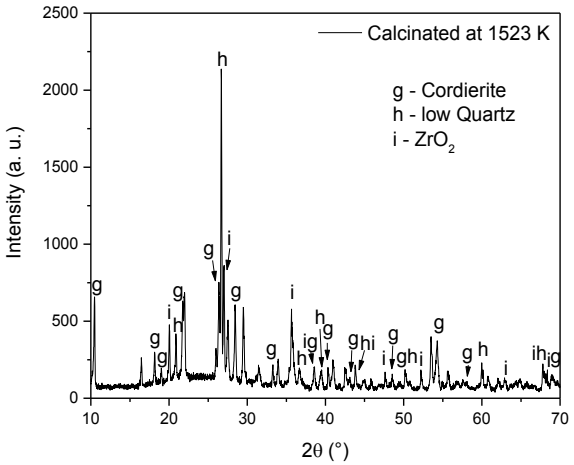

Figure 5.23 XRD of the ZT1B4 raw material. Three phases were identified.

To observe the thermal profile, DSC analysis of a powder and a bulk sample was conducted. Fig. 5.24 a) presents the result. Fig 5.24 b) presents, for the sake of comparison, the DSC analysis of L2R4 glass composition.

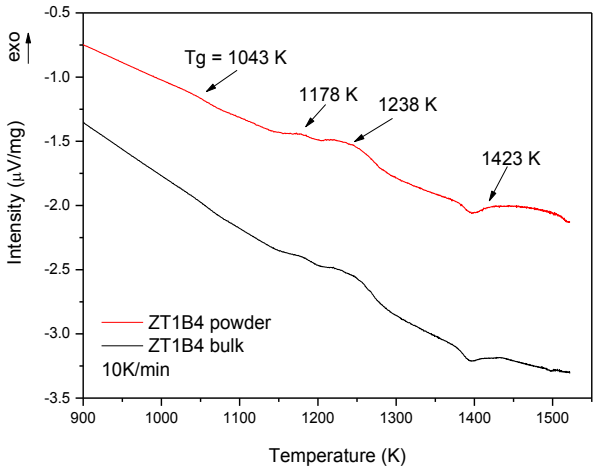

a)

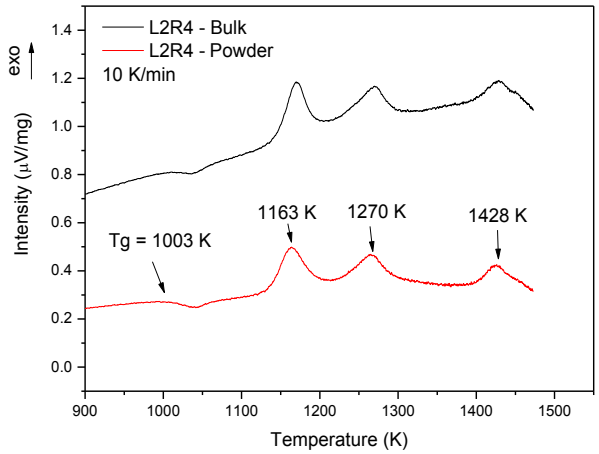

b)

Figure 5.24 DSC analysis of compositions a) ZT1B4 and b) L2R4.

It is important to say that the base line of the equipment was not good and that both the descent, observed on Fig 5.24 a) or ascent, observed on Fig 5.24 b) do not represent any microstructural changes on the glass. This setback does not compromise the analysis.

The change in proportion of the nucleating agents has promoted great difference on the thermal profile of the glasses. Original composition had sharper and more defined temperature peaks than the new glass. The last temperature shown in Fig 5.24 a) is actually the beginning of the peak, because it was broad and difficult to present a maximum. The coincidence between bulk and powder analyses indicate that the ZT1B4 glass composition also presents bulk nucleation. The glass transition temperature increased 40 K. The first crystallization peak was also displaced to higher temperatures; the second one, however, was shifted to lower temperatures. The third peak remained practically unchanged.

Aiming at obtaining transparent samples, a study was conducted to observe the temperature of the maximum nucleation rate. At this temperature, a higher number of nuclei is formed and then they will have less space to grow, for as they grow, their borders adjoin. If the resulting crystals have lower size than the wavelength of light (380-780 nm), they remain transparent.

This study was consisted of heat-treating samples for a fixed time (3 hours) at different temperatures close to Tg, where nucleation is preferred over crystallization. DSC analyses of these nucleated samples show the temperature shift by virtue of the nucleation process. There are two barriers to crystallization, one kinetic and another thermodynamic. Because of the presence of the nuclei, crystallization occurs at lower temperatures when compared to a parent non-heat-treated glass sample, as a result of lower thermodynamic barrier. Creating a nucleating site is needless since this process occurred during the 3-hour nucleating step.

Next, a graph of the inverse of crystallization peak maximum *versus* temperature of heat treatment is plot. The maximum indicates the temperature at which nucleation is maximum. The analyzed temperatures were 1003 K. 1023 K (below Tg), 1043 (Tg), 1063 K, 1073 K, 1083 K and 1093 K. Fig. 5.25 presents the DSC of the nucleated samples. The curves where dislocated to have from top-to-bottom, lowest-to-highest temperatures of heat-treatment.

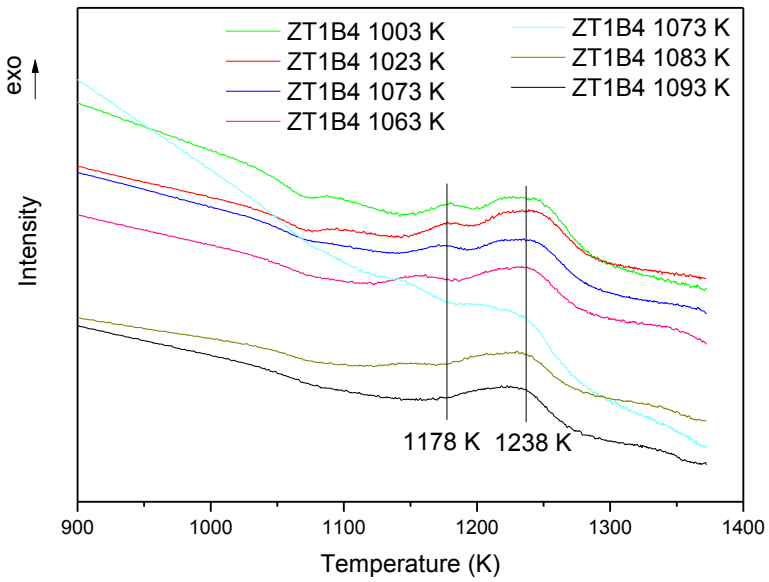

Figure 5.25 DSC analysis of 3-h-nucleated samples of ZT1B4 glass composition.

Straight vertical lines indicate the temperatures of the first and second crystallization peaks of the parent glass just to more easily observe the peak dislocation after heat treatment. Displacement towards lower temperatures of the first peak can be observed, and the second peak did not dislocate. From this curve, the inverse of the first peak maximum versus temperature of heat treatment was plot (Fig. 5.26). For the heat treatment at 1093 K, the first crystallization peak was no longer observed at the DSC.

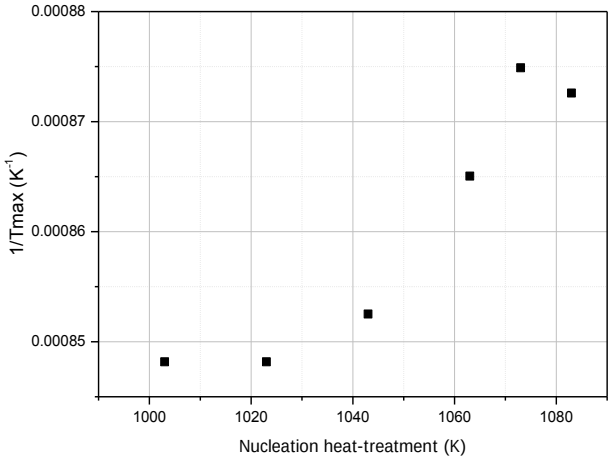

Figure 5.26 1/Tmax of the first crystallization peak *versus* nucleation temperature for the 3-h heat-treated samples of ZT1B4 glass composition.

The maximum is at 1073 K (30 K above Tg). This temperature was then chosen to nucleate the samples. Growth treatment was conducted at 1233 K, close to the second crystallization peak, for 3h for all samples. Nucleation time varied to observe which time leads to the highest improvement on mechanical properties. Table 5.7 presents the applied heat treatments as well as hardness and IFT values for the glass and glass-ceramics. Fig. 5.27 presents some samples after the heat treatments. The one after 20 min of nucleation at 1073 K and 3h of growth at 1233 K is opaque. After 40 min of nucleation and 3h of growth, the sample is translucent. Increasing nucleation time leads to transparent samples.

a) 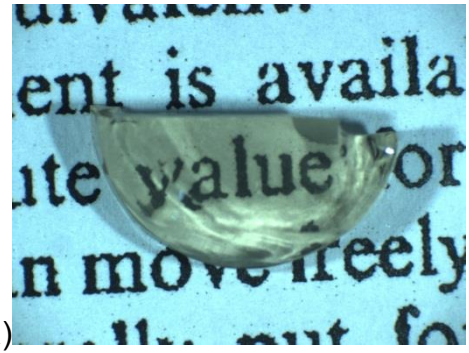 b) 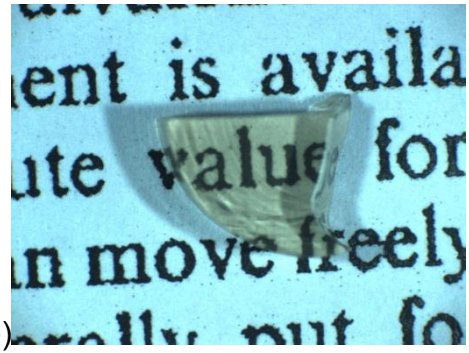

Figure 5.27 Glass-ceramic samples of ZT1B4 composition. a) Sample nucleated for 120 min at 1073 K and grew at 1233 for 3h and b) sample nucleated for 480 min at 1073 K and grew at 1233 for 3h.

Table 5.7 Hardness and IFT increase of parent glass and glass-ceramic samples from the ZT1B4 composition nucleated at different periods of time (Tn) at 1073 K and grew at 1233 K for 3h.

Tn (MIN)	**HARDNESS (GPa)**	**IFT INCREASE (%)**
Parent glass	6.68 ± 0.02	-
20	7.86 ± 0.03	15 ± 5
40	7.93 ± 0.07	30 ± 5
60	7.97 ± 0.03	10 ± 4
120	8.06 ± 0.03	30 ± 4
240	8.00 ± 0.05	36 ± 10
480	7.98 ± 0.04	8 ± 2

Mean hardness and IFT increase of the glass ceramics are close to 8 GPa and 30%, respectively. The L2R4 composition, which originated ZT1B4, has 10.2 GPa as mean hardness values of the glass-ceramic samples and IFT increase at approximately 50%. The lower values of these mechanical properties may indicate lower crystallinity of the new composition. The low crystallinity would also explain the less intense and broader DSC peaks of the new composition when compared with the original one. Fig. 5.28 shows the

XRD measurement that was conducted on the sample nucleated at 1073 K for 480 min and grown at 1233 K for 3h.

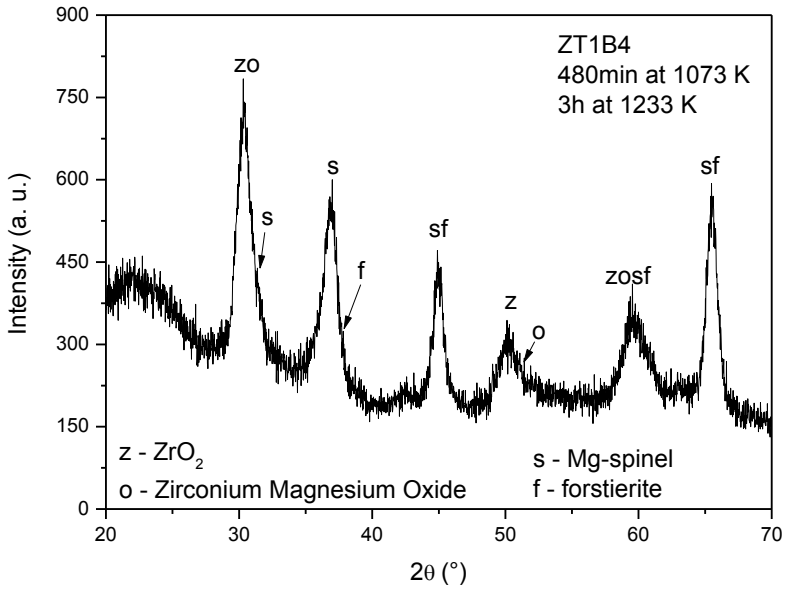

Figure 5.28 XRD pattern of ZT1B4 glass-ceramic heat-treated at 1073 K for 480 min and grew at 1233 K for 3h.

As it can be seen on fig 5.27, the transparency of the samples show that they are constituted of nanometric crystals. The transmission electron microscopy analysis performed on a powder sample and presented on Fig. 5.29 corroborates with this idea. When this type of material is analyzed, the XRD pattern is similar to the one presented in Fig. 5.28, with large and low-intensity peaks, making it not possible to infer the crystallinity degree after this analysis alone. The identification of the present crystal phases is also difficult, because of the larger peaks that coincide with a variety of phases. During the interpretation of this pattern, peaks of more than one crystal phase presented a match. The possible crystal phases are: Mg-spinel ($MgO.Al_2O_3$); forstierite ($2MgO.SiO_2$); zirconium oxide and zirconium and magnesium oxide ($Zr_{0,875}Mg_{0,125}O_{1,875}$). Since the diffraction patterns of these crystal phases are close, it is not possible to say that one or the other is present. Fig. 5.29 shows microstructure images obtained from transmission electron microscopy of a

sample nucleated for 60 min at 1073 K and with growth treatment at 1233 K for 3h.

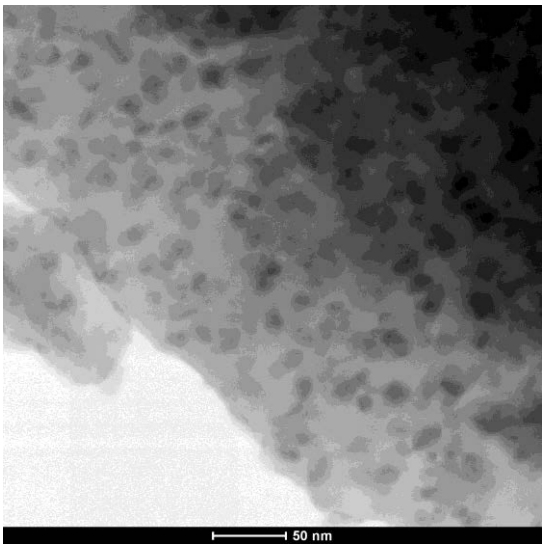

a)

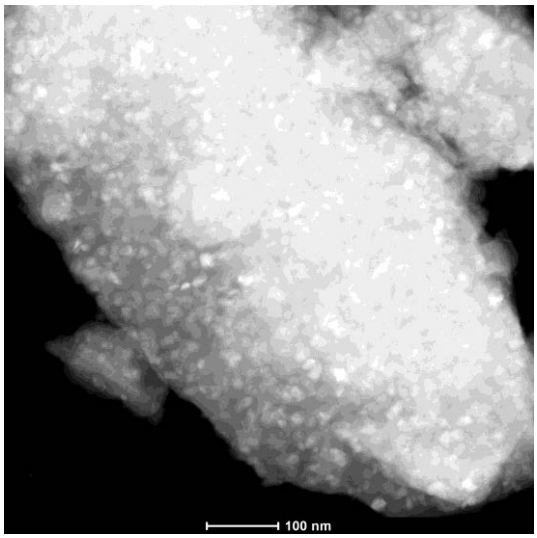

b)

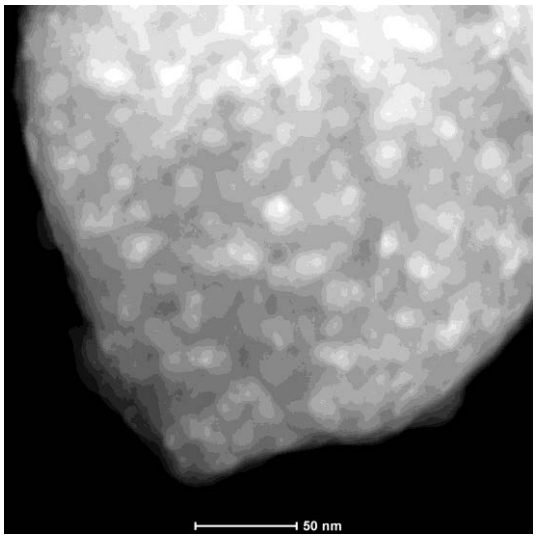

c)

Figure 5.29 Transmission electron microscopy analysis of a sample from formulation ZT1B4 after nucleation treatment at 1073 K for 60 min and growth treatment for 3h at 1233 K a) bright field, b) dark-field and c) high-angle annular dark-field (HAADF) images.

The analysis presented a material with a mean crystal value of about 20 nm. Although more than one phase is possibly present, the morphology of the crystals is the same. It is also possible to see that the crystals are far from each

other, thus facilitating further growth and hardness increase, since the crystal phase has higher hardness than the glass. Fig. 5.30 presents the element mapping on the sample.

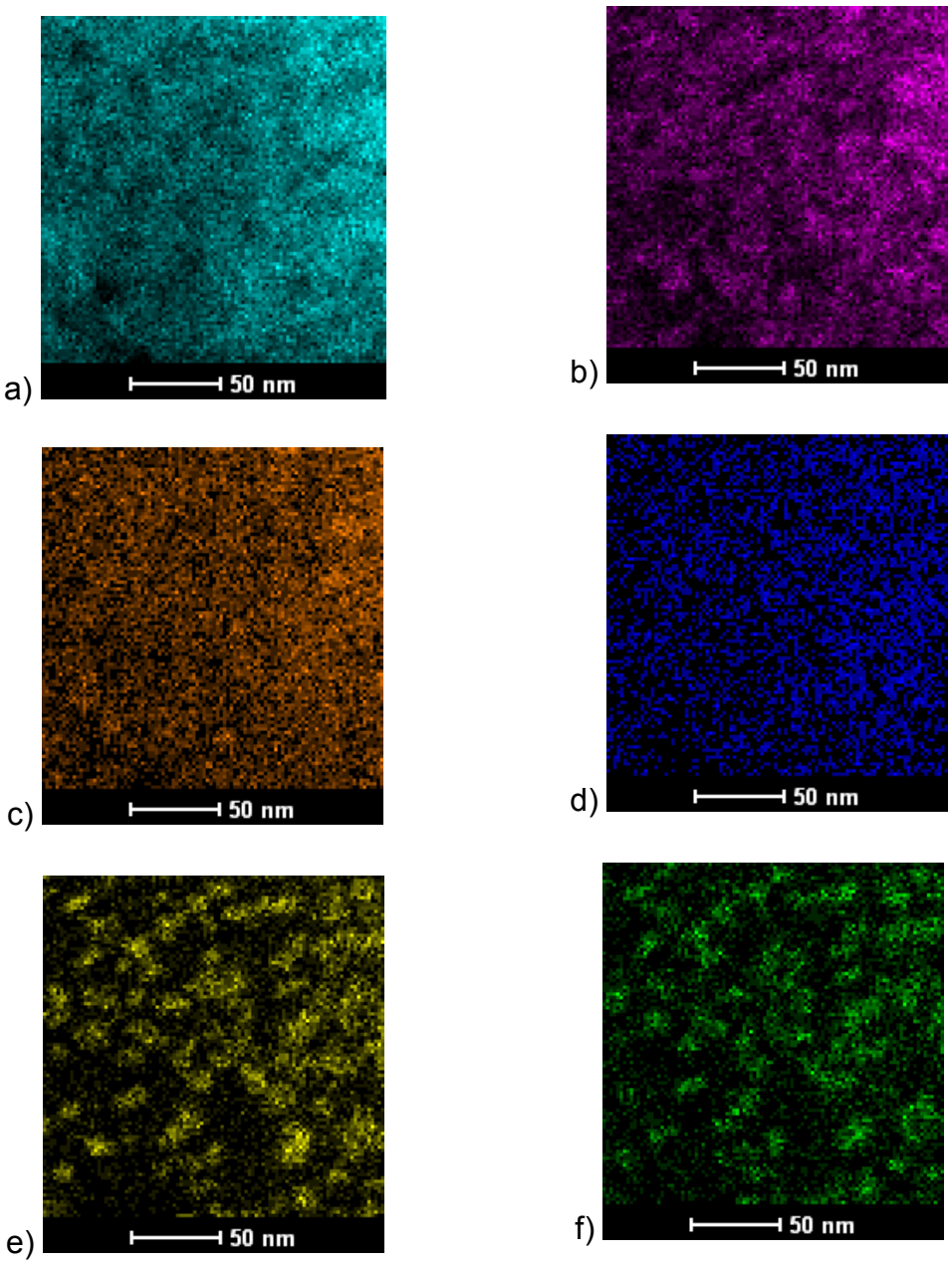

Figure 5.30 Element dispersion on the glass-ceramic particle from formulation ZT1B4 after nucleation treatment at 1073 K for 60 min and growth treatment for 3h at 1233 K. EDS images. a) Si; b) Al; c) Mg; d) Sb; e) Zr and f) Ti.

Magnesium and antimony are widely spread through the glassy and crystalline phase. Silicon is more concentrated, but still less than aluminum, and

both less than titanium and zirconium, the nucleating agents. Apparently, Ti and Zr are concentrated at the same spots.

Aiming at improving the mechanical properties through the increase on the crystalline fraction, new heat-treatments were conducted, with nucleation at the same temperature as applied before and with a 6-hour growth treatment (instead of 3h) at 1233 K. The resulting glass-ceramics are transparent, as can be seen in Fig. 5.31 and the mechanical properties are presented on table 5.8.

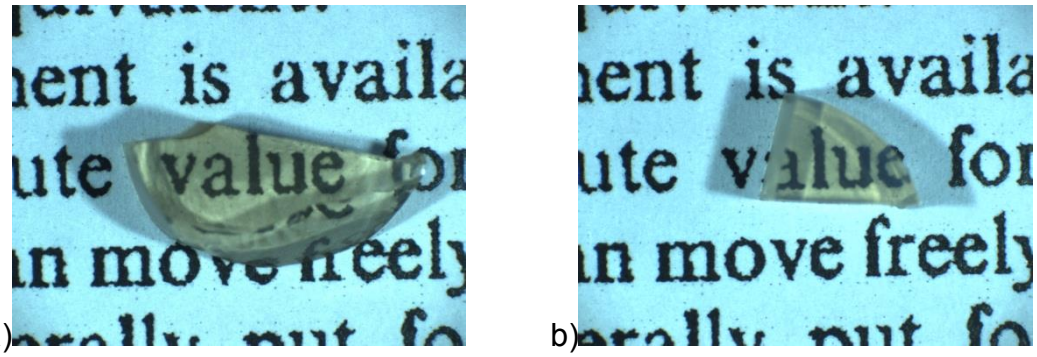

a) b)

Figure 5.31 ZT1B4 glass-ceramic samples. Nucleation at 1073 K for a) 120 min and b) 60 min. Both had a subsequent growth treatment at 1233 K for 6h.

Table 5.8 Hardness and IFT increase of parent glass and glass-ceramic samples from the ZT1B4 composition nucleated at different periods of time at (Tn) 1073 K and grew at 1233 K for 6h.

Tn (MIN)	HARDNESS (GPa)	IFT INCREASE (%)
60	7.94 ± 0.04	34 ± 7
120	7.82 ± 0.04	8 ± 3
240	7.73 ± 0.03	16 ± 6

No mechanical property increase was observed when the growth time went from 3h to 6h. Fig. 5.32 shows the XRD pattern of a glass-ceramic sample nucleated at 1073 K for 120 min and grown at 1233 K for 6h.

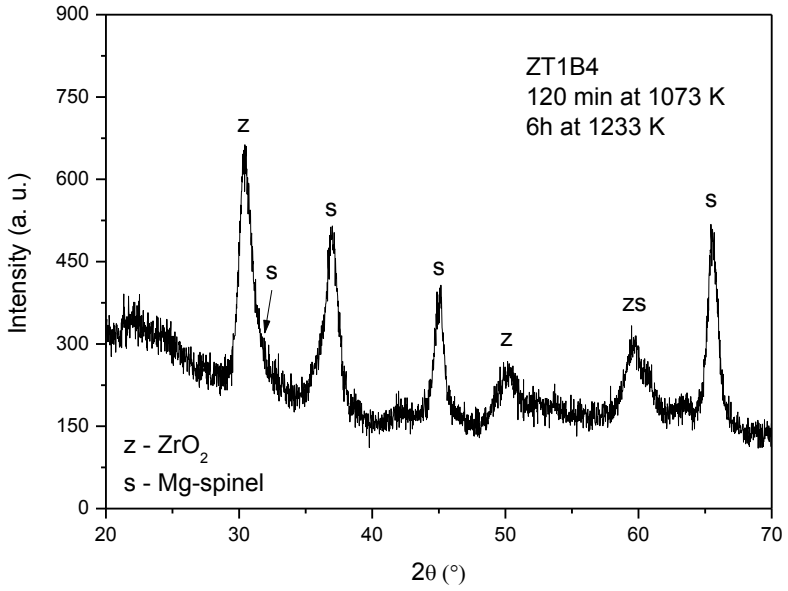

Figure 5.32 XRD pattern of ZT1B4 glass-ceramic heat-treated at 1073 K for 120 min and grew at 1233 K for 6h.

Once again, the presence of nanometric crystals enlarged the peaks, making it difficult to identify the crystal phases. It is possible that the sample has Mg-spinel and ZrO_2.

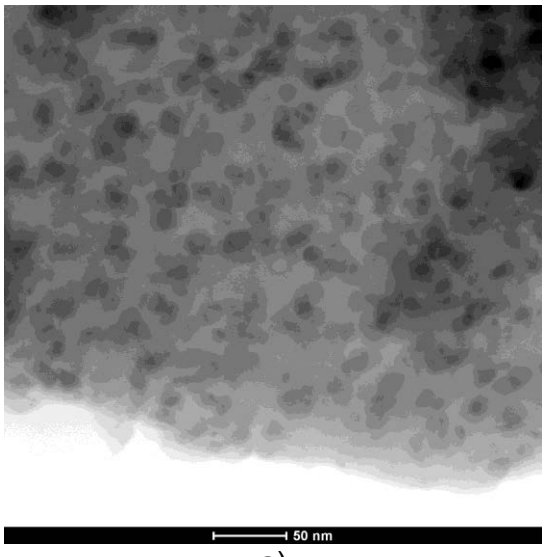

a)

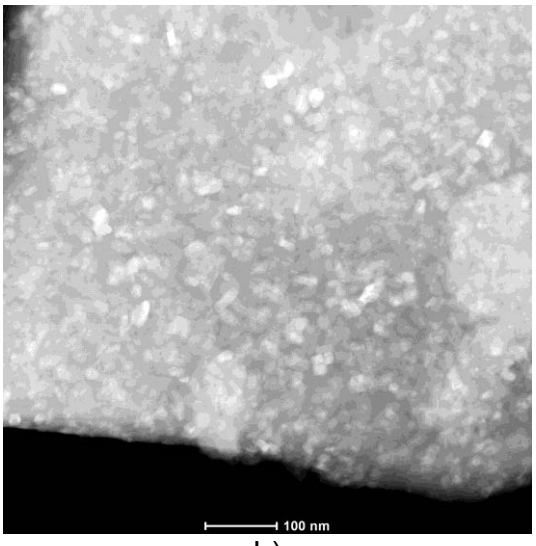

b)

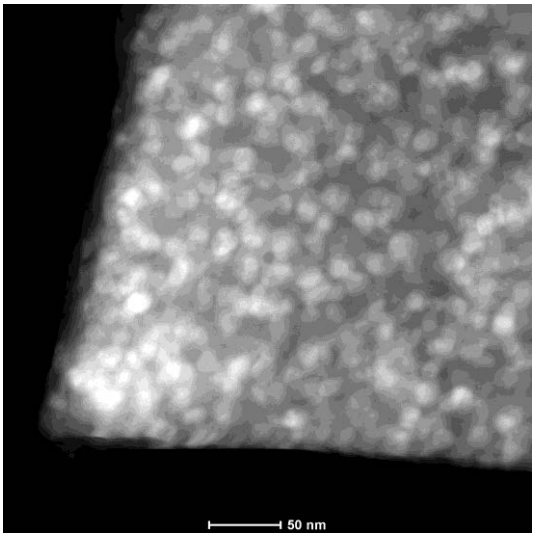

c)

Figure 5.33 Transmission electron microscopy analysis of a sample from formulation ZT1B4 after nucleation treatment at 1073 K for 60 min and growth treatment for 6h at 1233 K a) bright field, b) dark-field and c) HAADF images.

Mean crystal size is slightly higher than that for a sample with a 3-hour growth treatment. The dark-field images of both samples presented in Fig. 5.29 b) and Fig. 5.33 b) give a clear view of this fact. Fig. 5.34 presents the element mapping of this sample.

a) 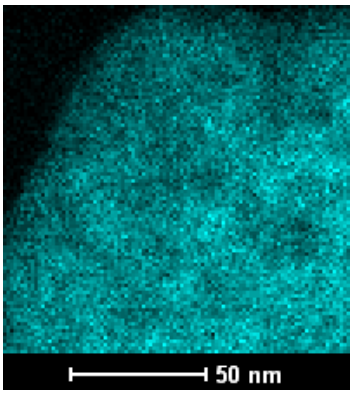

b) 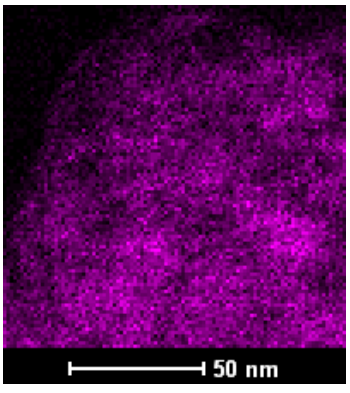

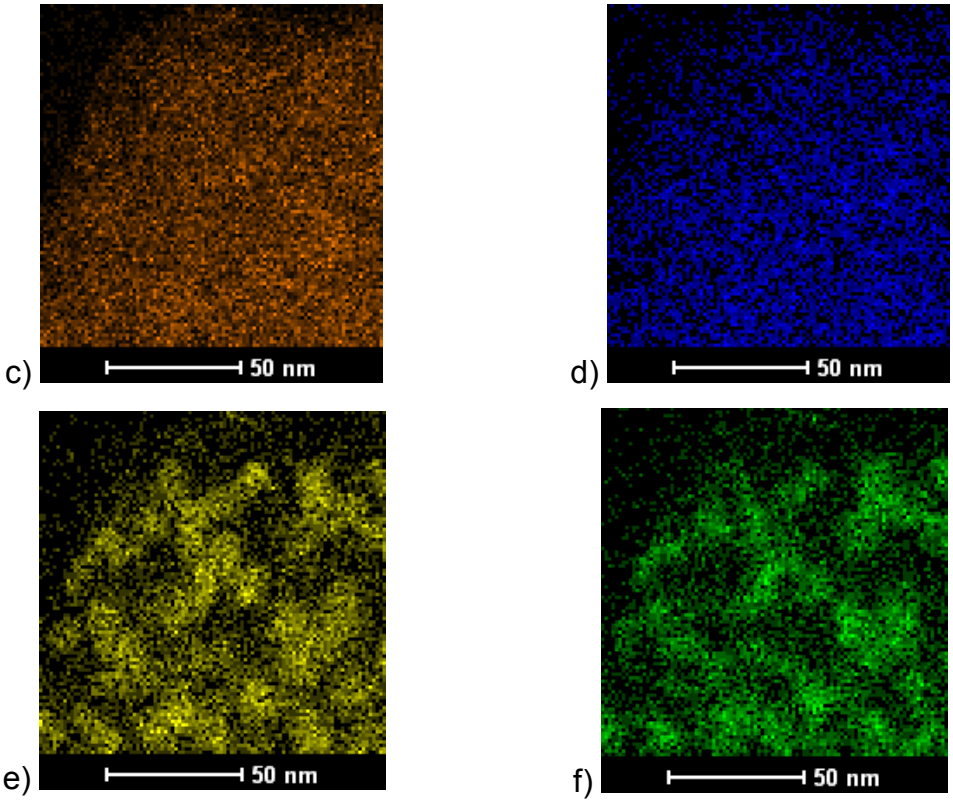

Figure 5.34 Element dispersion on the glass-ceramic particle from formulation ZT1B4 after nucleation treatment at 1073 K for 60 min and growth treatment for 6h at 1233 K. EDS images. a) Si; b) Al; c) Mg; d) Sb; e) Zr and f) Ti.

Comparing the element mapping of both samples, no significant difference can be observed, despite the mapping of Ti and Zr. Those elements are more concentrated when the 6-hour growth treatment was applied. This shows that even after the nucleation period, the nucleating agents still move and concentrate.

Both series of glass-ceramics present an IFT increase with highly disperse values and highly disperse errors. This is certainly due to the technique applied. Not all hardness tests generated cracks at the tip of the imprint, and the crack size for different imprints on the same glass-ceramic sample varied considerably, leading to the observed behavior. It is important to mention that this test was used only as a comparison between values of different glass-ceramics.

5.2.2 Formulation 75-25/ZT And Derivatives

Composition 75-25/ZT is presented on table 5.6. The thermal profile obtained by differential scanning calorimetry of a bulk and powder sample of this glass is presented in Fig. 5.35 a). For the sake of comparison, the DSC analysis of composition 75-25 is also presented (Fig. 5.35 b))

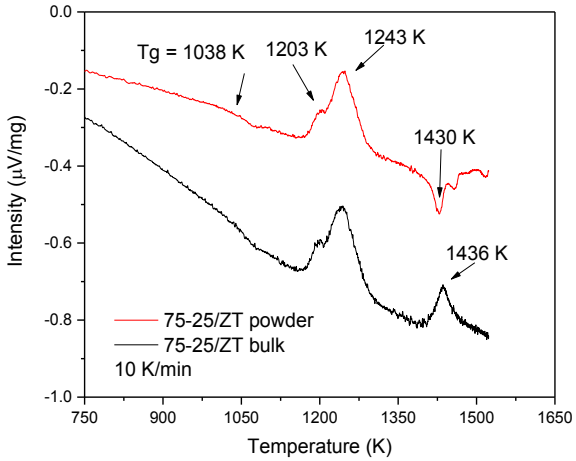

a)

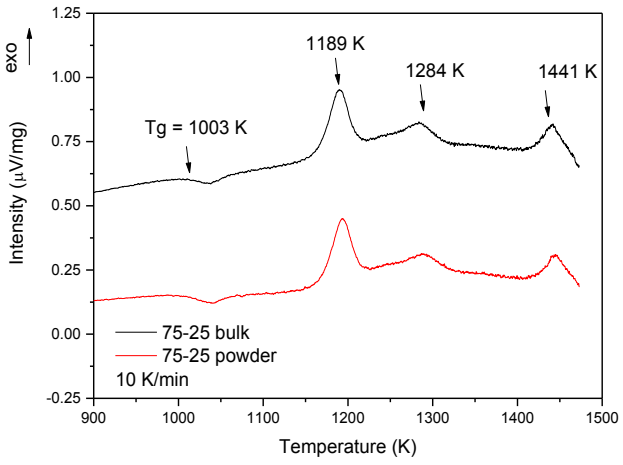

b)

Figure 5.35 DSC analysis of a) 75-25/ZT glass composition and b) 75-25 glass composition.

The first crystallization peak of the new composition almost merged to the second peak. The crystallization peaks were as intense as those of the original

composition, contrarily to what happened to ZT1B4 related to L2R4. Another remarkable difference between the reformulated glasses is that, for 75-25/ZT, only the first crystallization peak is at a higher temperature when compared to the original glass (75-25). The second and third peaks are at lower temperatures. It is important to note an unusual behavior at the DSC analysis of the bulk sample of composition 75-25/ZT. There is an endothermic at the temperature of 1430 K that shall not be mistakenly interpreted as melting, since the melting of this composition is around 1773 K. This endothermic event was not observed during the powder analysis. The coincidence of the temperature peaks on powder and bulk analysis is an indicative of internal nucleation.

A study to observe the temperature where nucleation is maximum was conducted. Bulk samples were heat-treated for three hours at 998 K, 1018 K (below Tg), 1038 K (Tg), 1058 K, 1078 K, 1098 K (above Tg). Fig 5.36 presents the DSC analysis of these samples. The curves were dislocated to have top-to-bottom, lowest-to-highest analyzed temperature. Straight vertical lines indicate the temperatures of the first and second crystallization peaks of a glass without heat treatment.

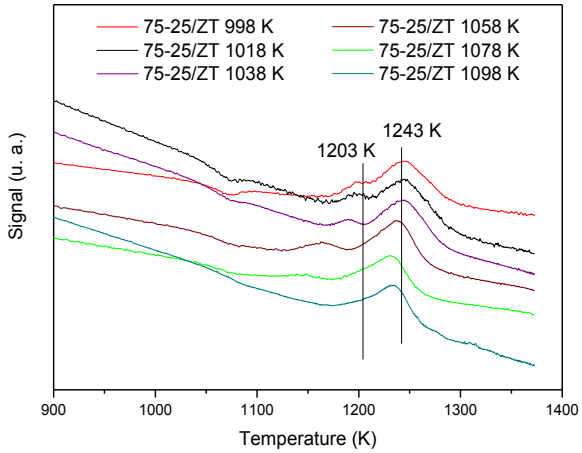

Figure 5.36 DSC curves of 75-25/ZT samples nucleated at different temperatures, for 3h.

It can be observed that, for some samples, the second crystallization peak dislocated to lower temperatures, contrarily to what happened to ZT1B4.

However, the first crystallization peak had a more pronounced dislocation. At higher temperatures, the first peak tends to disappear by reason of the intense nucleation. Fig. 5.37 presents a graph of the inverse of the first crystallization peak maximum *versus* heat treatment temperature

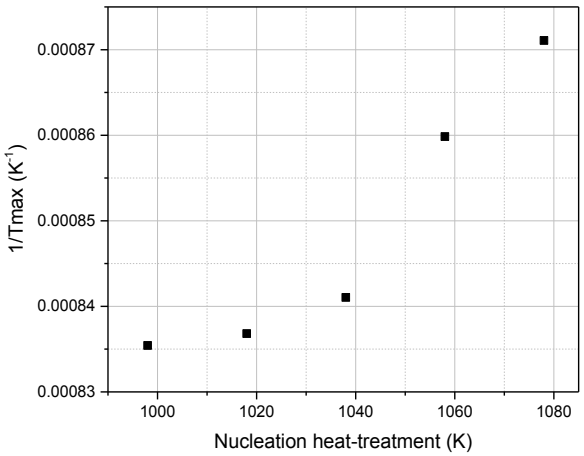

Figure 5.37 1/Tmax of the first crystallization peak *versus* nucleation temperature for the 3-h heat-treated samples of 75-25/ZT glass composition.

The maximum of this curve occurs at 1078 K. Two samples were prepared at 1098 K to observe the tendency of the curve and to see if the maximum was still at 1078 K, but after both analyses, the first crystallization peak was no longer observed. Then 1078 K was chosen as nucleation temperature. Growth treatment was performed at 1233 K for 3h. This is the temperature of the second crystallization peak after nucleation at 1078 K. Samples after double-stage heat treatment with nucleation at 1078 K even at the lowest times (120 min) were totally transparent with a light-yellow color, as it can be seen on Fig. 5.38. Table 5.9 presents the mechanical properties of the glass-ceramics and the glass.

a) 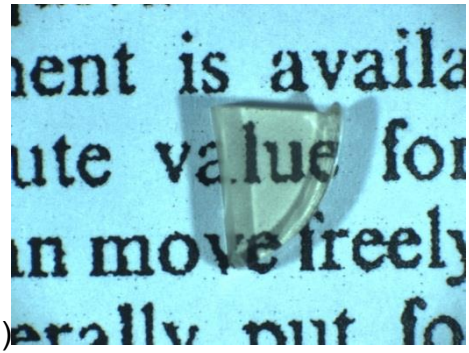 b) 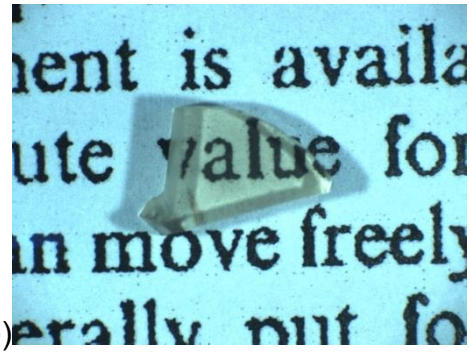

Figure 5.38 Glass-ceramic samples from formulation 75-25/ZT. a) sample nucleated at 1078 K for 120 min and with growth treatment at 1233 K for 3h. b) sample nucleated at 1078 K for 240 min and with growth treatment at 1233 K for 3h.

Table 5.9 Mechanical properties of glass and glass-ceramic samples from formulation 75-25/ZT nucleated at 1078 K for different periods of time and with growth treatment at 1233 K for 3h.

NUCLEATION TREATMENT (MIN)	**HARDNESS (GPa)**	**IFT INCREASE (%)**
GLASS SAMPLE	7.06 ± 0.03	-
120	8.27 ± 0.03	17 ± 2
240	8.14 ± 0.04	7 ± 2
360	8.23 ± 0.03	34 ± 5

As it occurred for formulation ZT1B4, an increase on the mechanical properties with relation to the original one (75-25) was not observed. 75-25 presented glass-ceramics with hardness up to 10.66 GPa and IFT increase in the order of 40%. Fig 5.39 presents XRD analysis of a sample after 360 min of nucleation at 1078 K and 3h of growth at 1233 K.

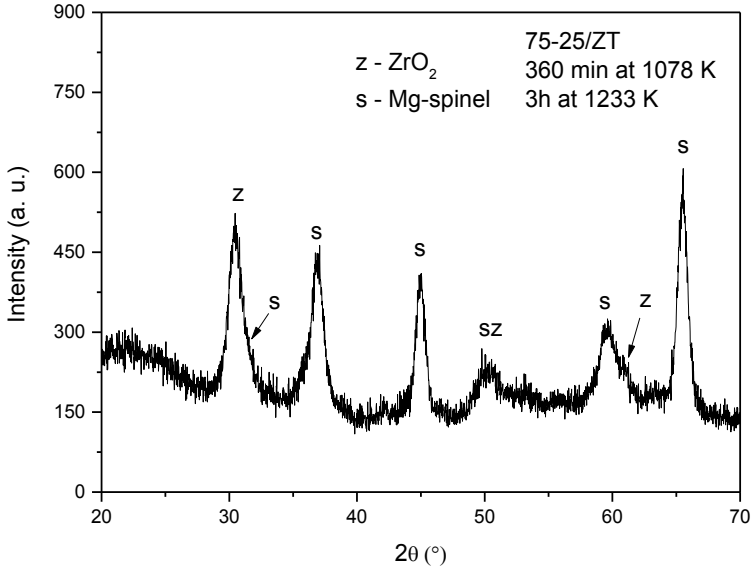

Figure 5.39 XRD pattern of glass-ceramic sample form 75-25/ZT after 360 min of nucleation at 1078 K and 3h of growth at 1233 K.

This diagram displays even less intense peaks than the one from the previous formulation. The residual glassy phase must be higher for this analyzed glass-ceramic than for the ones from formulation ZT1B4. The possible crystalline phases are Mg-spinel and zirconia. Microstructure analysis was performed with transmission electron microscopy. Fig. 5.40 shows bright field, dark-field and HAADF images of the crystals. The analyzed sample was nucleated for 120 min at 1078 K and had growth treatment at 1233 K for 3h. The sample was ground prior to the analysis.

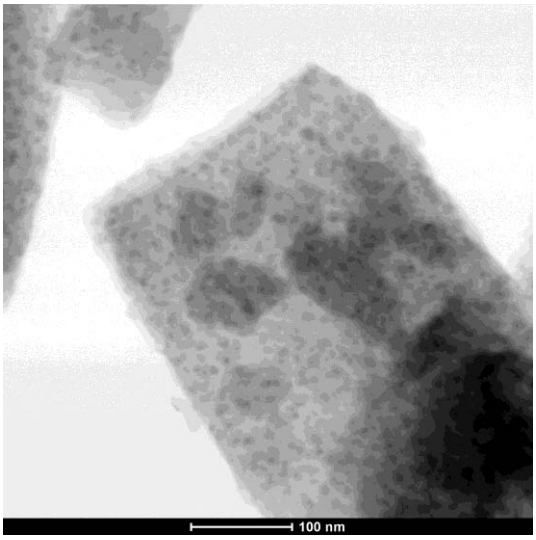

a)

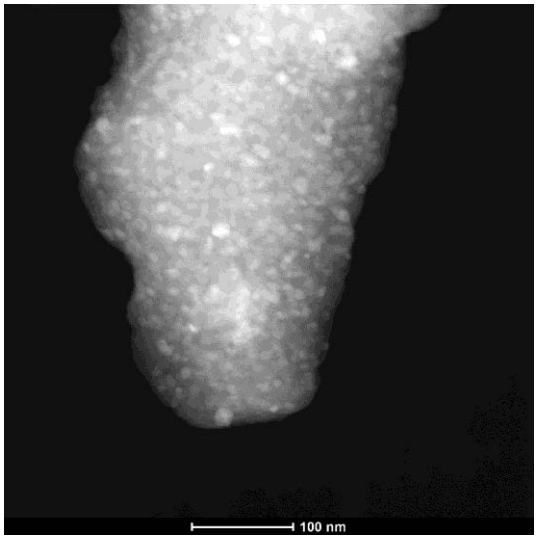

b)

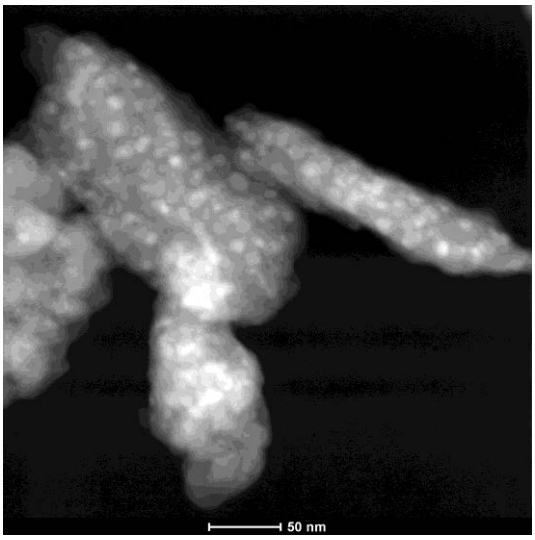

c)

Figure 5.40 Transmission electron microscopy analysis of a sample from formulation 75-25/ZT after nucleation treatment at 1078 K for 120 min and growth treatment for 3h at 1233 K a) bright field, b) dark-field and c) HAADF images.

Images indicate that samples are highly crystallized, but with totally unconnected crystals, making possible to improve growth time and increase crystallized fraction. Crystal size is on the range of 10 – 15 nm. Although the XRD pattern indicates two possible phases present, the morphology of the crystals does not allow to discriminate each. Observing the bright field image,

one notices darker regions inside the bigger particle. It is possible to distinguish crystals and a glassy phase in those regions, so it must be a simple superposition of particles. Fig. 5.41 presents the element distribution on the crystals, obtained by an energy dispersive x-ray (EDS) detector during the TEM analysis. The analyzed region is the one shown in fig 5.42 a).

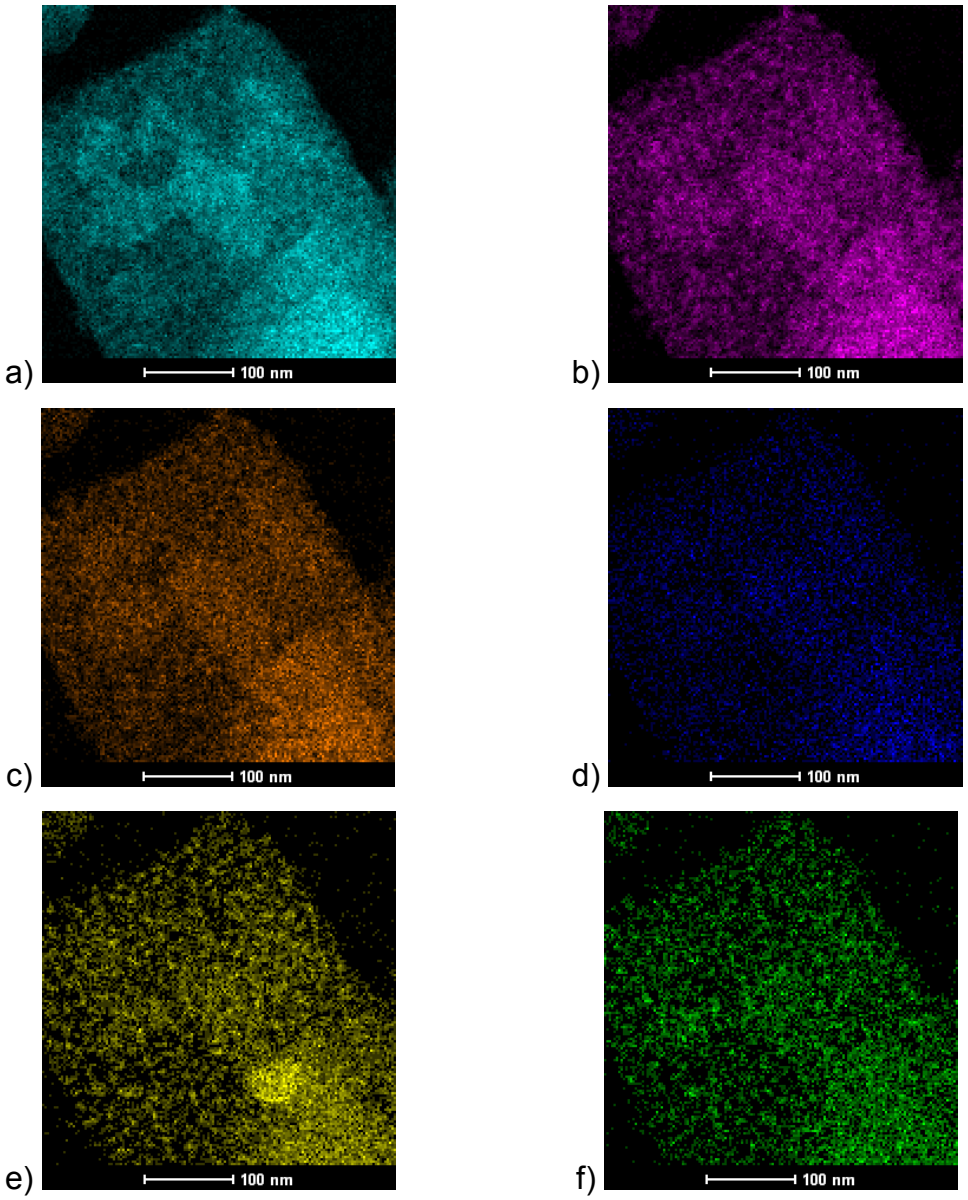

Figure 5.41 Element dispersion on the glass-ceramic particle from formulation 75-25/ZT after nucleation treatment at 1078 K for 120 min and growth treatment for 3h at 1233 K. EDS images. a) Si; b) Al; c) Mg; d) Sb; e) Zr and f) Ti.

All the elements but Zr are uniformly distributed through the sample. An apparent higher concentration density of Si, Al and Mg can be explained by the superposition of particles. Zr on the other hand is well concentrated on a spot, that must be of a ZrO_2 particle.

With the objective of increasing mechanical properties, new double-stage heat treatments were performed, with growth treatment of 6h at 1233 K, instead of 3h. The glass-ceramics resulting from this heat-treatment are also transparent, as it can be seen in Fig. 5.42. Table 5.10 presents the mechanical properties of the glass-ceramics.

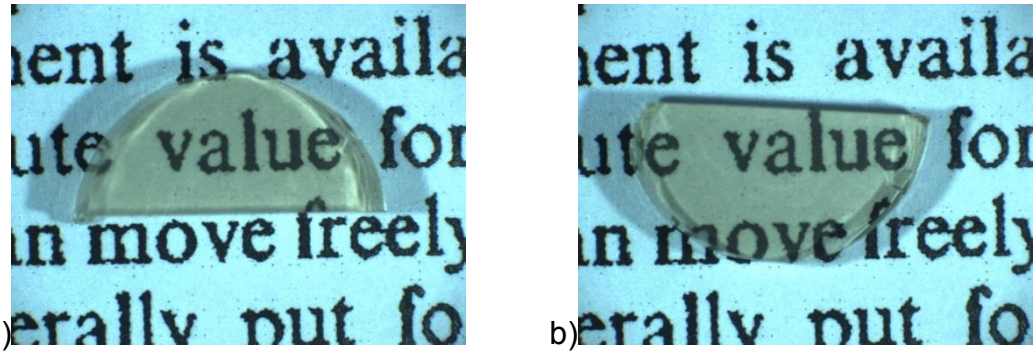

a) b)

Figure 5.42 75-25/ZT glass-ceramic samples a) nucleated at 1078 K for 120 min and with growth treatment at 1233 K for 6h and b) nucleated at 1078 K for 240 min and with growth treatment at 1233 K for 6h.

Table 5.10 Mechanical properties of formulation 75-25/ZT, nucleated at different times at 1078 K and with growth treatment at 1233 K for 6h.

NUCLEATION TREATMENT (MIN)	**HARDNESS (GPa)**	**IFT INCREASE (%)**
120	8.83 ± 0.03	4 ± 3
240	9.04 ± 0.03	5 ± 5
360	9.01 ± 0.04	6 ± 3

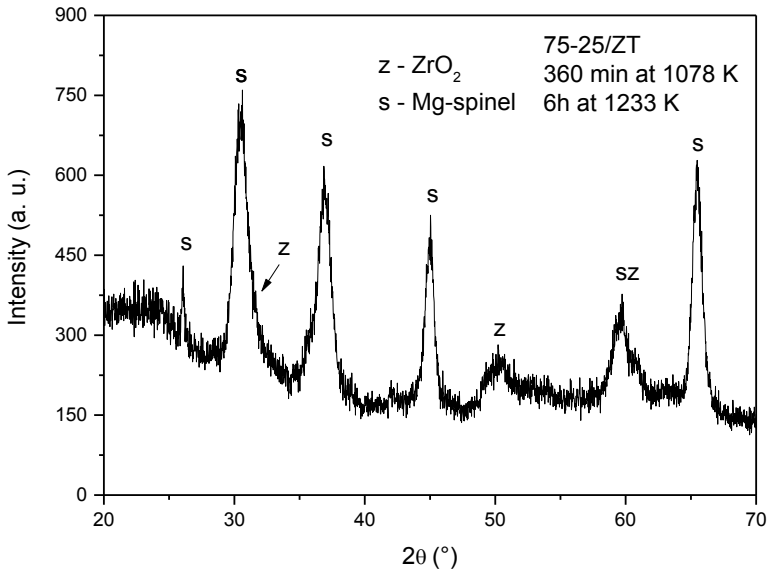

Figure 5.43 XRD pattern of glass-ceramic sample nucleated for 360 min at 1078 K and with growth treatment for 6h at 1233 K.

The intensity of the XRD peaks increased when compared to the former analysis. The crystal phases possibly present are the same as for when the growth treatment was 3h. There is also an increase on hardness but nothing relevant when it comes to IFT increase. This series of heat-treatments was the one that presented the highest increase on hardness, but formulations 75-25 and L2R4 still have glass-ceramics with higher values of this property. Microstructure analysis was performed with transmission electron microscopy. Fig. 5.44 presents bright field, dark-field and HAADF images of the crystals. The analyzed sample was nucleated for 240 min at 1078 K and had growth treatment at 1233 K for 6h. The sample was ground prior to the analysis.

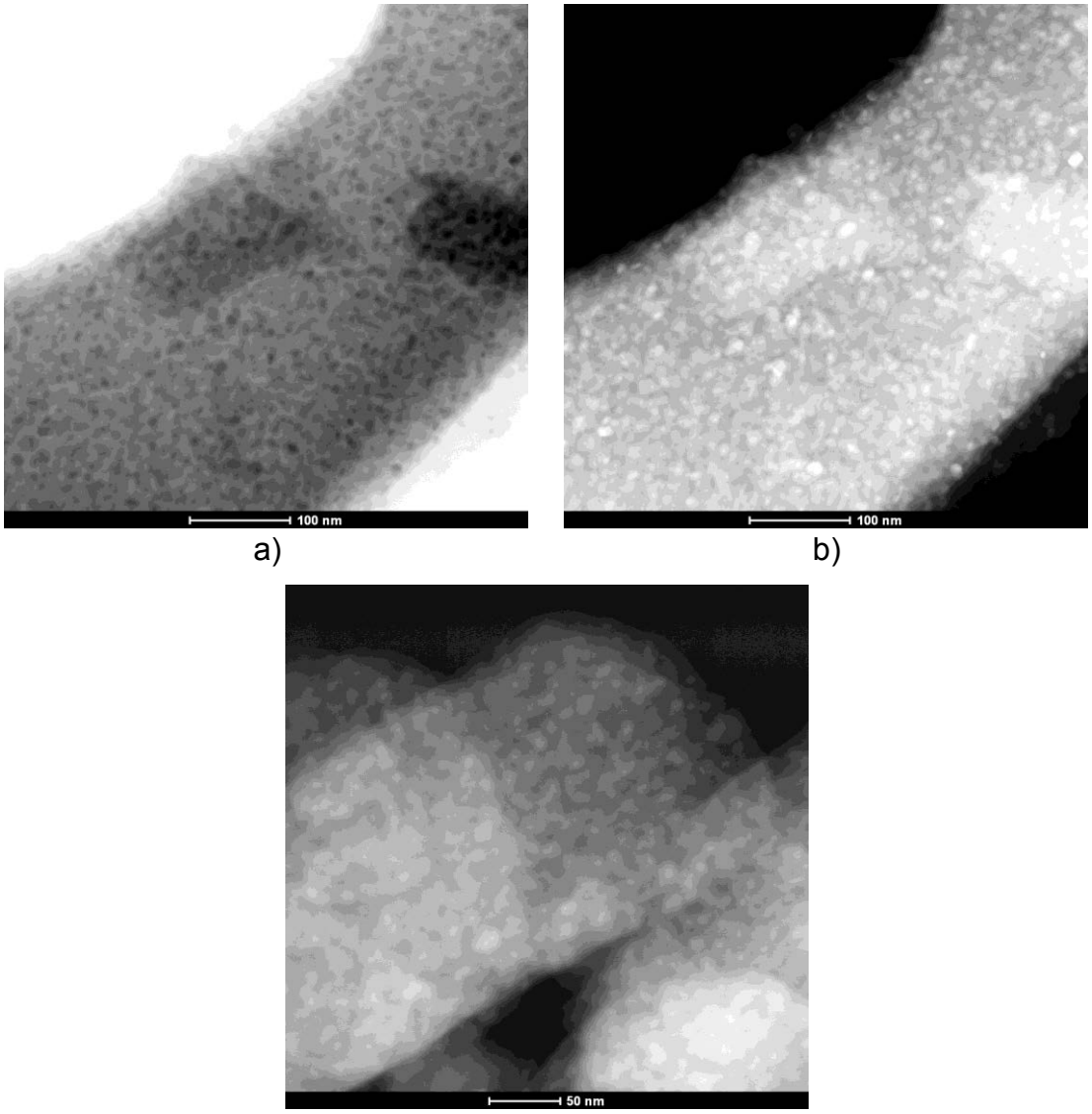

a) b)

c)

Figure 5.44 Transmission electron microscopy analysis of a sample from formulation 75-25/ZT after nucleation treatment at 1078 K for 240 min and growth treatment for 6h at 1233 K a) bright field, b) dark-field and c) HAADF images.

As it can be seen, the samples are densely crystallized, with mean crystal size lower than 10 nm, but with an unneglectable residual glassy phase, which would lead to the thought that an increase on crystal volume fraction would still be possible. After visual observation, one sees that the crystals are isolated, not in contact with one another. There are two possibilities that would explain this

behavior: the crystallization kinetics is low, so it would take the crystals longer periods of time at the growth temperature to grow until the point their borders are adjoined; or there is a courtyard effect on this glass. The courtyard effect was first observed by Fokin et al. [88] after studies on glass composition close to $1Na_2O.2CaO.3SiO_2$. In this glass, the presence of pre-existing crystals forecloses the formation of new ones on their proximity, at the nucleation temperature. The crystal growth for the nucleated crystals diminish as the primarily formed crystals are larger.

It was shown that for that glass system, the prime crystals are Na-rich on the first stages of the growth process and if a nucleation step is applied after a primary growth, the vicinity of the first crystals would be Na-poor, and no nucleation would occur there. A parallel could be made to formulation 75-25/ZT. Fig 5.45 presents the element distribution on the crystals, obtained by EDS detector during the TEM analysis.

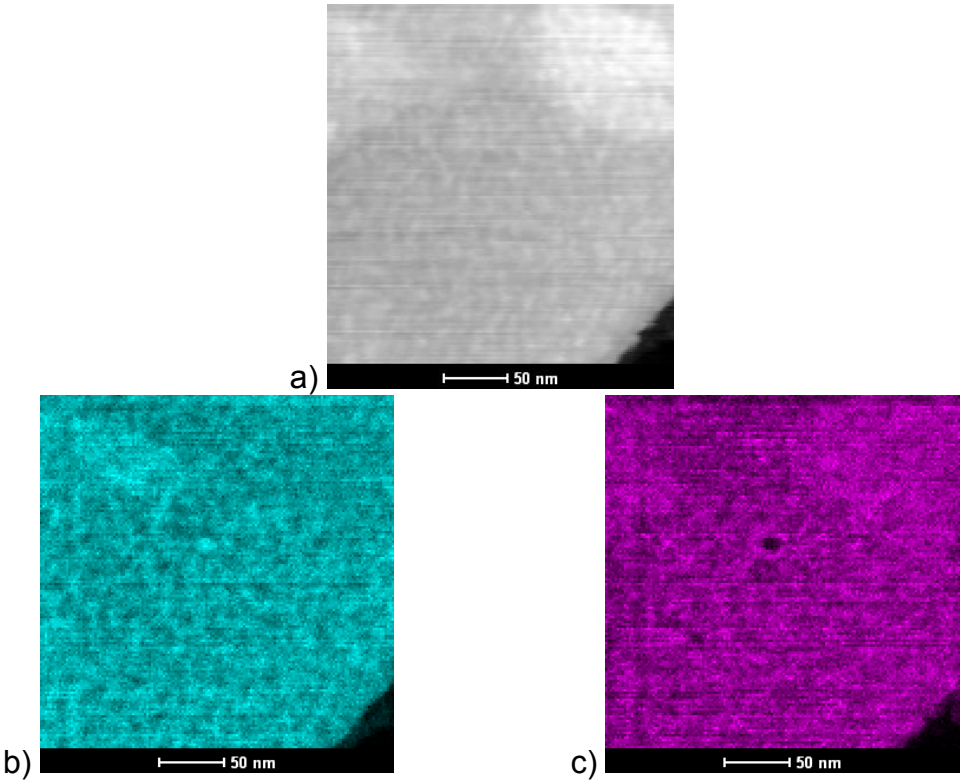

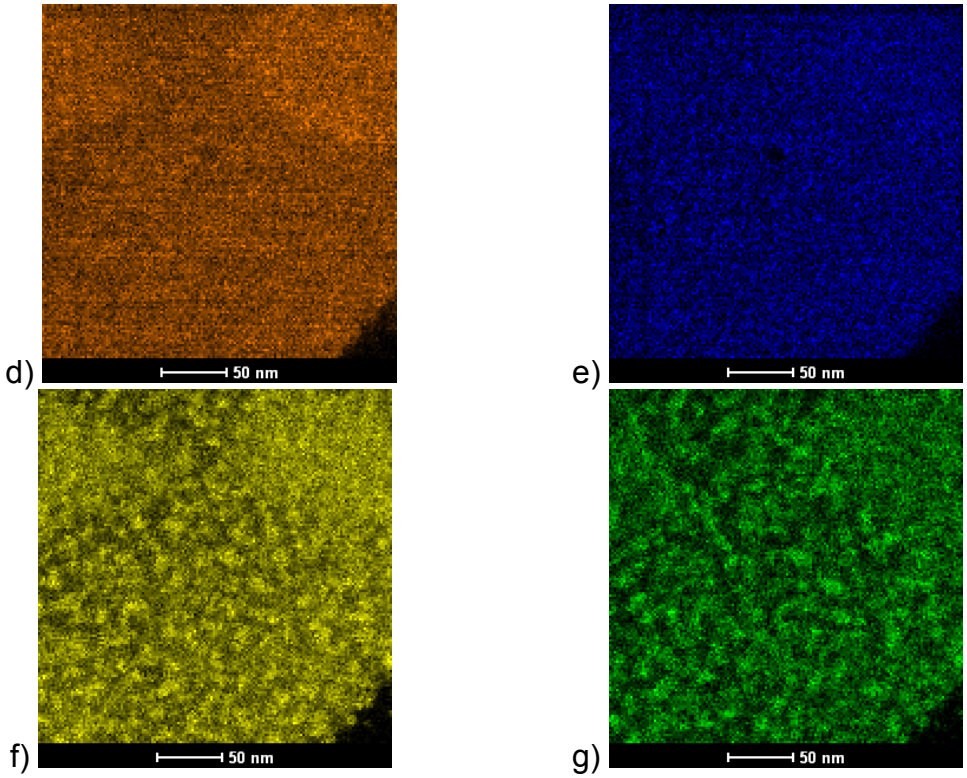

Figure 5.45 Element dispersion on the glass-ceramic particle from formulation 75-25/ZT after nucleation treatment at 1078 K for 240 min and growth treatment for 6h at 1233 K. EDS images. a) original image used for EDS analysis and the elements present: b) Si; c) Al; d) Mg; e) Sb; f) Zr and g) Ti.

The crystals are Ti- and Zr-rich, with Mg well spread over the glass-ceramic particle. Si and Al are more concentrated, but not as much as the nucleating agents. Because this formulation was the only that responded to the change on growth treatment, which leads to an increase on hardness, it was reformulated. The new compositions were called 75-25/25Ti and 75-25/0Ti. The former had the sum TiO_2 + ZrO_2 kept the same as in 75-25/ZT, but with a higher content of ZrO_2. 75% of the amount of nucleating agents, in mole, is ZrO_2 and 25% is TiO_2. Composition 75-25/0Ti on the other hand, had ZrO_2 as major nucleating agent with a minor addition of TiO_2. Table 5.11 presents the composition of formulation 75-25/25Ti, 75-25/0Ti and 75-25/ZT as comparison.

Table 5.11 Composition of new formulations 75-25/25Ti and 75-25/0Ti. Original composition 75-25/ZT is presented for comparison.

Component	**75-25/ZT**	**75-25/25Ti**	**75-25/0Ti**
Al_2O_3	17.66	17.67	17.67
SiO_2	55.48	55.52	55.52
MgO	16.65	16.66	16.66
TiO_2	03.84	01.85	0.50
ZrO_2	03.62	05.55	6.90
Sb_2O_3	1.25	1.25	1.25
B_2O_3	1.50	1.50	1.50

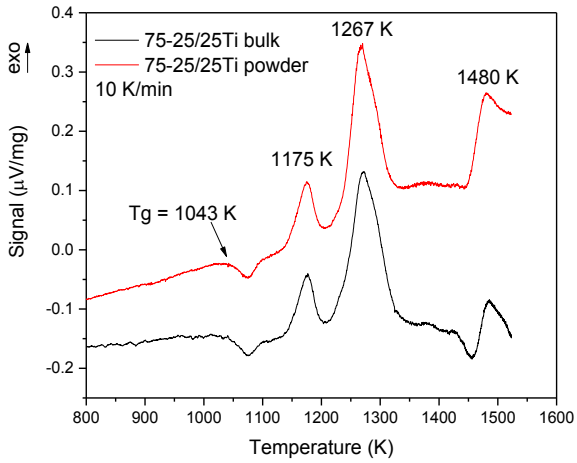

a)

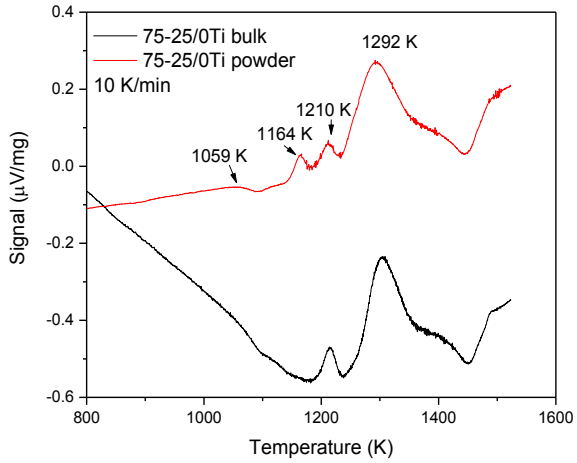

b)

Figure 5.46 DSC analysis of formulation a) 75-25/25Ti and b) 75-25/0Ti.

It was observed after the melting of composition 75-25/0Ti that not all ZrO_2 was dissolved in the glass. It was possible to see an important amount of undissolved material on the bottom of the platinum crucible. This indicates that the composition differs from the one presented on table 5.11. The DSC curve of a powder sample from this composition presented a crystallization peak which had not been seen in the bulk sample at 1164 K. That must be a crystal phase present only at the surface. Due to these two facts, this composition was discarded.

Composition 75-25/25Ti presented well-defined crystallization peaks, with powder and bulk samples having the same crystallization peak temperatures. Both glasses present 3 crystallization peaks up to 1523 K. The first peak of the new composition is the only one to appear at a lower temperature compared to the original glass. A study to observe where nucleation is maximum was carried out: samples were nucleated for 3h at 1013 K, 1033 K (below Tg), 1053 K, 1073 K and 1103 K (above Tg). Fig. 5.47 presents the DSC analysis of the nucleated samples. The curves were dislocated to have top-to-bottom, lowest-to-highest nucleation temperatures, the same way as presented on the analysis of compositions ZT1B4 and 75-25/ZT. Straight lines indicate first and second crystallization peaks of glass without heat treatment.

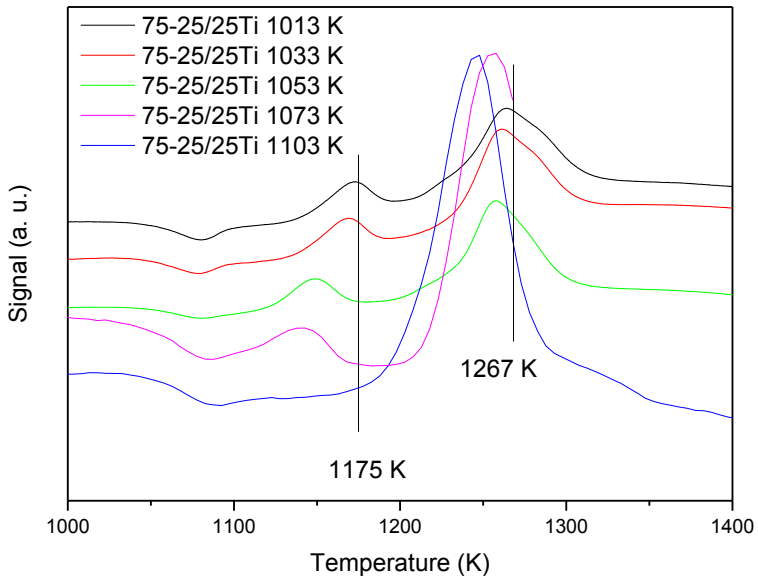

Figure 5.47 DSC curves of 75-25/25Ti samples nucleated at different temperatures, for 3h.

The behavior of nucleated samples from formulation 75-25/25Ti is similar to 75-25/ZT, since both crystallization peaks were dislocated to lower temperatures. For the highest nucleation temperature analyzed, 1103 K, the crystallization peak was no longer present. The second crystallization peak had a more pronounced displacement towards lower temperatures for formulation

75-25/25Ti (20 K) than for formulation 75-25/ZT (10 K). The first crystallization peak, however, presented higher displacement towards lower temperatures for formulation 75-25/ZT (55 K) than for 75-25/25Ti (35 K). This can be seen as an indication that the nucleation process is more intense on 75-25/ZT. Since the first peak was the one that promoted the highest temperature displacement, it was chosen as the nucleation temperature. Fig. 5.48 presents the graph of the inverse of first peak maximum *versus* nucleation heat-treatment.

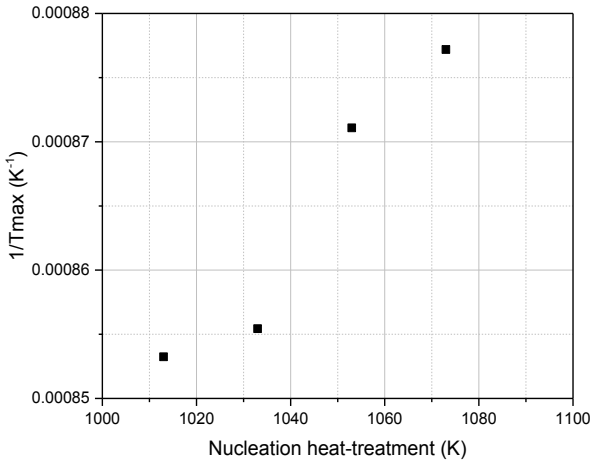

Figure 5.48 1/Tmax of the first crystallization peak *versus* nucleation temperature for the 3h heat-treated samples of 75-25/25Ti glass composition.

The highest value of the curve was observed at 1073 K, once again, for a higher temperature, the first crystallization peak was not observed. Temperature 1073 K was then chosen as the nucleating temperature for this composition. Growth treatment was performed at 1243 K for 3h. This is the temperature of the second crystallization peak after a 3h-nucleation step at 1073 K. Samples after double-stage were totally transparent and presented the same coloration of the parent glass. Remarkably, the glass was fragile and cracked during cutting, even after the long annealing process. Fig. 5.49 presents images of glass-ceramic samples. Table 5.12 presents the mechanical properties of the glass-ceramics and the glass.

a) 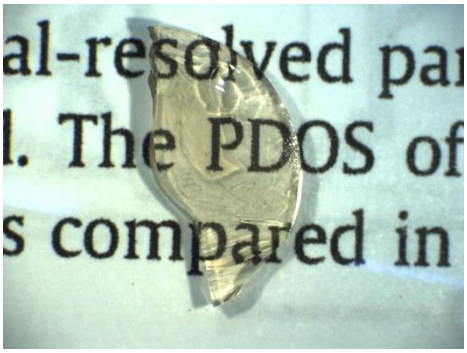

b) 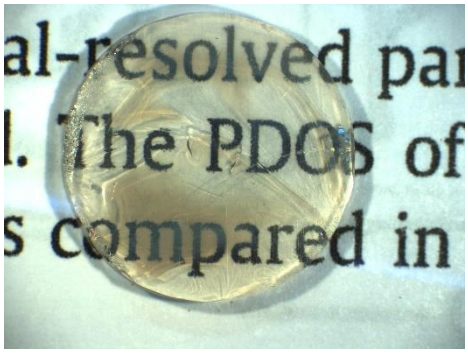

Figure 5.49 Glass-ceramic samples from 75-25/25Ti. a) sample nucleated at 1073 K for 1440 min (1 day) and with growth treatment at 1243 K for 3h. b) sample nucleated at 1073 K for 11520 min (8 days) and with growth treatment at 1243 K for 3h.

Table 5.12 Mechanical properties of formulation 75-25/25Ti, nucleated at different times at 1073 K and with growth treatment at 1243 K for 3h.

NUCLEATION TREATMENT (MIN)	**HARDNESS (GPa)**	**IFT INCREASE (%)**
GLASS SAMPLE	7.68 ± 0.06	-
1440	8.5 ± 0.1	30 ± 10
4260	8.51 ± 0.04	29 ± 7
11520	9.17 ± 0.07	26 ± 3

Glass hardness was the highest one for this formulation, but glass-ceramics had no significant increase after double-stage heat treatments for nucleation periods of 1440 min (1 day) and 4260 min (2 days and 23h). Only after 8 days of nucleation and 3h of growth, hardness changed to values close to those obtained with formulation 75-25/ZT, after 6h of growth. IFT increase is more significant here than for 75-25/ZT, although the associated errors were

also higher. Fig. 5.50 presents a XRD pattern of the sample nucleated at 1073 K for 11520 min and with growth treatment at 1243 K for 3h.

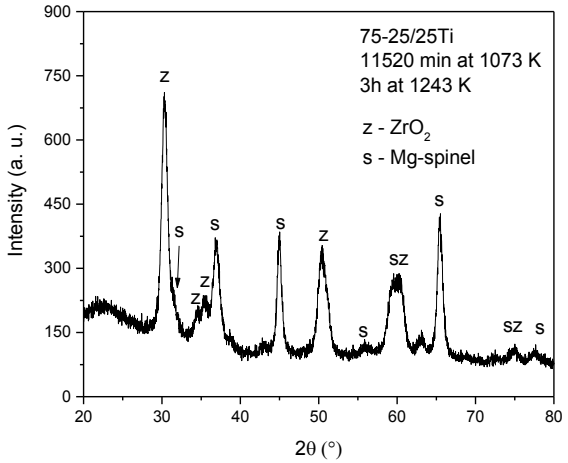

Figure 5.50 XRD pattern of glass-ceramic sample nucleated for 11520 min (8 days) at 1073 K and with growth treatment for 3h at 1243 K.

The possible crystal phases present are ZrO_2 and Mg-spinel. The presence of the former is understandable because of the low solubility in silicates. The latter promotes the increase in mechanical properties. Microstructure analysis was performed with transmission electron microscopy. Fig. 5.51 presents bright field, dark-field and HAADF images of the crystals. The sample was nucleated at 1073 K for 8 days and with growth treatment at 1243 K for 3h. The sample was ground prior to the analysis.

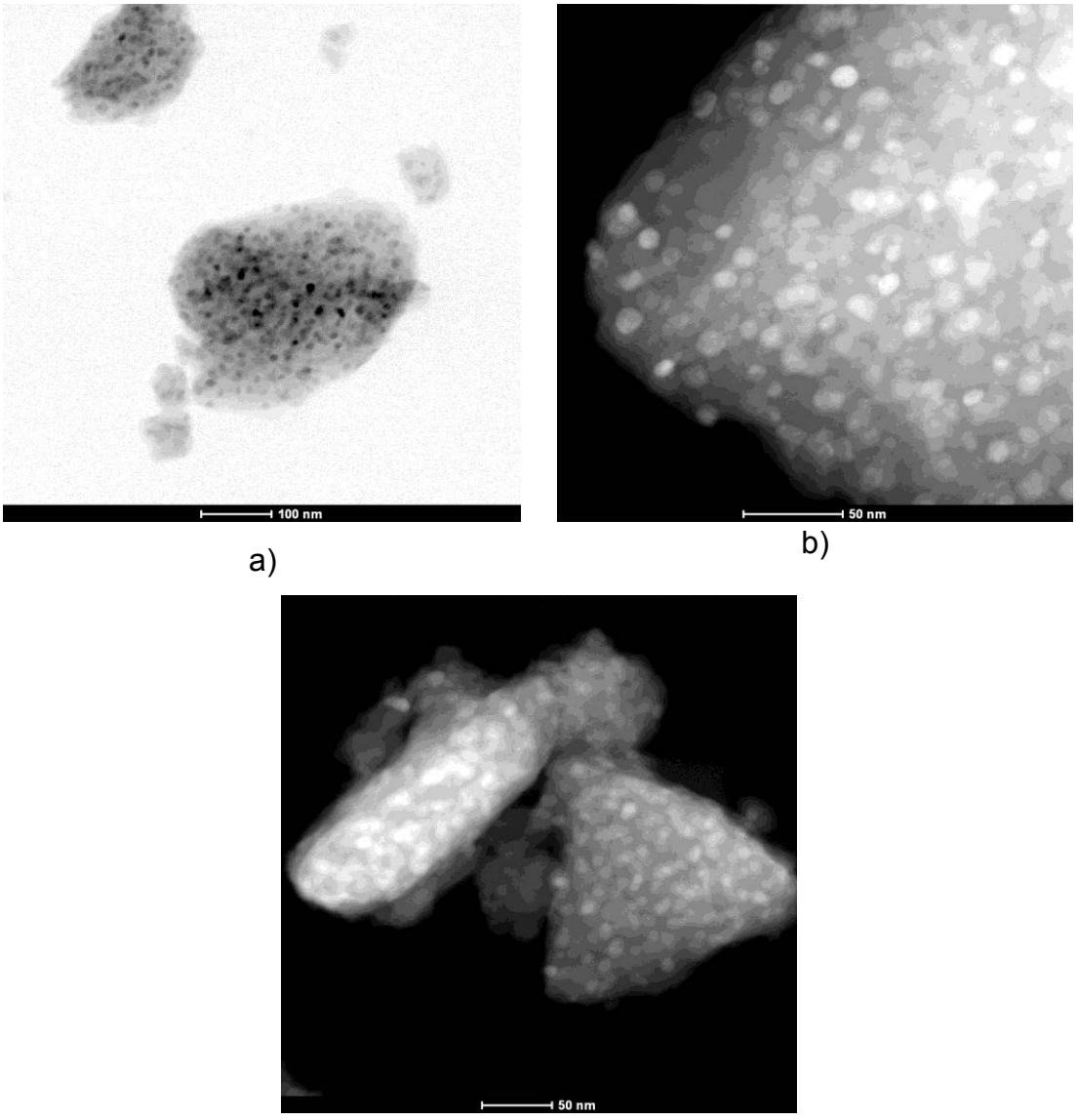

a) b)

c)

Figure 5.51 Transmission electron microscopy analysis of a sample from formulation 75-25/25Ti after nucleation treatment at 1073 K for 11520 min (8 days) and growth treatment for 3h at 1243 K a) bright field, b) dark-field and c) HAADF images.

The crystallization process is visually less intense than what is observed for a sample of formulation 75-25/ZT after nucleation treatment at 1078 K for 240 min and growth treatment for 6h at 1233 K (Fig. 5.45), despite the longer nucleation period applied. An 8-day nucleation process for formulation 75-25/25Ti lead to a less densely crystallized sample. That is an indication that

TiO_2 plays a more important role to nucleation compared to ZrO_2. Fig 5.52 presents the element distribution on the crystals, obtained by EDS detector during the TEM analysis. Antimony (Sb) was not analyzed since it has no role on crystallization.

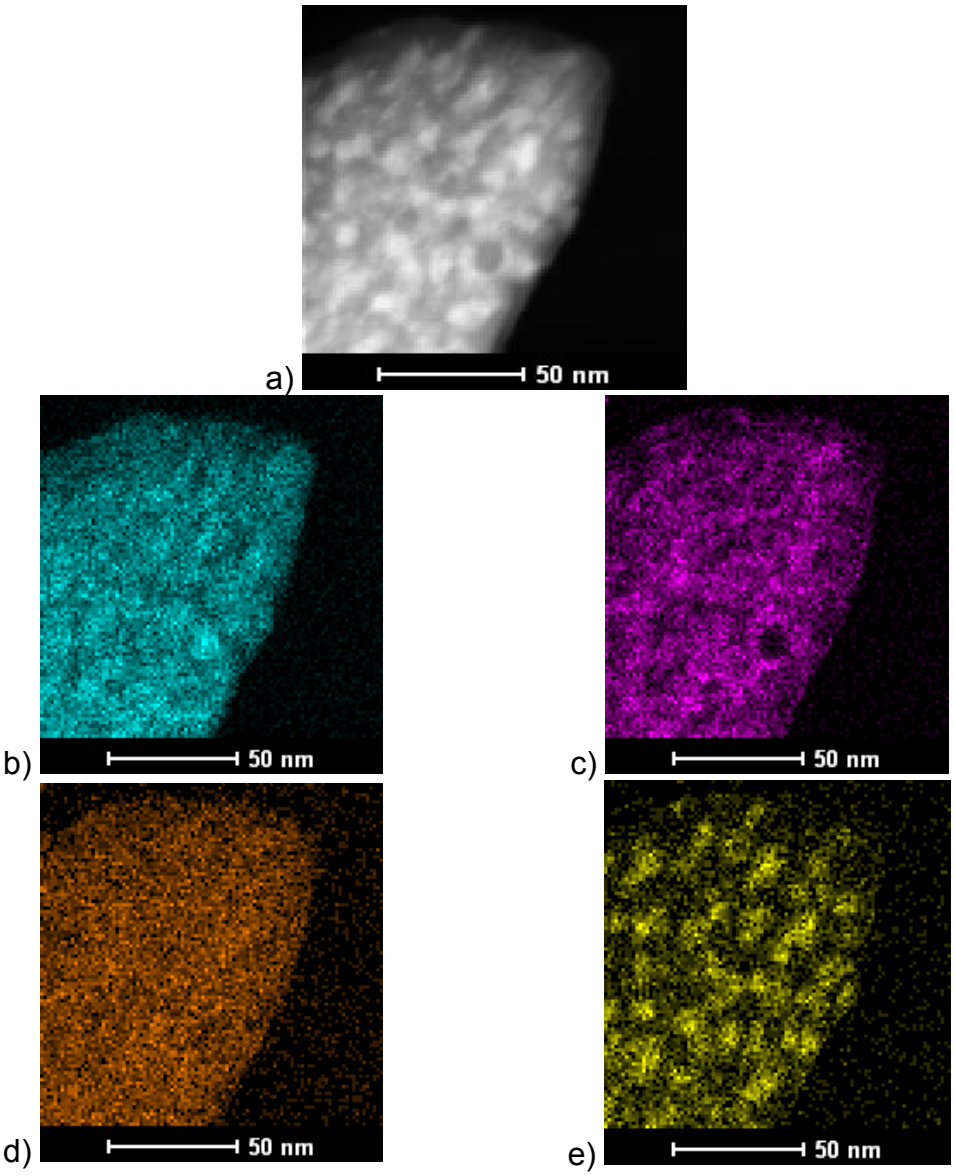

f) 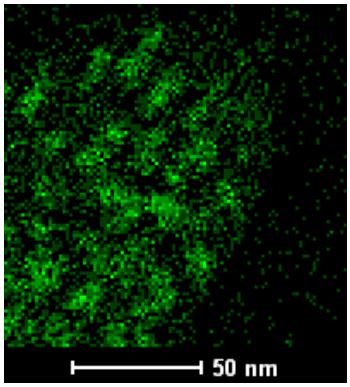

Figure 5.52 Element dispersion on the glass-ceramic particle from formulation 75-25/25Ti after nucleation treatment at 1073 K for 11520 min (8 days) and growth treatment for 3h at 1243 K. EDS images. a) original image used for EDS analysis and the elements present: b) Si; c) Al; d) Mg; e) Zr and f) Ti.

The nucleating agents are the most concentrated elements, the same way it happened for the analyzed sample of formulation 75-25/ZT. Mg is well spread on the residual glass and crystalline parts of the analyzed particles. Al and Si are apparently complementary.

The same way it was performed for formulation 75-25/ZT, a 6-hour growth step was performed here to observe if there would be an increase on hardness. It was observed that the glass, although it was visually homogeneous, after the double-stage heat treatment with 6h-growth at 1243 K, it presented non-homogeneous regions, as seen in Fig. 5.53. Two samples were crystallized and the measured properties are presented in table 5.13. Regions A and B on Fig. 5.54 b) indicate a transparent and opaque region, respectively. The opaque region must be a segregation of ZrO_2, due to its low dissolution on silicates [43].

a) 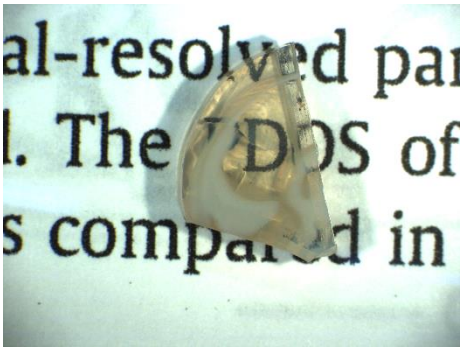

b) 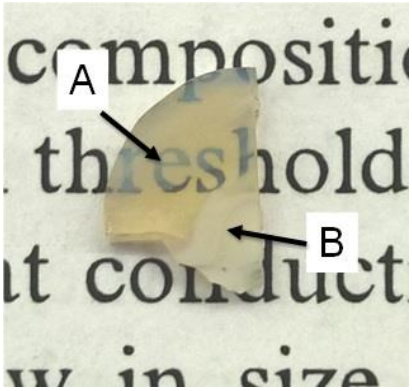

Figure 5.53 Glass-ceramic sample from 75-25/25Ti nucleated at a) 1073 K for 2880 min (2 days) and b) 1073 K for 4320 min (3 days). Both with growth treatment at 1243 K for 6h.

Table 5.13 Mechanical properties of formulation 75-25/25Ti, nucleated at different times at 1078 K and with growth treatment at 1233 K for 6h.

NUCLEATION TREATMENT (MIN)	HARDNESS (GPa)	IFT INCREASE (%)
GLASS SAMPLE	7.68 ± 0.06	-
2880	8.55 ± 0.06	35 ± 3
4320	8.7 ± 0.1	7 ± 3

Only two samples were prepared because no increase on hardness to values higher than 8.7 GPa was achieved, obtained after 8 days of nucleation at 1073 K and 3h of growth at 1243 K. Transmission electron microscopy analyses of regions A and B from the sample nucleated at 1073K for 4320 min and with growth treatment at 1243 K for 6h were conducted. The samples were ground prior to the analysis.

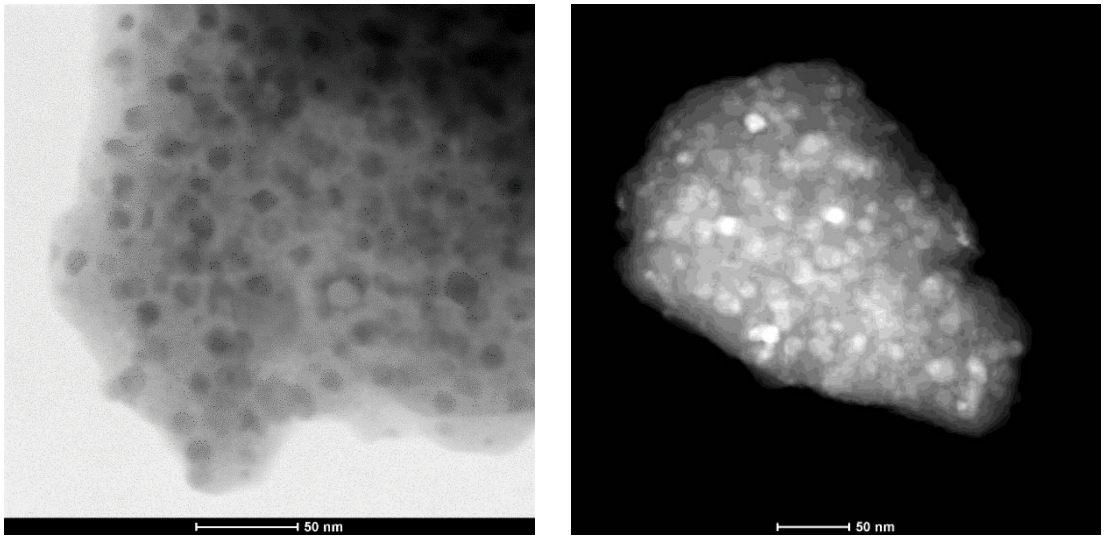

a) b)

Figure 5.54 Transmission electron microscopy analysis of the transparent region (region A on fig. 5.53) of a sample from formulation 75-25/25Ti after nucleation treatment at 1073 K for 4320 min and growth treatment for 6h at 1243 K a) bright field and b) dark-field images.

As it can be observed from TEM images, the sample is densely crystallized and it is possible to see crystals having an average size of 20 nm and even smaller ones. The increase on the growth time did not result on GCs with significantly higher hardness. Fig. 5.55 presents the element distribution on this sample.

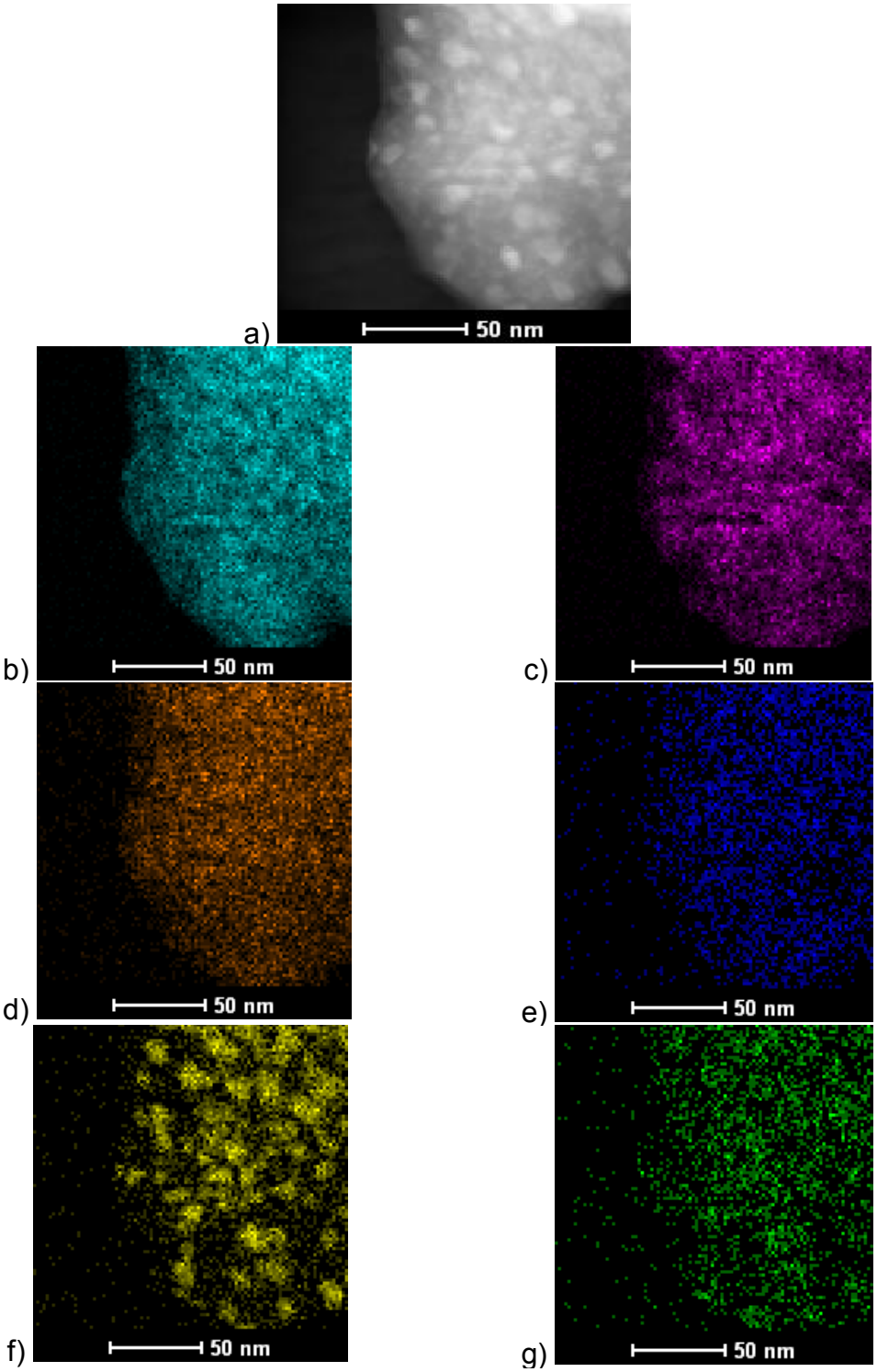

Figure 5.55 Element dispersion on the transparent region (region A on fig. 5.53) of the glass-ceramic sample from formulation 75-25/25Ti after nucleation treatment at 1073 K for 4320 min and growth treatment for 6h at 1243 K. EDS images. a) original image used for EDS analysis and the elements present: b) Si; c) Al; d) Mg; e) Sb; f) Zr and g) Ti.

Almost all the elements on the GC sample present the same distribution as for the GC sample after a 3h-growth. The only difference is the Zr distribution. After a 6-hour growth there is no concentration of this element, the opposite to what happened after a 3-hour growth. Fig 5.56 presents TEM images for the opaque region of a GC nucleated at 1073 K for 4320 min and with growth treatment at 1243 K for 6h (region B on fig. 5.53 b)).

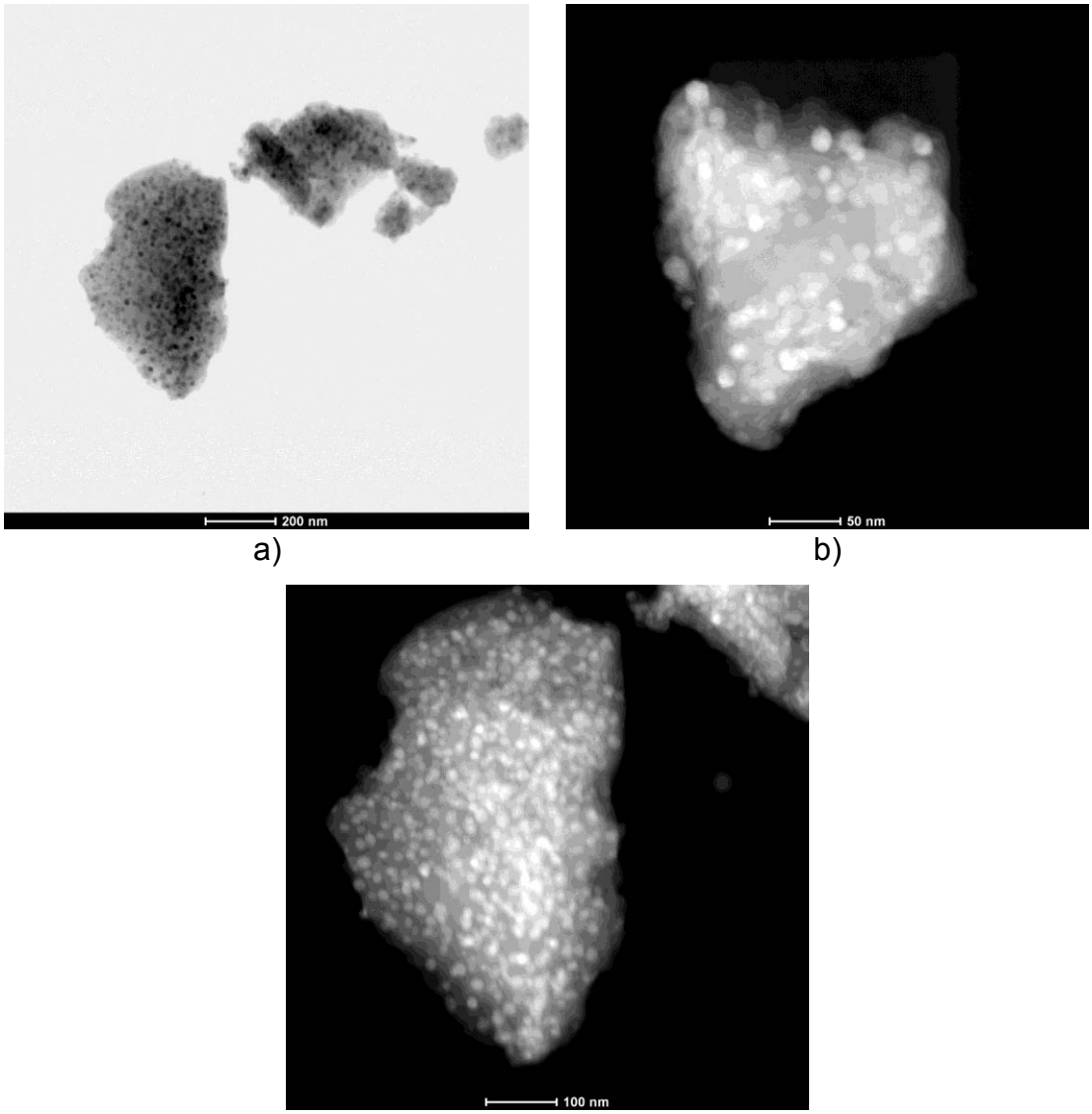

a) b)

c)

Figure 5.56 Transmission electron microscopy analysis of the opaque region (region B on fig. 5.53) a sample from formulation 75-25/25Ti after nucleation treatment at 1073 K for 4320 min and growth treatment for 6h at 1243 K a) bright field, b) dark-field and c) HAADF images.

Comparing TEM images from regions A and B of the GC sample presented on fig. 5.53 b), it seems that the opaque region is less densely crystallized than the transparent one and that the crystals have the same mean size (around 20 nm). Because of opacity, micron-size crystals may also be present on region B. They are not observed on TEM analysis by virtue of the high magnification applied. In an attempt to observe such crystals, the GC sample nucleated at 1073 K for 2880 min (2 days) and with growth treatment at 1243 K for 6h, Fig. 5.53 a), after a 5s-chemical etching with HF 5.3vol% was observed in an optical microscope. No crystals were observed, though. Fig. 5.57 presents the element distribution in region B.

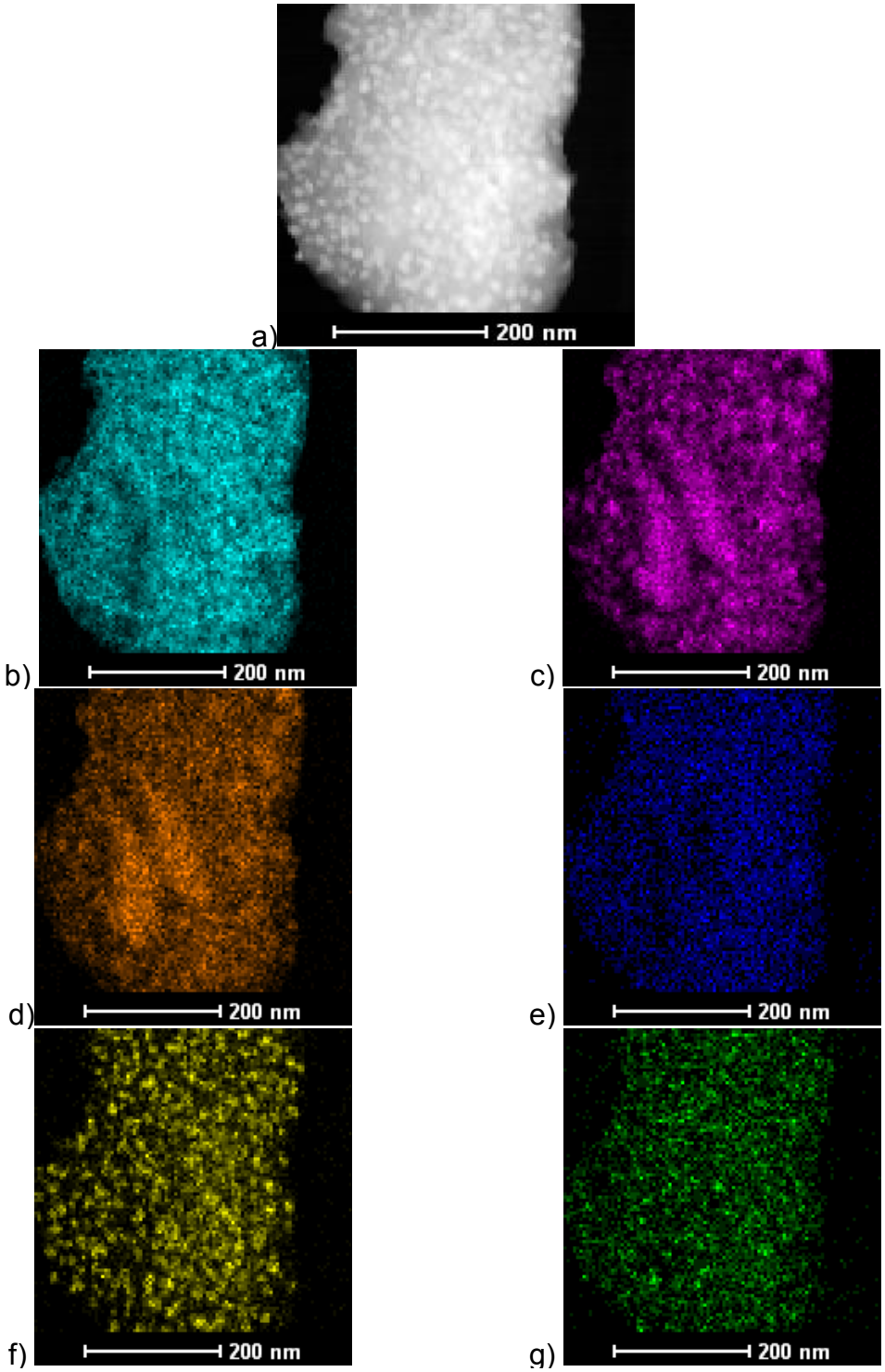

Figure 5.57 Element dispersion on the opaque region (region B on fig. 5.53) of the glass-ceramic sample from formulation 75-25/25Ti after nucleation treatment at 1073 K for 4320 min and growth treatment for 6h at 1243 K. EDS images. a) original image used for EDS analysis and the elements present: b) Si; c) Al; d) Mg; e) Sb; f) Zr and g) Ti.

Two remarkable facts must be pointed out after analyzing the images. The first one is that it is possible to observe a concentration of Al and Mg on the same site, indicating the presence of a crystalline phase with those two elements. The second one is the Ti distribution. In region B, Ti is more disperse and present in smaller crystals. Fig. 5.58 presents the XRD analysis of a sample nucleated at 1073 K for 2 days and with growth treatment at 1243 K for 6h.

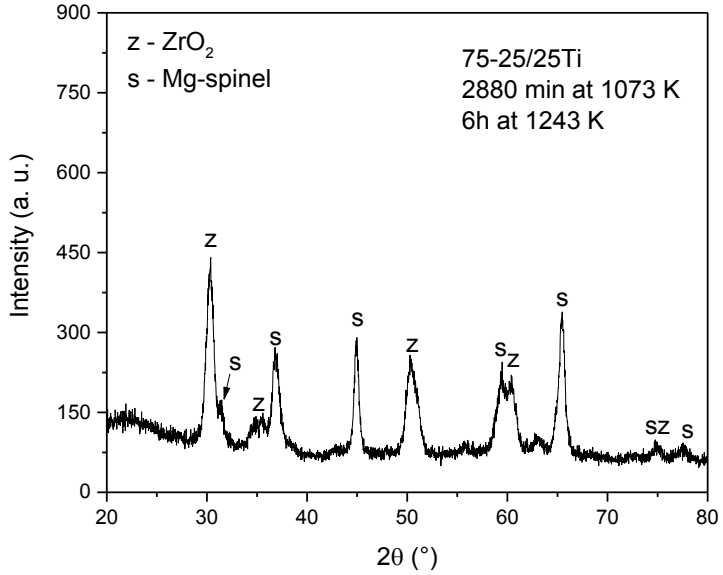

Figure 5.58 XRD pattern of glass-ceramic sample nucleated for 2880 min at 1073 K and with growth treatment for 6h at 1243 K.

The possible crystal phases present are also ZrO_2 and Mg-spinel, the same as for a sample with growth treatment of 3h at 1243 K. As it can be observed when one compares the XRD patterns, the intensity of the peaks on the sample crystallized with a growth step for 3h are more intense than for the sample with a 6-h growth step. The higher crystallinity can be the explanation for a higher hardness, even with the same possible crystal phases.

5.3 Part C

Attempting to remove TiO_2 as nucleating agent, and thus, the color of the glasses and glass-ceramics, a composition similar to the ones studied was proposed (presented on Table 5.14), but having no ZrO_2 and TiO_2 as nucleating agents, only metallic Ag, added as $AgNO_3$. This composition consisted of 80 mol% of the stoichiometry of cordierite ($2MgO.2Al_2O_3.5SiO_2$) and 20 mol% of other constituents. Four glasses were prepared and the amounts of $AgNO_3$ were added so as to have 200 ppm, 500 ppm, 1000 and 10,000 ppm of metallic silver in the glasses. After melting, all glasses are completely transparent and colorless. Fig. 5.59 presents the DSC analysis of the 4 glasses.

Table 5.14 Glass composition having excess of metallic Ag as nucleating agent.

Component	**mol%**
Al_2O_3	19.55
SiO_2	59.42
MgO	18.72
Sb_2O_3	1.05
B_2O_3	1.26

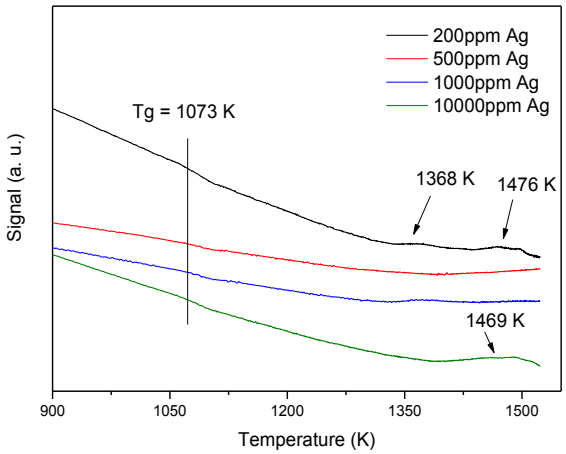

Figure 5.59 DSC analysis from compositions having different amounts of Ag. Bulk samples.

Glass transition of the compositions is approximately 1073 K, although is difficult to infer for sure due to the discrete inflexion of the curves. The glasses with 500 ppm and 1000 ppm of Ag presented no sign of crystallization. The other two presented discrete crystallization peaks, indicating a low propensity to crystallization. For this reason, only the glass with the highest amount of Ag was chosen for further investigation. This glass was dubbed 1Ag. Aiming at finding the temperature at which nucleation was maximum, a series of samples were treated for 3h at different temperatures: 1043 K (below Tg), 1073 K (Tg), 1093 K, 1103 K, 1113 K, 1133 K (above Tg). Fig 5.60 presents the DSC analysis of the nucleated samples and the graph of 1/Tmax versus the nucleation temperature.

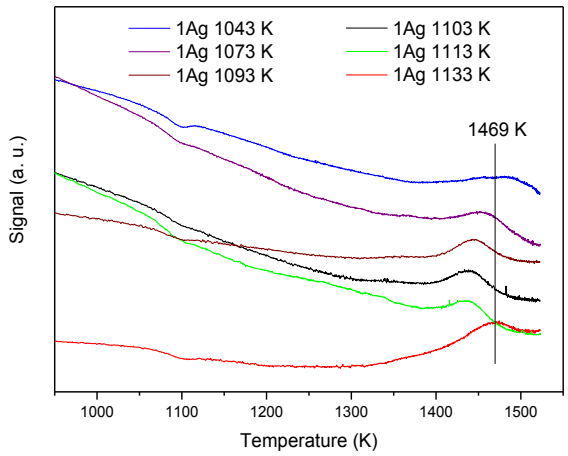

a)

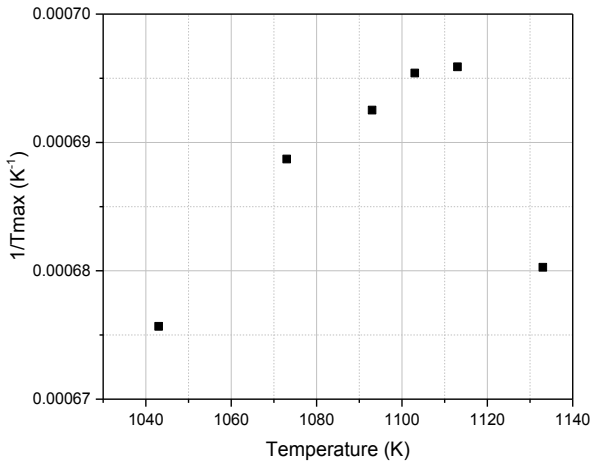

b)

Figure 5.60 a) DSC analysis of samples from formulation 1Ag nucleated for 3h at different temperatures. The straight line indicates the crystallization peak of glass without heat-treatment, for the sake of comparison. b) 1/Tmax of the crystallization peak *versus* nucleation temperature for the 3h heat-treated samples of 1Ag glass composition.

The maximum on the curve 1/Tmax *versus* nucleation temperature is observed at 1113 K. Two samples were nucleated at this temperature for 180 min and 360 min. Growth treatment was applied at 1434 K, the temperature of the crystallization peak after nucleation. It was observed, after crystallization, that the samples lost their original form, because of the high temperature of

growth. This fact, coupled with the discrete crystallization observed after the DSC analysis, lead to the abandoning of this path.

5.4 UV-Vis Transmittance

After analyzing of the effect of crystallization on the hardness of the samples from different compositions, double-stage heat-treatments that lead to the highest increase on Hv for each studied formulation was chosen to measure the light transmittance on the range from 380 nm to 780 nm. The samples had a diameter of 12 mm and the light passed through a slit of 8.16 mm. The heat-treatment applied for crystallization of a sample from formulation 75-25 had nucleation at 1006 K for 2 days and growth at 1173 K for 3h. This sample presented thickness of 1.58 mm. For formulation 75-25/ZT, nucleation was applied at 1078 K for 240 min and growth treatment at 1233 K for 6h. This sample had thickness of 1.91 mm. Finally, for formulation 75-25/25Ti nucleation was applied at 1073 K for 8 days and growth treatment at 1273 K for 3h. This sample was 1.50-mm thick. Fig. 5.61 present the transmittance of these samples before (glass) and after crystallization (glass-ceramic).

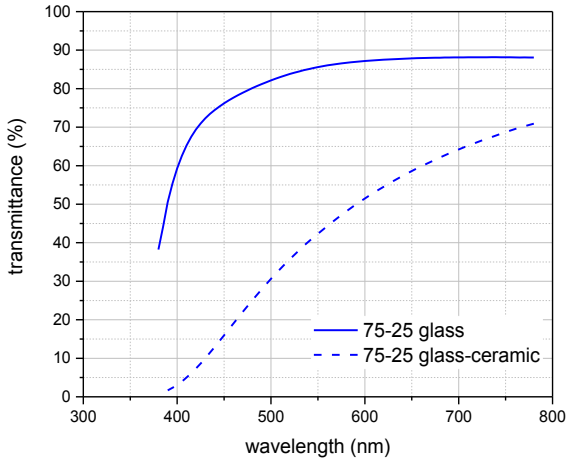

a)

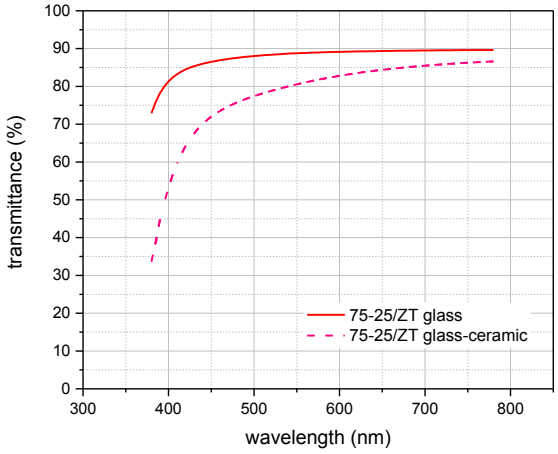

b)

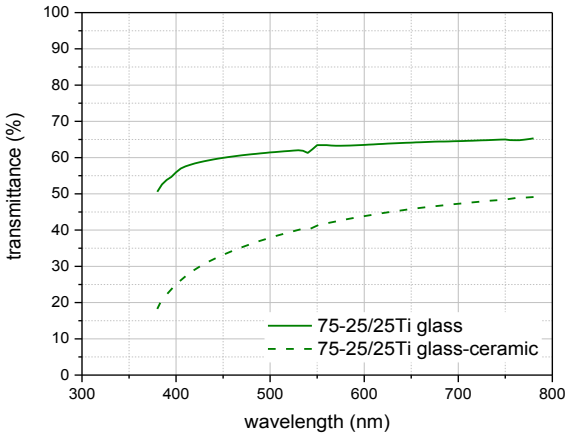

c)

Figure 5.61 a) Transmittance analysis of a glass and glass-ceramic sample from composition 75-25. Sample thickness was 1.58 mm. b) Transmittance analysis of a glass and glass-ceramic sample from composition 75-25/ZT. Sample thickness was 1.91 mm. c) Transmittance analysis of a glass and glass-ceramic sample from composition 75-25/25Ti. Sample thickness was 1.50 mm.

As it can be seen on Fig. 5.61 the samples had different behaviors before and after crystallization, despite the difference in thickness between samples. Among the glass samples, formulation 75-25 presented transmittance values close to formulation 75-25/ZT. For that formulation, transmittance values were higher than 80% for most of the analyzed wavelengths, but with an important drop at low wavelengths.

Inversely to what would be expected, the formulation with the lowest amount of TiO_2 was the one with the lowest transmittance values, close to 60%. This must be due to the presence of cords in the glass. This formulation has the highest amount of ZrO_2, and thus, the highest viscosity. It is known that zirconia has low solubility on silicates [43], making it difficult to have a good mix of the constituents. Cords on this glass are caused by local chemical differences and lead to a difference of the refractive index of the glass. The analyzed sample had a small crack on its bulk and must be the responsible for the small step observed on wavelengths close to 550 nm. This step is less pronounced on the glass-ceramic.

Formulation 75-25 presented the highest drop in transmittance after crystallization, being the drop at low wavelengths higher than at high wavelengths. Although the sample of formulation 75-25/ZT was the thickest, it was the one that presented the highest transmittance values, close to 90%, and the formulation that presented the lowest drop after crystallization.

6 SUMMARY AND CONCLUSIONS

In Part A of this thesis, the elastic moduli and Poisson's ratio of the glass of formulation 75-25 were studied as a function of temperature and time in three different stages: during heating from room temperature to crystallization temperature (1173 K) and during the nucleation (1006 K) and crystallization (1173 K) plateaus. During the first analyzed stage, the elastic moduli decreased in response to increasing temperature. The values of Poisson's ratio during this stage indicated a highly cross-linked structure that softened rapidly as temperatures increased, as indicated by an α value typical of a fragile glass. In the second stage, the evolution of E and G was more pronounced during the first 10h. The analysis of the third stage indicated that crystallization evolved faster during the first 2 hours at 1173 K. After the applied heat treatment, five crystalline phases were identified by high temperature XRD: spinel ($MgO.Al_2O_3$), rutile (TiO_2), karooite ($MgO.2TiO_2$), sillimanite ($Al_2O_3.SiO_2$) and sapphirine ($4MgO.5Al_2O_3.2SiO_2$). Samples of composition 75-25 were prepared, applying the same nucleation treatment but longer growth treatment, and hardness and K_{IC} were analyzed. The hardness of GC samples changed in response to the duration of the crystal growth treatment and applied load, remaining approximately between 8.25 and 9.75 GPa. The fracture toughness of the different GC samples remained the same within the experimental error, and increased by about 55% in comparison to the parent glass, reaching 1.2 $MPa.m^{1/2}$. Elemental distribution analysis (EDS) revealed Ti concentration gradients throughout the analyzed areas of the glass-ceramic samples, with some regions containing high concentrations and others low concentrations, possibly indicating that a certain concentration of titanium is required to ensure its performance as a nucleating agent.

In Part B of the thesis, the roles of titania and zirconia in the crystallization of the glass were analyzed by varying the ratio between these two nucleating agents. Formulation ZT1B4 yielded glass-ceramics with hardness values of about 8 GPa. Formulation 75-25/ZT presented slightly higher hardness values of about 8.2 GPa in the double-stage heat treatment with growth treatment of 3h. After 6 hours of growth heat-

treatment, the hardness increased to up to 9 GPa and Ti and Zr concentrations were much higher than in the previous treatment. This formulation originated two others, called 75-25/25Ti and 75-25/0Ti, the former presenting hardness values higher than 8.5 GPa. The EDS analysis indicated that Ti and Zr were densely concentrated after 3h of growth treatment. Composition 75-25/0Ti was discarded after melting due to poor dissolution of ZrO_2. Although none of the new glass formulations (ZT1B4, 75-25/ZT and 75-25/25Ti) matched the hardness values of the original formula (approximately 10 GPa for the transparent GCs), all the glasses and glass-ceramics presented less intense coloration.

In Part C of this thesis, a second attempt was made to develop a glass without TiO_2 by testing a formulation containing only metallic silver as a nucleating agent. Four glass compositions containing different amounts of $AgNO_3$ were prepared. These glasses did not yield homogeneous GCs and the glass-ceramic samples did not maintain their shape due to the high temperatures of the heat treatments, so these formulations were discarded.

Transmittance measured in the same sample, before and after crystallization, indicated that formulation 75-25 presented the highest drop in transmittance upon crystallization. The resulting GC (1.58 mm sample) was the least transparent of all the formulations. Formulation 75-25/ZT yielded the most transparent glass and GC, with a transparency higher than 85% for the glass and higher than 73% for the GC in a 1.91 mm sample. This formulation also presented the closest values of transparency between the glass and GC. Formulation 75-25/25Ti contained the smallest amount of TiO_2 and the highest zirconia content and produced the least transparent glass and a glass-ceramic (1.50 mm sample), with 40-50% transmittance in the visible range.

Two main conclusions can be drawn. First, from a technological standpoint, the most suitable formulation for use as a colorless device for ballistic protection is formulation 75-25/ZT. This glass showed the highest transparency and the lowest loss of transparency after crystallization, and its crystallization yielded GCs with hardness values of up to 85% of those of the transparent CGs from compositions L2R4 and 75-25.

Second, from the scientific standpoint, the system under study was unable to yield a colorless transparent glass-ceramic. The role of TiO_2 is fundamental in the bulk crystallization of glass-ceramics of this MAS system. Its substitution with ZrO_2 is possible to a certain extent. A minimum amount of 0.5 mol% of TiO_2 (formulation 75-25/25Ti) was necessary to trigger internal nucleation in the glass. Even so, inhomogeneity was observed due to the large amount (6.9 mol%) of ZrO_2 in this formulation.

7 FUTURE WORK

The *in situ* evolution of the mechanical properties and formation of the crystalline phase in formulation 75-25/ZT should be investigated to determine the sequence of crystalline phase formation. Such an investigation would reveal if a given heat treatment applied to obtain a transparent GC is the one that leads to the highest increase in mechanical properties, or if a microstructural evolution is still possible to optimize the mechanical properties.

The results presented here lead us to conclude that, based on hardness values, formulation 75-25/ZT is the most suitable one for use in ballistic protection devices. However, further investigations, and especially ballistic tests, are necessary to ensure that this material can provide effective protection against different levels of ballistic impact, since ballistic resistance involves many different factors. GC samples of this composition should be prepared and tested as specified, for instance, by the Brazilian standard ABNT NBR 15000, which classifies materials used for ballistic protection and provides guidelines for testing them. GC samples from formulation 75-25 should also be tested under the same conditions to determine whether the performance of formulation 75-25/ZT is similar or possibly even superior.

8 REFERENCES

[1] Gálvez, V. S.; Paradela, L. S.; Analysis of failure of add-on armour for vehicle protection against ballistic impact. Engineering Failure Analysis, 2009. 16(6): p. 9.

[2] Medvedovski, E.; Lightweight ceramic composite armour system. Advances in Applied Ceramics, 2006. 15(5): p. 5.

[3] da Silva, M. V.; StainerI, D.; Al-QureshiII, H. A.; Hotza, D.; Blindagens cerâmicas para aplicações balísticas: uma revisão. Cerâmica, 2014. 60(355): p. 9.

[4] Altug, G. S.; Özistek, T. D.; Dilibal, S.; Özbek, S.; Transparent Armour Systems and General Applications. MSI Defense Review, 2015. May 2015: p. 8.

[5] Salem, J. A.; Transparent Armor Ceramics as Spacecraft Windows. Journal of the American Ceramic Society, 2012. 96(1): p. 9.

[6] Hydras, L.; Transparent Impact Resistant System, U. S. P. T. Office, Editor. 2014, INTERNATIONAL CITY TECHNOLOGIES LLC.

[7] Budd, M.I.; Darrant, J.G.; Glass-ceramic armour, I.P. Office, Editor. 1995, GEC Alsthom: UK. p. 16.

[8] Navarro, J. M. F.; El vidrio. 3rd ed. 2003, Madrid: Consejo Superior de Investigaciones Científicas. 720.

[9] Ballistics definition. [cited 2016 June, 1st].

[10] Abrablin. [cited 2012 August 15th].

[11] Abrablin. Table Balística Norma ABNT. 2012.

[12] National Institute of Justice, Ballistic Resistant Protective Materials. 1985, National Institute of Justice. p. 9.

[13] BCA Textil. Protection levels for automotive shielding 2015.

[14] Woodward, R. L.; Gooch Jr., W. A.; O'Donnell, R. G.; Perciballi, W. J.; Baxter, B. J.; Pattie, S. D.; A study of fragmentation in the ballistic impact

of ceramics. International Journal of Impact Engineering, 1994. 15(5): p. 14.

[15] Medvedovski, E.; Alumina ceramics for ballistic protection, Part 1. American Ceramic Society Bulletin 2002. 81(3): p. 6.

[16] Naik, N. K.; Shrirao, P.; Reddy, B. C. K.; Ballistic impact behaviour of woven fabric composites: Parametric studies. Materials Science and Engineering: A, 2005. 412(1-2): p. 13.

[17] Gonçalves, D. P.; Análise e investigação de impactos em blindagem composta cerâmica/metal., in Engenharia Aeronáutica e Mecânica. 2000, Instituto Tecnológico de Aeronáutica. p. 107.

[18] Naebe, M.; Sandlin, J.; Crouch, I.; Fox, B.; Novel polymer-ceramic composites for protection against ballistic fragments. Polymer Composites, 2013. 34(2): p. 7.

[19] LaSalvia, J. C.; Campbell, J.; Swab, J. J.; McCauley, J. W.; Beyond hardness: Ceramics and ceramic-based composites for protection. The Journal of The Minerals, 2010. 62(1): p. 8.

[20] Rudoi, B. L.; Ballistic resistant glass-ceramic and method of preparation., U. S. P. T. Office, Editor. 1984: USA. p. 8.

[21] Stookey, S. D.; Ceramic body and method of making it, U. S. P. T. Office, Editor. 1961, Corning Glass Works: USA. p. 6.

[22] Beall, G. H.; Glass-ceramic bodies and method of making them, U. S. P. T. Office, Editor. 1966, Corning Glass Works: USA. p. 7.

[23] Takagi, K.; Tashiro, M.; Method of preventing scum formation in glass melts, and glass-ceramic products, U. S. P. T. Office, Editor. 1966, Nippon Electric Glass Co: USA. p. 3.

[24] Bolton, N.; Smith, W. N.; Fire resistant transparent laminates, U. S. P. T. Office, Editor. 1996, Artistic Glass Products Company: USA.

[25] Darrant, J. G.; Thompson, C. A.; Processing of transparent glass-ceramic W.I.P. Organization, Editor. 2003, Alstom. p. 28.

[26] Weinhold, C.; Lightweight transparent armor window, U. S. P. T. Office, Editor. 2013, Schott Corporation: USA. p. 22.

[27] Gallo, L.S.; Vitrocerâmicas do sistema MgO – Al_2O_3 – SiO_2 para uso em proteção balística, in Departamento de Enganharia de MAteriais. 2012, Universidade Federal de São Carlos: Brazil.

[28] Zachau, T.; Corvers, S.; Reactive Armor, U. S. P. T. Office, Editor. 2013: USA. p. 11.

[29] da Cunha, T. B.; Wu, J. P.; Peitl, O.; Fokin, V. M.; Zanotto, E. D.; Iannucci, L.; Boccaccini, A. R.; Mechanical Properties and Impact Resistance of a New Transparent Glass-Ceramic. Advanced Engineering Materials, 2007. 9(3): p. 6.

[30] Clayton, J. D.; Penetration resistance of armor ceramics: Dimensional analysis and property correlations. International Journal of Impact Engineering, 2015. 85: p. 8.

[31] Neshpor, V. C.; Zaitsev, G. P.; Dovgal, E. J.; Maystrenko, A. L.; Dasevskaya, O. B.; Armour ceramics ballistic efficiency evaluation. in World Ceramics Congress. 1995. Florence, Italy.

[32] Liebald. R.; Beier, W.; Alkemper, J.; Schiffner, U.; Armor material and method for producing it, U. S. P. T. Office, Editor. 2011, SCHOTT AG: USA.

[33] Carberry, J.; Boyett, J.; Cline, C.; Mirata, M.; Leighton, K. T.; Serafin, W.; Aleshire, E.; Glass-Ceramic with laminates, U. S. P. T. Office, Editor. 2009, PITTS AND BRITTIAN P C: USA.

[34] Jones, R. W., Armor materials U.P.a.T. Office, Editor. 1991, Ceramic Developments (Midlands) Limited: USA. p. 6.

[35] Raichel, A.; Nachumi, A.; Raichel, S.; Protection from kinetic threats using glass-ceramic material, U. S. P. T. Office, Editor. 2005, GlassCerax Ltd.: USA. p. 19.

[36] Haney, E. J.; Subhash, G.; Damage Mechanisms Perspective on Superior Ballistic Performance of Spinel over Sapphire. Experimental Mechanics, 2012. 53(1): p. 16.

[37] Krell, A.; Strassburger, E.; Order of influences on the ballistic resistance of armor ceramics and single crystals. Materials Science and Engineering: A, 2014. 597: p. 9.

[38] Krell, A.; Strassburger, E.; Hutzler, T.; Klimke, J.; Single and Polycrystalline Transparent Ceramic Armor with Different Crystal Structure. Journal of the American Ceramic Society, 2013. 96(9): p. 4.

[39] Chen, G.-H.; Liu, X.-Y.; Influence of AlN addition on thermal and mechanical properties of cordierite-based glass/ceramic composites. Journal of Materials Processing Technology, 2007. 190(1-3): p. 4.

[40] Chen, G.-H.; Liu, X.-Y.; Sintering, crystallization and properties of MgO–Al_2O_3–SiO_2 system glass-ceramics containing ZnO. Journal of Alloys and Compounds, 2007. 431(1-2): p. 4.

[41] Marghussian, V. K.; Balazadegan, O.; Eftekhari-yekta, B.; Crystallization behaviour, microstructure and mechanical properties of cordierite–mullite glass ceramics. Journal of Alloys and Compounds, 2009. 484: p. 902–906.

[42] Höland, W.; Beall, G. H.; Glass Ceramic Technology. 2nd Edition ed. 2012: Wiley.

[43] Goel, A.; Shaaban, E. R.; Melo F. C. L.; Ribeiro, M. J.; Ferreira J. M. F.; Non-isothermal crystallization kinetic studies on MgO– Al_2O_3–SiO_2–TiO_2 glass. Journal of Non-Crystalline Solids, 2007. 353: p. 2383–2391.

[44] MgO–Al_2O_3–SiO_2 phase equilibria diagram. Teaching Phase Equilibria December, 14th 2015 [cited 2014 March, 10th].

[45] Wang, S.-M.; Kuang, F.-H.; Yan, Q.-Z.; Ge, C.-C.; Qi, L.-H.; Crystallization and infrared radiation properties of iron ion doped cordierite glass-ceramics. Journal of Alloys and Compounds, 2011. 509(6): p. 5.

[46] Shao, H.; Liang, K.; Zhou, F.; Wang, G.; Hu, A.; Microstructure and mechanical properties of MgO– Al_2O_3–SiO_2–TiO_2 glass–ceramics. Materials Research Bulletin, 2005. 40(3): p. 7.

[47] Shao, H.; Liang, K.; Peng, F.; Crystallization kinetics of MgO– Al_2O_3–SiO_2 glass-ceramics. Ceramics International, 2004. 30(6): p. 4.

[48] Chavoutier, M.; Caurant, D.; Majérus, O.; Boulesteix, R.; Loiseau, P.; Jousseaume, C.; Brunet, E.; Lecomte, E.; Effect of TiO2 content on the crystallization and the color of (ZrO_2, TiO_2)-doped Li_2O–Al_2O_3–SiO_2 glasses. in 10th International Symposium on Crystallization in Glasses and Liquids 2012. Goslar, Germany: Journal of Non-Crystalline Solids.

[49] Fokin, V. M.; Zanotto, E. D.; Surface and volume nucleation and growth in TiO2–cordierite glasses. Journal of Non-Crystalline Solids, 1999. 246(1-2): p. 13.

[50] Anusavice, K. J.; Zhang, N. Z.; Moorhead, J. E.; Influence of colorants on crystallization and mechanical properties of lithia-based glass-ceramics. Dental Materials, 1994. 10(2): p. 6.

[51] Mishima, N.; Wakasugi, T.; Ota, R.; Bulk crystallisation in mixed alkali disilicate glasses doped with a nucleating agent. Physics and Chemistry of Glasses 2006. 47(3): p. 7.

[52] Mishima, N.; Wakasugi, T.; Ota, R.; Nucleation Behavior of Li_2O-Na_2O-SiO_2 Glass Doped with Platinum. Journal of the Ceramic Society of Japan 2004. 112(1036): p. 4.

[53] ASTM International, Standard Test Method for Vickers Indentation Hardness of Advanced Ceramics. 2008, ASTM International. p. 8.

[54] Callister Jr., W.D.; Materials Science and Engineering: An Introduction, 7th Edition. 2007: Wiley Publishers.

[55] Wachtman, J. B., Cannon, W. R.; Matthewson, M. J.; Mechanical Properties of Ceramics 2nd Edition ed. 2009: Wiley. 496.

[56] Green, D. J.; An Introduction to the Mechanical Properties of Ceramics. 1998: Cambridge University Press. 352.

[57] Nishida, T.; Shiono, T.; Nishikawa, T.; On the Fracture Toughness of Polycrystalline Alumina Measured by SEPB Method. Journal of the European Ceramic Society, 1989. 5(6): p. 5.

[58] Nose, T.; Fujii, T.; Evaluation of Fracture Toughness for Ceramic Materials by a Single-Edge-Precracked-Beam Method. Journal of the American Ceramic Society, 1988. 71(5): p. 6.

[59] Ponton, C. B.; Rawlings, R. D.; Vickers indentation fracture toughness test Part 1 Review of literature and formulation of standardised indentation toughness equations. Materials Science and Technology, 1989. 5(9): p. 8.

[60] Anstis, G. R.; Chantikul, P.; Lawn, B. R.; Marshall, D. B.; A Critical Evaluation of Indentation Techniques for Measuring Fracture Toughness: I, Direct Crack Measurements. Journal of the American Ceramic Society, 1981. 64(9): p. 6.

[61] Quinn, G. D.; Bradt, R. C.; On the Vickers Indentation Fracture Toughness Test. Journal of the American Ceramic Society, 2007. 90(3): p. 8.

[62] Feng, Y.; Zhang, T.; Yang, R.; A Work Approach to Determine Vickers Indentation Fracture Toughness. Journal of the American Ceramic Society, 2011. 94(2): p. 4.

[63] Ray, K. K.; Dutta, A. K.; Comparative study on indentation fracture toughness evaluations of soda–lime–silica glass. British Ceramic Transactions, 1999. 98(4): p. 7.

[64] Kruzic, J. J.; Ritchie, R. O.; Determining the Toughness of Ceramics from Vickers Indentations Using the Crack-Opening Displacements: An Experimental Study. Journal of the American Ceramic Society, 2003. 86(8): p. 4.

[65] Niihara, K.; A fracture mechanics analysis of indentation-induced Palmqvist crack in ceramics. Journal of Materials Science Letters, 1983. 2(5): p. 3.

[66] Cook, R. F.; Pharr, G. M.; Direct Observation and Analysis of Indentation Cracking in Glasses and Ceramics. Journal of the American Ceramic Society, 1990. 73(4): p. 11.

[67] Serbena, F. C.; Mathias I.; Foerster, C. E.; Zanotto, E. D.; Crystallization toughening of a model glass-ceramic. Acta Materialia, 2015. 86: p. 13.

[68] Ponton, C. B.; Rawlings, R. D.; Vickers indentation fracture toughness test Part 2 Application and critical evaluation of standardised indentation toughness equations. Materials Science and Technology, 1989. 5(10): p. 16.

[69] Boch, P.; Nièpce, J.-C.; Ceramic Materials: Processes, Properties, and Applications, ed. P. Boch and J.-C. Nièpce. 2007: Wiley-ISTE.

[70] Rouxel, T.; Elastic Properties and Short-to Medium-Range Order in Glasses. Journal of the American Ceramic Society, 2007. 90(10): p. 20.

[71] IMCE - Integrated Material Control Engineering n.v., RFDA HT 1050 Software Manual. p. 63.

[72] ASTM International, Standard Test Method For Dynamic Young's Modulus, Shear Modulus, and Poisson's Ratio by Impulse Excitation of Vibration. 2009, ASTM International. p. 16.

[73] Spinel Mineral Data. Mineralogy Database 9/5/2012 May 4th]; Available from: http://webmineral.com/data/Spinel.shtml#.VTeNTyGqqko.

[74] Mullite Mineral Data. [cited 2015 December, 10th].

[75] Rutile Mineral Data. Mineralogy Database 9/5/2012 May, 5th]; Available from: http://webmineral.com/data/Rutile.shtml#.VJBCLyvF-So.

[76] Sapphirine Mineral Data. Mineralogy Database 9/5/2012 May 1st]; Available from: http://webmineral.com/data/Sapphirine.shtml#.VS0zZ_mUeSo.

[77] Guignard, M.; Cormier, L.; Montouillout, V.; Menguy, N.; Massiot, D.; Structural fluctuations and role of Ti as nucleating agent in an aluminosilicate glass. Journal of Non-Crystalline Solids, 2010. 356(25-27): p. 5.

[78] Wachtman, J. B.; Tefft, W. E.; Lam, D. G.; Apstein, C.S.; Exponential Temperature Dependence of Young's Modulus for Several Oxides. Physical Review, 1961. 122: p. 6.

[79] Rouxel, T.; Thermodynamics of viscous flow and elasticity of glass forming liquids in the glass transition range. The Journal of Chemical Physics, 2011. 135: p. 15.

[80] Angell, C. A.; Perspective on the glass transition. Journal of Physics and Chemistry of Solids, 1988. 49(8): p. 8.

[81] Huger, M.; Chotard, T.; Internal report. Université de Limoges: Limoges.

[82] Gueguen, Y.; Rouxel, T.; Gadaud, P.; Bernard, C.; Keryvin, V.; Sangleboeuf, J.-C.; High-temperature elasticity and viscosity of GexSe1−x glasses in the transition range. PHYSICAL REVIEW B, 2011. 84(6): p. 8.

[83] Askarpour, V.; Manghnani, M. H. ; Richet, P.; Elastic properties of diopside, anorthite, and grossular glasses and liquids: A Brillouin Scattering study up to 1400 K. Journal of Geophysical Research, 1993. 98(B10): p. 6.

[84] Angell, C. A.; Simulation of glasses and glass-forming liquids after two decades: some perspectives. Computational Materials Science, 1995. 4: p. 6.

[85] Weinberg, M. C.; Birnie III, D. P.; Shneidman, V. A; Crystallization kinetics and the JMAK equation Journal of Non-Crystalline Solids 1997. 219: p. 11.

[86] Zanotto, E. D.; Galhardi, A.; Experimental test of the general theory of transformation kinetics: Homogeneous nucleation in a $Na_2O{\cdot}2CaO{\cdot}3SiO_2$ glass. Journal of Non-Crystalline Solids, 1988. 104(1): p. 8.

[87] Quinn, G.D.; Green, P.; Xu, K.; Cracking and the Indentation Size Effect for Knoop Hardness of Glasses. Journal of the American Ceramic Society, 2003. 86(3): p. 8.

[88] Fokin, V. M.; Potapova, O. V.; Chinaglia, C. R.; Zanotto, E. D.; The effect of pre-existing crystals on the crystallization kinetics of a soda–lime-silica glass. The courtyard phenomenon. Journal of Non-Crystalline Solids, 1999. 258(1-3): p. 7.

VU :

Le Directeur de Thèse
(Nom et Prénom)

VU :

Le Responsable de l'École Doctorale

VU pour autorisation de soutenance

Rennes, le

Le Président de l'Université de Rennes 1

Davis ALIS

VU après soutenance pour autorisation de publication :

Le Président de Jury,
(Nom et Prénom)